

The detection of a hot molecular core in the extreme outer Galaxy

TAKASHI SHIMONISHI,^{1,2} NATSUO IZUMI,³ KENJI FURUYA,⁴ AND CHIKAKO YASUI⁵

¹*Center for Transdisciplinary Research, Niigata University, Ikarashi-nincho 8050, Nishi-ku, Niigata, 950-2181, Japan*

²*Environmental Science Program, Department of Science, Faculty of Science, Niigata University, Ikarashi-nincho 8050, Nishi-ku, Niigata, 950-2181, Japan*

³*Institute of Astronomy and Astrophysics, Academia Sinica, No. 1, Section 4, Roosevelt Road, Taipei 10617, Taiwan*

⁴*National Astronomical Observatory of Japan, Osawa 2-21-1, Mitaka, Tokyo 181-8588, Japan*

⁵*National Astronomical Observatory of Japan, California Office, 100 W. Walnut St., Suite 300, Pasadena, CA 91124, USA*

ABSTRACT

Interstellar chemistry in low metallicity environments is crucial to understand chemical processes in the past metal-poor universe. Recent studies of interstellar molecules in nearby low-metallicity galaxies have suggested that the metallicity has a significant effect on chemistry of star-forming cores. Here we report the first detection of a hot molecular core in the extreme outer Galaxy, which is an excellent laboratory to study star formation and interstellar medium in a Galactic low-metallicity environment. The target star-forming region, WB89-789, is located at the galactocentric distance of 19 kpc. Our ALMA observations in 241-246, 256-261, 337-341, and 349-353 GHz have detected a variety of carbon-, oxygen-, nitrogen-, sulfur-, and silicon-bearing species, including complex organic molecules (COMs) containing up to nine atoms, towards a warm (>100 K) and compact (< 0.03 pc) region associated with a protostar ($\sim 8 \times 10^3 L_\odot$). Deuterated species such as HDO, HDCO, D₂CO, and CH₂DOH are also detected. A comparison of fractional abundances of COMs relative to CH₃OH between the outer Galactic hot core and an inner Galactic counterpart shows a remarkable similarity. On the other hand, the molecular abundances in the present source do not resemble those of low-metallicity hot cores in the Large Magellanic Cloud. The results suggest that a great molecular complexity exists even in a primordial environment of the extreme outer Galaxy. The detection of another embedded protostar associated with high-velocity SiO outflows is also reported.

Keywords: astrochemistry – ISM: molecules – stars: protostars – ISM: jets and outflows – radio lines: ISM

1. INTRODUCTION

Understanding the star formation and interstellar medium (ISM) at low metallicity is crucial to unveil physical and chemical processes in the past Galactic environment or those in high-redshift galaxies, where the metallicity was significantly lower compared to the present-day solar neighborhood.

Hot molecular cores are one of the early stages of star formation and they play a key role in the formation of chemical complexity of the ISM. Physically, hot cores are defined as having small source size ($\lesssim 0.1$ pc), high density ($\gtrsim 10^6$ cm⁻³), and warm gas/dust temperature ($\gtrsim 100$ K) (e.g., van Dishoeck & Blake 1998; Kurtz et al. 2000). Chemistry of hot cores is characterized by sublimation of ice mantles,

which accumulated in the course of star formation. In cold molecular clouds and prestellar cores, gaseous molecules and atoms are frozen onto dust grains. With increasing dust temperatures by star formation activities, chemical reaction among heavy species become active on grain surfaces to form larger complex molecules (e.g., Garrod & Herbst 2006). In addition, sublimated molecules, such as CH₃OH and NH₃, are subject to further gas-phase reactions (e.g., Nomura & Millar 2004; Taquet et al. 2016). As a result, warm and dense gas around protostars become chemically rich, and embedded protostars are observed as one of the most powerful molecular line emitters, which is called a hot core. They are important targets for astrochemical studies of star-forming regions, because a variety of molecular species, including complex organic molecules (COMs), are often detected in hot cores (Herbst & van Dishoeck 2009, and references therein). Thus detailed studies on chemical properties of hot cores are important for understanding complex chemical processes triggered by star formation.

Corresponding author: Takashi Shimonishi
 shimonishi@env.sc.niigata-u.ac.jp

Recent ALMA (Atacama Large Millimeter/submillimeter Array) observations of hot molecular cores in a nearby low metallicity galaxy, the Large Magellanic Cloud (LMC), have suggested that the metallicity has a significant effect on their molecular compositions (Shimonishi et al. 2016b, 2020; Sewiło et al. 2018); cf., the metallicity of the LMC is $\sim 1/2\text{--}1/3$ of the solar neighborhood. A comparison of molecular abundances between LMC and Galactic hot cores suggests that organic molecules (e.g., CH₃OH, a classical hot core tracer) show a large abundance variation in low-metallicity hot cores (Shimonishi et al. 2020). There are organic-poor hot cores that are unique in the LMC (Shimonishi et al. 2016b), while there are relatively organic-rich hot cores, where the abundances of organic molecules roughly scale with the metallicity (Sewiło et al. 2018). Astrochemical simulations for low-metallicity hot cores suggest that dust temperature during the initial ice-forming stage would play a key role for making the chemical diversity of organic molecules (Acharyya & Herbst 2018; Shimonishi et al. 2020). On the other hand, sulfur-bearing molecules such as SO₂ and SO are commonly detected in known LMC hot cores and their molecular abundances roughly scale with the metallicity of the LMC. Although the reason is still under debate, the results suggest that SO₂ can be an alternative molecular species to trace hot core chemistry in metal-poor environments.

The above results suggest that molecular abundances in hot cores do not always simply scale with the elemental abundances of their parent environments. However, it is still unclear if the observed chemical characteristics of LMC hot cores are common in other low metallicity environments or they are uniquely seen only in the LMC. Currently, known low-metallicity hot core samples are limited to those in the LMC. It is thus vital to understand universal characteristics of interstellar chemistry by studying chemical compositions of star-forming cores in diverse metallicity environments.

Recent surveys (e.g., Anderson et al. 2015, 2018; Izumi et al. 2017; Wenger et al. 2021) have found a number of ($\sim 10\text{--}20$) star-forming region candidates in the extreme outer Galaxy, which is defined as having galactocentric distance (D_{GC}) larger than 18 kpc (Yasui et al. 2006; Kobayashi et al. 2008). The extreme outer Galaxy has a very different environment from those in the solar neighborhood, with lower metallicity (less than -0.5 dex, Fernández-Martín et al. 2017; Wenger et al. 2019), lower gas density (e.g., Nakanishi & Sofue 2016), and small or no perturbation from spiral arms. Such an environment is of great interest for studies of the star formation and ISM in the early phase of the Milky Way formation and those in dwarf galaxies (Ferguson et al. 1998; Kobayashi et al. 2008). The low metallicity environment is in common with the Magellanic Clouds, and thus the extreme outer Galaxy is an

ideal laboratory to test the universality of the low metallicity molecular chemistry observed in the LMC and SMC.

Among star-forming regions in the extreme outer Galaxy, WB89-789 (IRAS 06145+1455; $06^{\text{h}}17^{\text{m}}24^{\text{s}}.2$, $14^{\circ}54'42''$, J2000) has particularly young and active nature (Brand & Wouterloot 1994). It is located at the galactocentric distance of 19.0 kpc and the distance from Earth is 10.7 kpc (based on optical spectroscopy of a K3 III star, Brand & Wouterloot 2007). The metallicity of WB89-789 is estimated to be a factor of four lower than the solar value according to the Galactic oxygen abundance gradient reported in the literature (Fernández-Martín et al. 2017; Wenger et al. 2019; Bragança et al. 2019; Arellano-Córdova et al. 2020, 2021). The region is associated with dense clouds traced by CS and CO (Brand & Wouterloot 2007). The total mass of the cloud is estimated to be $6 \times 10^3 M_{\odot}$ for a ~ 10 pc diameter area (Brand & Wouterloot 1994). An H₂O maser is detected towards the region (Wouterloot et al. 1993), but no centimeter radio continuum is found (Brand & Wouterloot 2007). Several class I protostar candidates are identified by previous infrared observations (Brand & Wouterloot 2007).

We here report the first detection of a hot molecular core in the extreme outer Galaxy based on submillimeter observations towards WB89-789 with ALMA. Section 2 describes the details of the target source, observations, and data reduction. The observed molecular line spectra and images, as well as analyses of physical and chemical properties of the source, are presented in Section 3. Discussion about the properties of the hot core and comparisons of molecular abundances with known Galactic and LMC hot cores are given in Section 4. This section also presents the detection of another embedded protostar with high-velocity outflows in the WB89-789 region. The conclusions are given in Section 5.

2. TARGET, OBSERVATIONS, AND DATA REDUCTION

2.1. Target

The target star-forming region is WB89-789 (Brand & Wouterloot 1994). The region contains three Class I protostar candidates identified by near-infrared observations (Brand & Wouterloot 2007), and one of them is a main target of the present ALMA observations. The region observed with ALMA is indicated on a near-infrared two-color image shown in Figure 1. The observed position is notably reddened compared with other parts of WB89-789.

2.2. Observations

Observations were conducted with ALMA in 2018 and 2019 as a part of the Cycle 5 (2017.1.01002.S) and Cycle 6 (2018.1.00627.S) programs (PI: T. Shimonishi). A summary of the present observations is shown in Table 1. The pointing

Table 1. Observation summary

	Observation	On-source	Mean	Number	Baseline			Channel	
					Date	Time	PWV ^a	of	Min
						(min)	(mm)	Antennas	(m)
Band 6	2018 Dec 6 – (250 GHz)	115.5	0.5–1.5	45–49	15.1	783.5	0.41 × 0.50	5.6	0.98 MHz (1.2 km s ⁻¹)
Band 7	2018 Apr 30 – (350 GHz)	64.1	0.6–1.0	43–44	15.1	500.2	0.46 × 0.52	5.4	0.98 MHz (0.85 km s ⁻¹)

^a Precipitable water vapor.

^b The average beam size of continuum achieved by TCLEAN with the Briggs weighting and the robustness parameter of 0.5. Note that we use a common circular restoring beam size of 0''.50 for Band 6 and 7 data to construct the final images.

^c Maximum Recoverable Scale.

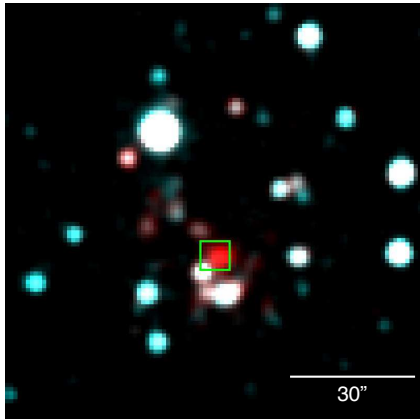


Figure 1. Near-infrared two-color image of the WB89-789 star-forming region based on 2MASS data (Skrutskie et al. 2006). Blue is *J*-band ($1.25\text{ }\mu\text{m}$) and red is *K*_s-band ($2.16\text{ }\mu\text{m}$). The image size is $100'' \times 100''$. The green square indicates the field-of-view of the ALMA submillimeter images shown in Figures 4–5.

center of antennas is RA = $06^{\text{h}}17^{\text{m}}23^{\text{s}}$ and Dec = $14^{\circ}54'41''$ (ICRS). The total on-source integration time is 115.5 minutes for Band 6 data and 64.1 minutes for Band 7. Flux and bandpass calibrators are J0510+1800, J0854+2006, and J0725-0054 for Band 6, while J0854+2006 and J0510+1800 for Band 7, respectively. Phase calibrators are J0631+2020 and J0613+1708 for Band 6 and J0643+0857 and J0359+1433 for Band 7. Four spectral windows are used to cover the sky frequencies of 241.40–243.31, 243.76–245.66, 256.90–258.81, and 258.76–260.66 GHz for Band 6, while 337.22–339.15, 339.03–340.96, 349.12–351.05, and 350.92–352.85 GHz for Band 7. The channel spacing is 0.98 MHz, which corresponds to 1.2 km s^{-1} for Band 6 and 0.85 km s^{-1} for Band 7. The total number of antennas is 45–49 for Band 6 and 43–44 for Band 7. The minimum–maximum baseline lengths are 15.1–783.5 m for Band 6 and 15.1–500.2 m for

Band 7. A full-width at half-maximum (FWHM) of the primary beam is about $25''$ for Band 6 and $18''$ for Band 7.

2.3. Data reduction

Raw data is processed with the *Common Astronomy Software Applications* (CASA) package. We use CASA 5.4.0 (Band 6) and 5.1.1 (Band 7) for the calibration and CASA 5.5.0 for the imaging. The synthesized beam sizes of $0''.39$ – $0''.42 \times 0''.49$ – $0''.52$ with a position angle of -36 degree for Band 6 and $0''.45$ – $0''.46 \times 0''.51$ – $0''.52$ with a position angle of -54 degree for Band 7 are achieved with the Briggs weighting and the robustness parameter of 0.5. In this paper, we use a common circular restoring beam size of 0''.50, which corresponds to 0.026 pc (5350 au) at the distance of WB89-789. The synthesized images are corrected for the primary beam pattern using the impbcor task in CASA. The continuum image is constructed by selecting line-free channels. Before the spectral extraction, the continuum emission is subtracted from the spectral data using the CASA's uvcontsub task.

The spectra and continuum flux are extracted from the 0''.50 diameter circular region centered at RA = $06^{\text{h}}17^{\text{m}}24.073$ and Dec = $14^{\circ}54'42.27$ (ICRS), which corresponds to the submillimeter continuum center of the target and is equivalent to the hot core position. Hereafter, the source is referred to as WB89-789 SMM1.

3. RESULTS AND ANALYSIS

3.1. Spectra

Figures 2–3 show submillimeter spectra extracted from the continuum center of WB89-789 SMM1. Spectral lines are identified with the aid of the Cologne Database for Molecu-

Table 2. Summary of detected molecular species

2 atoms	3 atoms	4 atoms	5 atoms	6 atoms	7 atoms	8 atoms	9 atoms
CN	HDO	H ₂ CO	c-C ₃ H ₂	CH ₃ OH	CH ₃ CHO	HCOOCH ₃	CH ₃ OCH ₃
NO	H ¹³ CO ⁺	HDCO	HC ₃ N	¹³ CH ₃ OH	c-C ₂ H ₄ O		C ₂ H ₅ OH
CS	HC ¹⁸ O ⁺	D ₂ CO	H ₂ CCO	CH ₂ DOH			C ₂ H ₅ CN
C ³⁴ S	H ¹³ CN	HNCO	HCOOH	CH ₃ CN			
C ³³ S	HC ¹⁵ N	H ₂ CS		NH ₂ CO			
SO	CCH						
³⁴ SO	SO ₂						
³³ SO	³⁴ SO ₂						
SiO	OCS						
	¹³ OCS						

lar Spectroscopy¹ (CDMS, Müller et al. 2001, 2005) and the molecular database of the Jet Propulsion Laboratory² (JPL, Pickett et al. 1998). The detection criterion adopted here is 3σ significance level and the velocity coincidence with the systemic velocity (V_{sys}) of WB89-789 SMM1 (34.5 km s^{-1}). The lines with the significance level higher than 2.5σ but lower than 3σ are indicated as tentative detection in the tables in Appendix A. More than 85 % of lines are detected above 5σ level.

Line parameters are measured by fitting a Gaussian profile to detected lines. We estimate the peak brightness temperature, the FWHM, the LSR velocity, and the integrated intensity for each line based on the fitting. For spectral lines for which a Gaussian profile does not fit well, their integrated intensities are calculated by directly integrating the spectrum over the frequency region of emission. Full details of the line fitting can be found in Appendix A (Tables of measured line parameters) and Appendix B (Figures of fitted spectra). The table also contains the estimated upper limits on important non-detection lines.

A variety of carbon-, oxygen-, nitrogen-, sulfur-, and silicon-bearing species, including COMs containing up to nine atoms, are detected from WB89-789 SMM1 (see Table 2). Multiple high excitation lines (upper state energy $>100 \text{ K}$) are detected for many species. Measured line widths are typically $3\text{--}6 \text{ km s}^{-1}$. Most of lines consist of a single velocity component, but SiO has doppler shifted components at $V_{sys} \pm 5 \text{ km s}^{-1}$ as indicated in Figure B1 in Appendix B.

3.2. Images

Figures 4–5 show synthesized images of continuum and molecular emission lines observed toward the target region. The images are constructed by integrating spectral data in the velocity range where the emission is detected. Most molecular lines, except for those of molecular radicals CN, CCH, and NO, have their intensity peak at the continuum center, which corresponds to the position of a hot core. Simple molecules such as H¹³CO⁺, H¹³CN, CS, and SO are extended compared to the beam size. Secondary intensity peaks are also seen in those species. Complex molecules and HDO are concentrated at the hot core position. A characteristic symmetric distribution is seen in SiO. Further discussion about the distribution of the observed emission is presented in Section 4.2.

3.3. Derivation of column densities, gas temperatures, and molecular abundances

3.3.1. Rotation diagram analysis

Column densities and rotation temperatures are estimated based on the rotation diagram analysis for the molecular species where multiple transitions with different excitation energies are detected (Figure 6). We here assume an optically thin condition and the local thermodynamic equilibrium (LTE). We use the following formulae based on the standard treatment of the rotation diagram analysis (e.g., Sutton et al. 1995; Goldsmith & Langer 1999):

$$\log\left(\frac{N_u}{g_u}\right) = -\left(\frac{\log e}{T_{\text{rot}}}\right)\left(\frac{E_u}{k}\right) + \log\left(\frac{N}{Q(T_{\text{rot}})}\right), \quad (1)$$

where

$$\frac{N_u}{g_u} = \frac{3k \int T_b dV}{8\pi^3 \nu S \mu^2}, \quad (2)$$

and N_u is a column density of molecules in the upper energy level, g_u is the degeneracy of the upper level, k is the Boltzmann constant, $\int T_b dV$ is the integrated intensity estimated

¹ <https://www.astro.uni-koeln.de/cdms>

² <http://spec.jpl.nasa.gov>

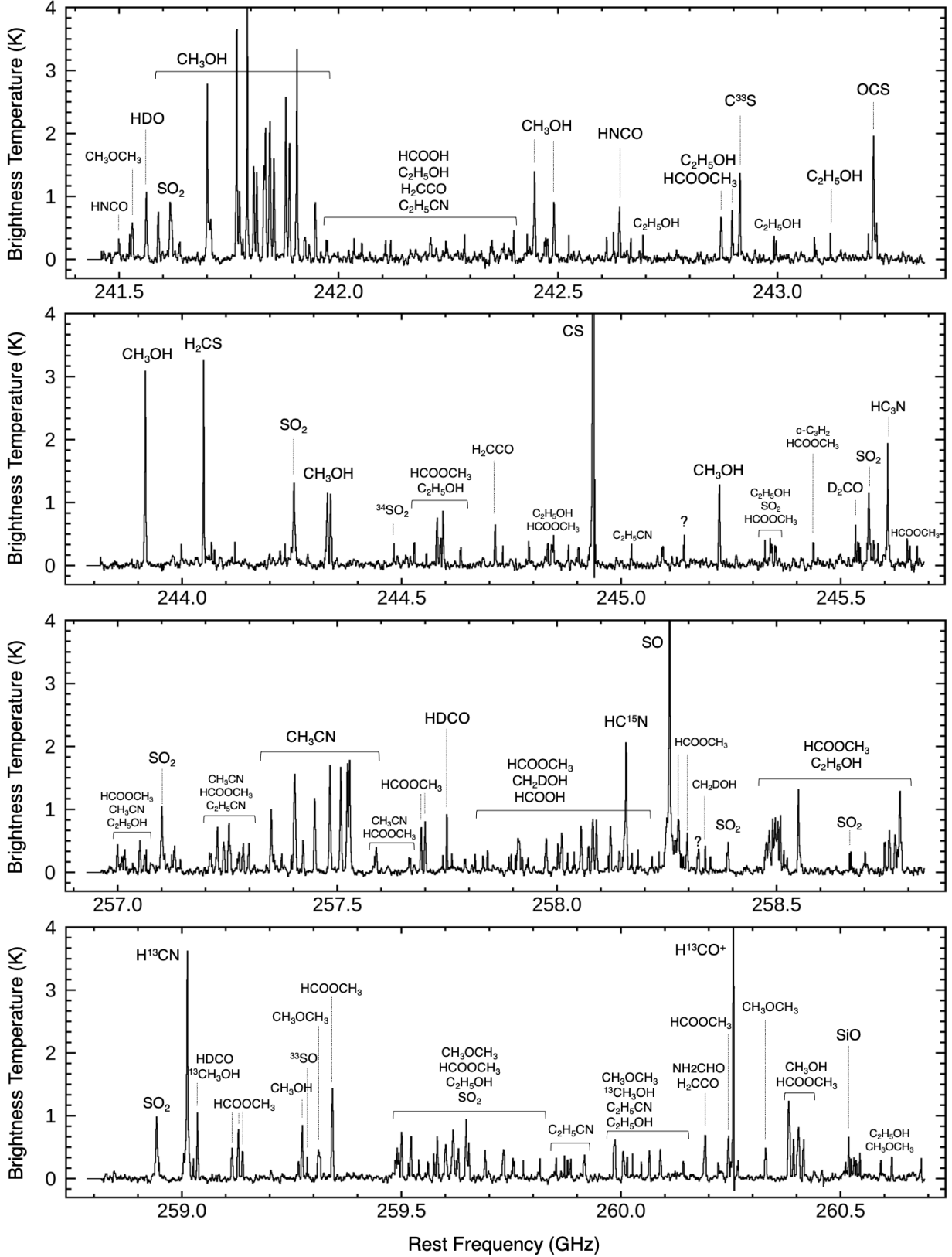


Figure 2. ALMA band 6 spectra extracted from the the 0'50 (0.026 pc) diameter region centered at the present hot molecular core in the extreme outer Galaxy, WB89-789 SMM1. Detected emission lines are labeled. Unidentified lines are indicated by "?". The source velocity of 34.5 km s⁻¹ is assumed.

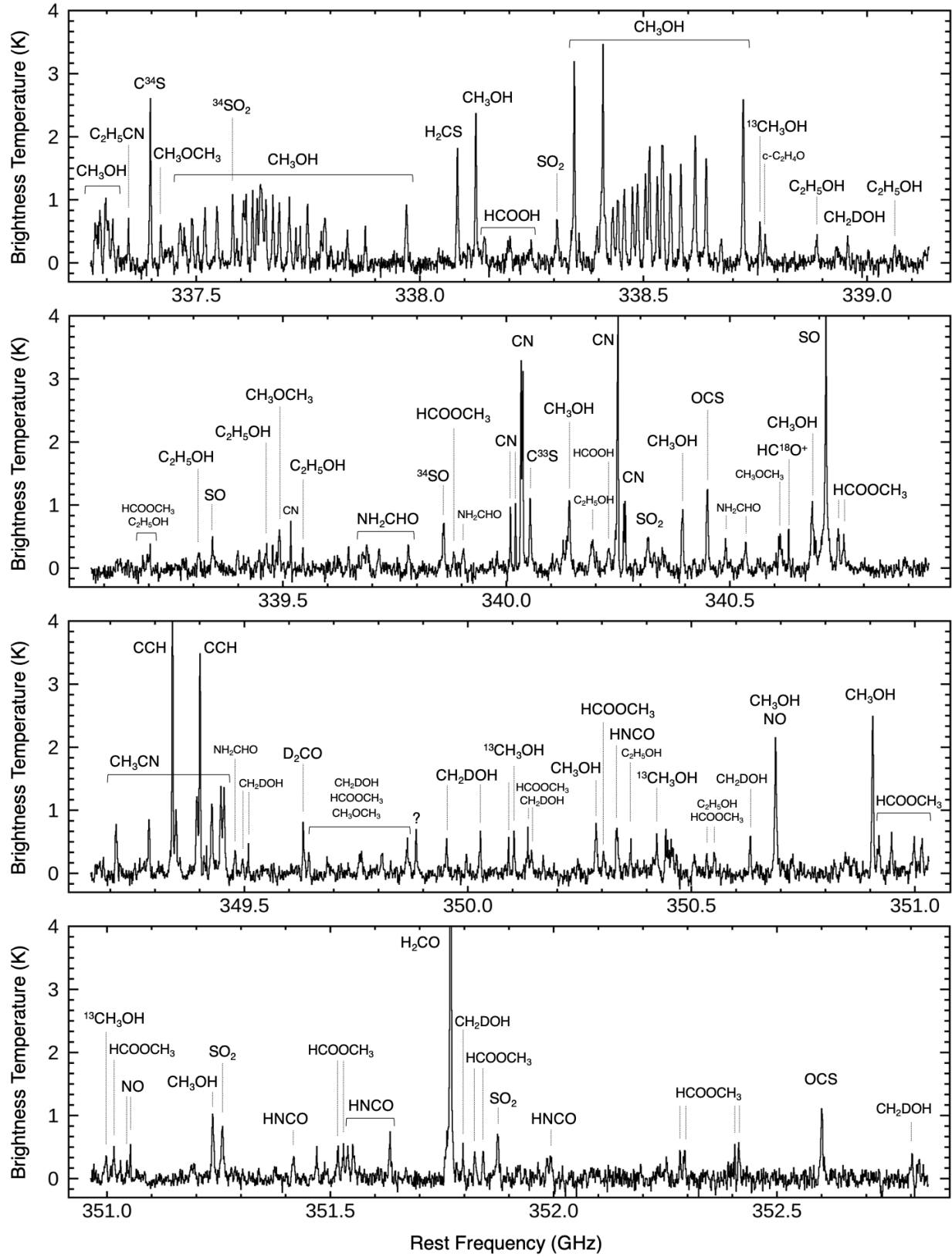


Figure 3. Same as in Figure 2, but for ALMA Band 7.

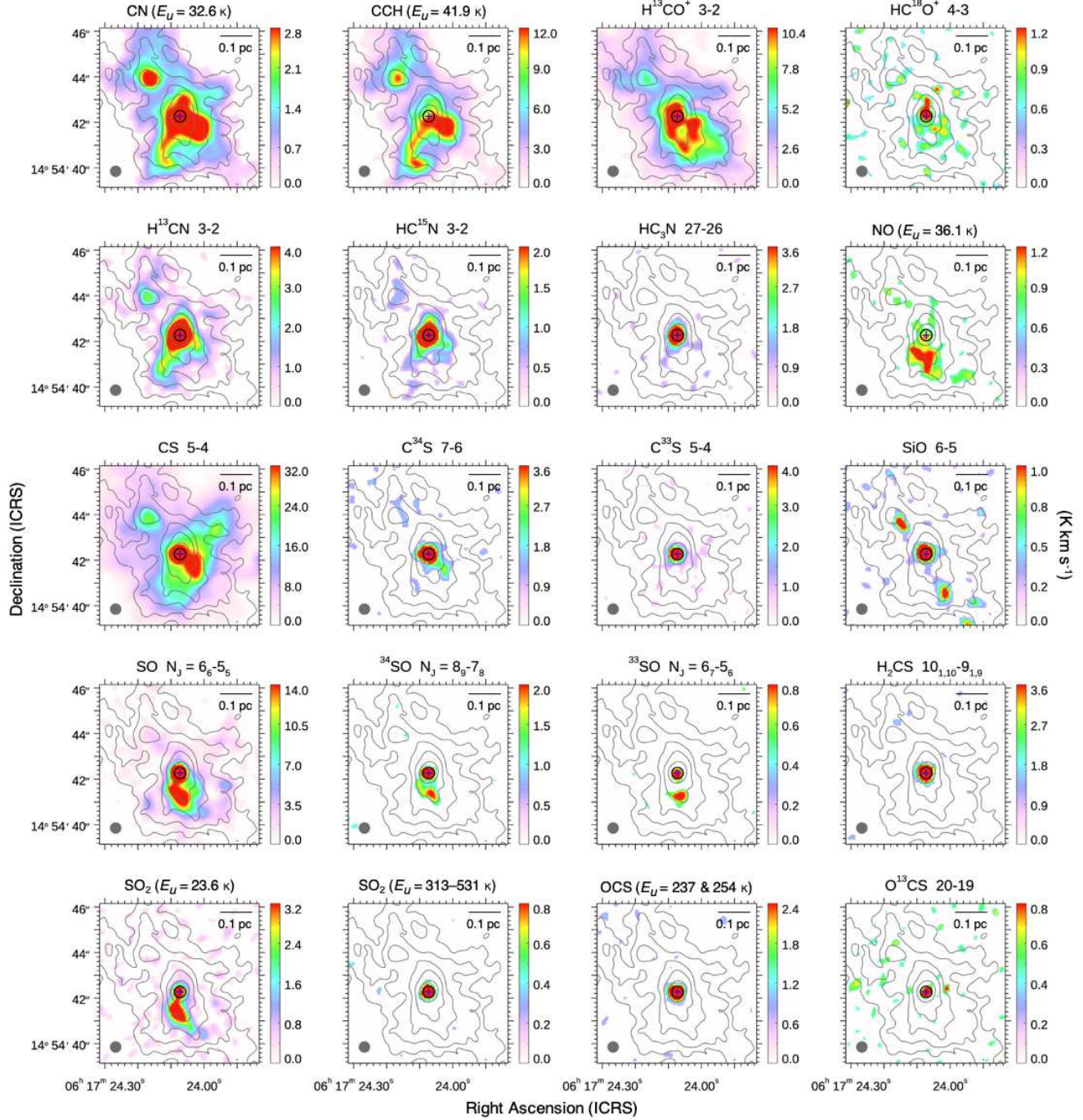


Figure 4. Integrated intensity distributions of molecular emission lines. Gray contours represent the 1.2 mm continuum distribution and the contour levels are 5σ , 10σ , 20σ , 40σ , 100σ of the rms noise (0.044 mJy/beam). Low signal-to-noise ratio regions ($S/N < 2$) are masked. The spectra discussed in the text are extracted from the region indicated by the black open circle. The blue cross represents the 1.2 mm continuum center. The synthesized beam size is shown by the gray filled circle in each panel. North is up, and east is to the left.

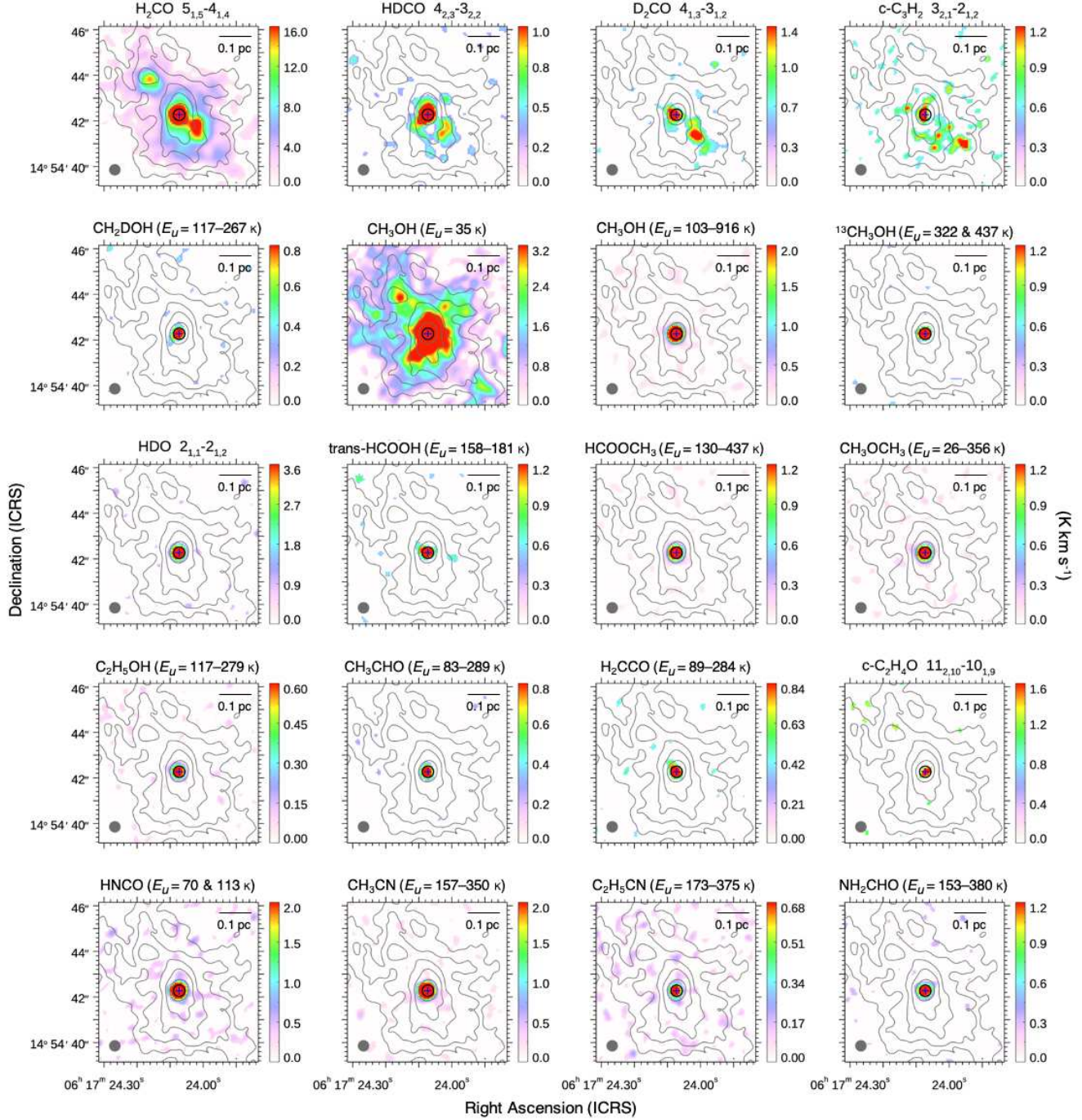


Figure 5. Same as in Figure 4.

from the observations, ν is the transition frequency, S is the line strength, μ is the dipole moment, T_{rot} is the rotational temperature, E_u is the upper state energy, N is the total column density, and $Q(T_{\text{rot}})$ is the partition function at T_{rot} . All the spectroscopic parameters required in the analysis are extracted from the CDMS or JPL database. Derived column densities and rotation temperatures are summarized in Table 3.

Most molecular species are well fitted by a single temperature component. Data points in diagrams of CH₃CN and C₂H₅CN are relatively scattered. For CH₃OH, CH₃CN, HNCO, SO₂, and HCOOCH₃, transitions with relatively large $S\mu^2$ values at low E_u (<300 K) are excluded from the fit in order to avoid possible effect of optical thickness (see gray points in Fig. 6). Adapted threshold values are $\log S\mu^2 > 1.1$ for CH₃OH, $\log S\mu^2 > 2.4$ for CH₃CN, $\log S\mu^2 > 1.6$ for HNCO, $\log S\mu^2 > 1.2$ for SO₂, and $\log S\mu^2 > 1.8$ for HCOOCH₃.

Complex organic molecules, HDO, and SO₂ show high rotation temperatures (>130 K). This suggests that they are originated from a warm region associated with a protostar. On the other hand, C³³S and D₂CO, and H₂CS show lower temperatures, suggesting that they arise from a colder region in the outer part of the protostellar envelope. SO also shows a low rotation temperature. Its T_{rot} is close to that of C³³S. However, SO lines are often optically thick in dense cores, particularly for low- E_u lines, thus the derived rotation temperature would be an upper limit.

3.3.2. Column densities of other molecules

Column densities of molecular species for which rotation diagram analysis is not applicable are estimated from Equation 1 after solving it for N . Their rotation temperatures are estimated as follows, by taking into account that the sight-line of WB89-789 SMM1 contains both cold and warm gas components as described in Section 3.3.1.

The rotation temperature of C³³S is applied to those of CS and C³⁴S, considering a similar distribution of isotopologues. Similarly, the rotation temperature of D₂CO is applied to H₂CO and HDCO, and that of SO₂ to ³⁴SO₂. For other species, we assume that molecules with an extended spatial distribution trace a relatively low-temperature region rather than a high-temperature gas associated with a hot core. CN, CCH, H¹³CO⁺, HC¹⁸O⁺, H¹³CN, HC¹⁵N, NO, SiO, ³⁴SO, ³³SO, and c-C₃H₂ correspond to this case. We assume a rotation temperature of 35 K for those species, which is roughly equivalent to that of C³³S.

High gas temperatures are observed for COMs, SO₂, and HDO, which are associated with a compact hot core region. Average temperature of those species is ~200 K. We assume this temperature for column density estimates (including upper limit) of c-C₂H₄O, HC₃N, ¹³CH₃CN, ¹³OCS, and

CH₃SH. Estimated column densities are summarized in Table 3.

We have also estimated column densities of selected species based on non-LTE calculations with RADEX (van der Tak et al. 2007). For input parameters, we use the H₂ gas density of 2.1×10^7 cm⁻³ according to our estimate in Section 3.3.3 and the background temperature of 2.73 K. Kinetic temperatures are assumed to be the same as temperatures tabulated in Table 3. The line intensities and widths are taken from the tables in Appendix A³. We assume an empirical 10% uncertainty for input line intensities. The resultant column densities are summarized in Table 3. The calculated non-LTE column densities are reasonably consistent with the LTE estimates.

3.3.3. Column density of H₂, dust extinction, and gas mass

A column density of molecular hydrogen (N_{H_2}) is estimated from the dust continuum data. We use the following equation to calculate N_{H_2} based on the standard treatment of optically thin dust emission:

$$N_{\text{H}_2} = \frac{F_{\nu}/\Omega}{2\kappa_{\nu}B_{\nu}(T_d)Z\mu m_{\text{H}}}, \quad (3)$$

where F_{ν}/Ω is the continuum flux density per beam solid angle as estimated from the observations, κ_{ν} is the mass absorption coefficient of dust grains coated by thin ice mantles at 1200/870 μm as taken from Ossenkopf & Henning (1994) and we here use 1.07 cm² g⁻¹ for 1200 μm and 1.90 cm² g⁻¹ for 870 μm , T_d is the dust temperature and $B_{\nu}(T_d)$ is the Planck function, Z is the dust-to-gas mass ratio, μ is the mean atomic mass per hydrogen (1.41, according to Cox 2000), and m_{H} is the hydrogen mass. We use the dust-to-gas mass ratio of 0.002, which is obtained by scaling the Galactic value of 0.008 by the metallicity of the WB89-789 region.

A line of sight towards a hot core contain dust grains with different temperatures because of the temperature gradient in a protostellar envelope. Representative dust temperature (i.e. mass-weighted average temperature) would fall somewhere in between that of a warm inner region and a cold outer region. Shimonishi et al. (2020) presented a detailed analysis of effective dust temperature in the sight-line of a low-metallicity hot core in the LMC, based on a comparison of N_{H_2} derived by submillimeter dust continuum with the above method, model fitting of spectral energy distributions (SEDs), and the 9.7 μm silicate dust absorption depth. The paper concluded that $T_d = 60$ K for the dust continuum

³ The following lines are used for non-LTE calculation with RADEX; H¹³CO⁺(3–2), HC¹⁸O⁺(4–3), H₂CO(5_{1,5}–4_{1,4}), c-C₃H₂(3_{2,1}–2_{1,2}), CN($N = 3$ –2, $J = \frac{5}{2} - \frac{3}{2}$, $F = \frac{5}{2} - \frac{3}{2}$), H¹³CN(3–2), HC¹⁵N(3–2), HC₃N(27–26), NO($J = \frac{7}{2} - \frac{5}{2}$, $\Omega = \frac{1}{2}$, $F = \frac{9}{2}^+ - \frac{7}{2}^-$), CH₃CN(14₀–13₀), SiO(6–5), CS(5–4), OCS(20–19), H₂CS(7_{1,6}–6_{1,5}), SO($N_J = 6_6 - 5_5$), and CH₃OH(7₅ E–6₅ E).

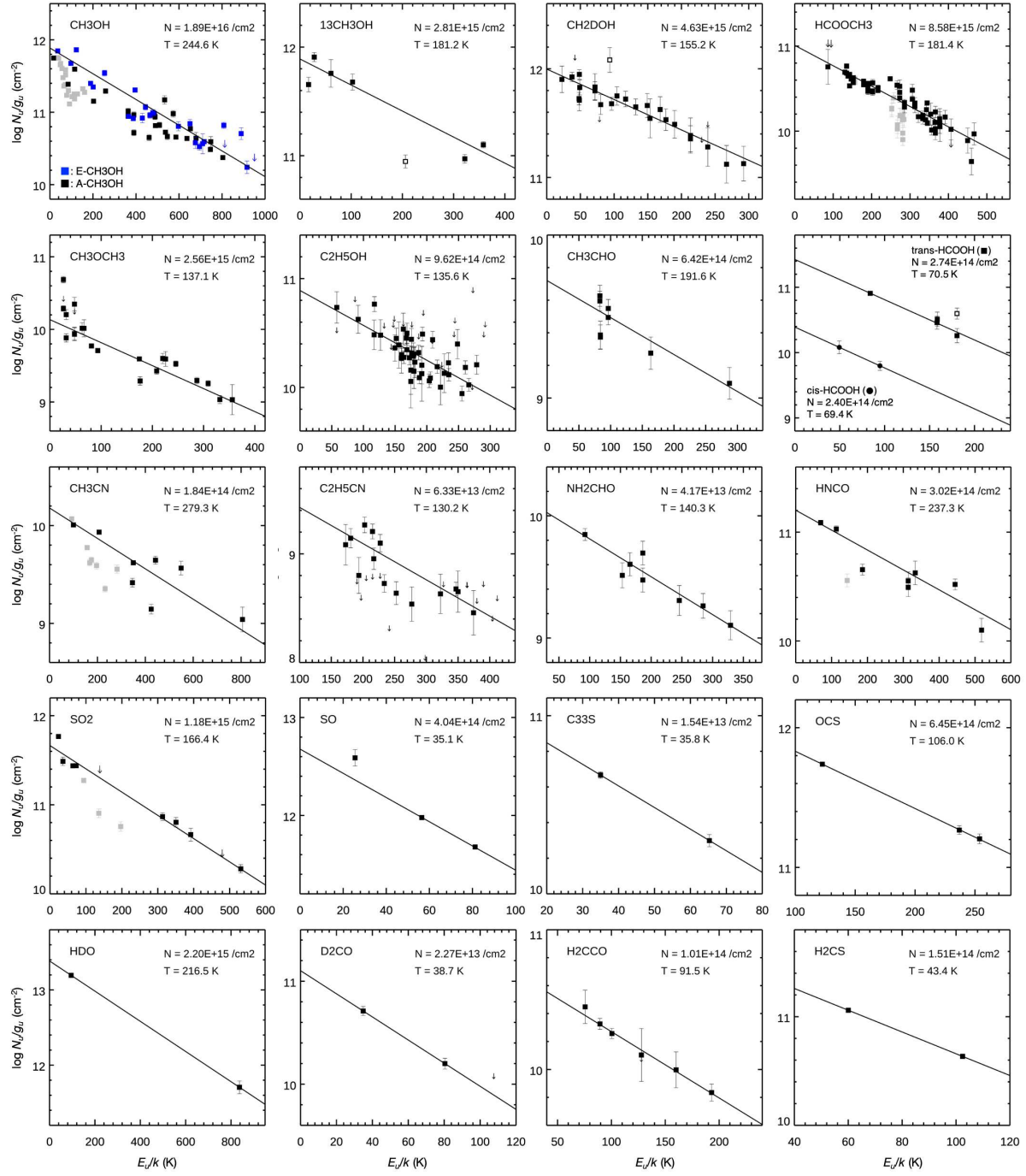


Figure 6. Results of rotation diagram analyses. Upper limit points are shown by the downward arrows. The solid lines represent the fitted straight line. Derived column densities and rotation temperatures are shown in each panel. The open squares are excluded in the fit because they significantly deviate from other data points. The gray squares are also excluded in the fit because of their large $S\mu^2$ values. CH₃OH is fitted by using only E-type transitions, which are shown in blue. For HCOOH, trans- (square) and cis- (circle) species are plotted together. See Section 3.3.1 for details.

analysis yields the N_{H_2} value which is consistent with those obtained by other different methods. This temperature corresponds to an intermediate value between a cold gas component (~ 50 K) represented by SO and a warm component (~ 150 K) represented by CH_3OH and SO_2 in this LMC hot core. The present hot core, WB89-789 SMM1, harbors similar temperature components as discussed in Sections 3.3.1 and 3.3.2. We thus applied $T_d = 60$ K for the present source. The continuum brightness of SMM1 is measured to be 11.33 ± 0.05 mJy/beam for $1200 \mu\text{m}$ and 28.0 ± 0.2 mJy/beam for $870 \mu\text{m}$ (3σ uncertainty). Based on the above assumption, we obtain $N_{\text{H}_2} = 1.6 \times 10^{24} \text{ cm}^{-2}$ for $1200 \mu\text{m}$ and $N_{\text{H}_2} = 1.2 \times 10^{24} \text{ cm}^{-2}$ for the $870 \mu\text{m}$. The N_{H_2} value changes by a factor of up to 1.6 when the assumed T_d is varied between 40 K and 90 K.

Alternatively, a column density of molecular hydrogen can be determined by the model fitting of the observed spectral energy distribution (SED). The best-fit SED discussed in Section 4.1 yields $A_V = 184$ mag. We here use a standard value of $N_{\text{H}}/E(B-V) = 5.8 \times 10^{21} \text{ cm}^{-2} \text{ mag}^{-1}$ (Draine 2003) and a slightly high $A_V/E(B-V)$ ratio of 4 for dense clouds (Whittet et al. 2001). Taking into account a factor of four lower metallicity, we obtain $N_{\text{H}_2}/A_V = 2.9 \times 10^{21} \text{ cm}^{-2} \text{ mag}^{-1}$, where we assume that all the hydrogen atoms are in the form of H_2 . Using this conversion factor, we obtain $N_{\text{H}_2} = 5.3 \times 10^{23} \text{ cm}^{-2}$. This N_{H_2} is similar to the N_{H_2} derived from the aforementioned method assuming $T_d = 150$ K. Such T_d may be somewhat high as a typical dust temperature in the line of sight, but it is not very unrealistic value given the observed temperature range of molecular gas towards WB89-789 SMM1.

In this paper, we use $N_{\text{H}_2} = 1.1 \times 10^{24} \text{ cm}^{-2}$ as a representative value, which corresponds to the average of N_{H_2} derived by the dust continuum data and the SED fitting. This N_{H_2} corresponds to $A_V = 380$ mag using the above conversion factor. Assuming the source diameter of 0.026 pc and the uniform spherical distribution of gas around a protostar, we estimate the gas number density to be $n_{\text{H}_2} = 2.1 \times 10^7 \text{ cm}^{-3}$, where the total gas mass of $13 M_\odot$ is enclosed.

Similarly, the mass for a 0.1 pc diameter region (i.e., a canonical size of dense cores) is estimated to be $75 M_\odot$ with $T_d = 60$ K, where Band 6 and Band 7 estimates are averaged. For the whole field shown in Figures 4–5, which roughly corresponds to a 0.5 pc diameter region, the total mass is estimated to be $800\text{--}2500 M_\odot$, where we assume $T_d = 20\text{--}10$ K for extended dust emission. Note that this is a lower limit because the maximum recoverable scale of the present observations is $5''.4$ (0.28 pc).

3.3.4. Fractional abundances and isotope abundance ratios

Fractional abundances with respect to H_2 are shown in Table 4, which are calculated based on column densities es-

timated in Sections 3.3.1–3.3.3. The fractional abundances normalized by the CH_3OH column density are also discussed in Sections 4.3–4.4, because of the non-negligible uncertainty associated with N_{H_2} (see Section 3.3.3).

Abundances of HCO^+ , HCN , SO , CS , OCS , and CH_3OH are estimated from their isotopologues, H^{13}CO^+ , H^{13}CN , ^{34}SO , C^{34}S , O^{13}CS , and $^{13}\text{CH}_3\text{OH}$. Detections of isotopologue species for SO , CS , OCS , and CH_3OH imply that the main species would be optically thick. Isotope abundance ratios of $^{12}\text{C}/^{13}\text{C} = 150$ and $^{32}\text{S}/^{33}\text{S} = 35$ are assumed, which are obtained by extrapolating the relationship between isotope ratios and galactocentric distances reported in Wilson & Rood (1994) and Humire et al. (2020) to $D_{GC} = 19$ kpc.

Abundance ratios are derived for several rare isotopologues; we obtain $\text{CH}_2\text{DOH}/\text{CH}_3\text{OH} = 0.011 \pm 0.002$, $\text{D}_2\text{CO}/\text{HDCO} = 0.45 \pm 0.10$, $^{34}\text{SO}/^{33}\text{SO} = 5 \pm 1$, $\text{C}^{34}\text{S}/\text{C}^{33}\text{S} = 2 \pm 1$, and $^{32}\text{SO}_2/^{34}\text{SO}_2 = 20 \pm 4$. The $^{32}\text{SO}_2/^{34}\text{SO}_2$ ratio in WB89-789 SMM1 is similar to the solar $^{32}\text{S}/^{34}\text{S}$ ratio (22, Wilson & Rood 1994), although we expect a slightly higher value in the outer Galaxy due to the $^{32}\text{S}/^{34}\text{S}$ gradient in the Galaxy (Chin et al. 1996; Humire et al. 2020). Astrophysical implication for the deuterated species are discussed in Section 4.4.

The rotation diagram of CH_3CN is rather scattered. Although its isotopologue line is not detected, optical thickness might affect the column density estimate, as CH_3CN is often optically thick in hot cores (e.g., Fuente et al. 2014). To obtain a possible range of its column density, we use the rotation diagram of $^{12}\text{CH}_3\text{CN}$ data to estimate a lower limit and the non-detection of the $^{13}\text{CH}_3\text{CN}(19_0\text{--}18_0)$ line at 339.36630 GHz ($E_u = 163$ K) for an upper limit.

We have also repeated the analysis for the spectra extracted from a 0.1 pc ($1''.93$) diameter region at the hot core position, for the sake of comparison with LMC hot cores (see Section 4.4). Those abundances are also summarized in Table 4. The abundances for a 0.1 pc area do not drastically vary from those for a 0.026 pc area. Molecules with compact spatial distribution (e.g., COMs) tend to decrease their abundances by a factor of $\sim 2\text{--}3$ in the 0.1 pc data due to the beam dilution effect. In contrast, those with extended spatial distributions and intensity peaks outside the hot core region (H^{13}CO^+ , CCH , CN , and NO) increases by a factor of ~ 2 in the 0.1 pc data.

4. DISCUSSION

4.1. Hot molecular core and protostar associated with WB89-789 SMM1

The nature of WB89-789 SMM1 is characterized as (i) the compact distribution of warm gas (~ 0.03 pc, see Section 4.2),

Table 3. Estimated rotation temperatures, column densities, and source sizes

Molecule	T_{rot}	$N(X)$	$N(X)$ non-LTE	Size
	(K)	(cm $^{-2}$)	(cm $^{-2}$)	($''$)
H ₂	...	1.1×10^{24}	...	0.85 ^c
H ¹³ CO ⁺	35	$(7.0 \pm 0.1) \times 10^{12}$	$(7.6 \pm 0.9) \times 10^{12}$	>1.5 ^d
HC ¹⁸ O ⁺	35	$(5.8 \pm 0.9) \times 10^{11}$	$(5.7 \pm 0.6) \times 10^{11}$	1.18 ^d
CCH	35	$(2.7 \pm 0.1) \times 10^{14}$...	>2 ^d
c-C ₃ H ₂	35	$(9.5 \pm 2.2) \times 10^{13}$	$(8.2 \pm 0.9) \times 10^{13}$ ^a	>1 ^d
H ₂ CO	39	$(1.1 \pm 0.1) \times 10^{14}$	$(1.3 \pm 0.1) \times 10^{14}$ ^a	>1.5 ^d
HDCO	39	$(5.1 \pm 0.3) \times 10^{13}$...	>1 ^d
D ₂ CO	39^{+6}_{-5}	$(2.3 \pm 0.5) \times 10^{13}$...	>1 ^d
CN	35	$(3.3 \pm 0.2) \times 10^{14}$	$(2.5 \pm 0.3) \times 10^{14}$	>2 ^d
H ¹³ CN	35	$(1.2 \pm 0.1) \times 10^{13}$	$(1.1 \pm 0.1) \times 10^{13}$	0.92 ^d
HC ¹⁵ N	35	$(6.3 \pm 0.2) \times 10^{12}$	$(5.8 \pm 0.6) \times 10^{12}$	0.75 ^d
HC ₃ N	200	$(2.7 \pm 0.3) \times 10^{13}$	$(2.1 \pm 0.2) \times 10^{13}$	0.65
NO	35	$(9.0 \pm 2.5) \times 10^{14}$	$(8.9 \pm 0.9) \times 10^{14}$	>1.5 ^d
HNCO	237^{+17}_{-15}	$(3.0 \pm 0.2) \times 10^{14}$...	0.54
CH ₃ CN	279^{+12}_{-11}	$(1.8 \pm 0.1) \times 10^{14}$	$(8.6 \pm 0.8) \times 10^{13}$	0.51
¹³ CH ₃ CN	200	<5 × 10 ¹²
C ₂ H ₅ CN	130^{+20}_{-15}	$(6.3 \pm 1.7) \times 10^{13}$...	0.52
NH ₂ CO	140^{+8}_{-7}	$(4.2 \pm 0.7) \times 10^{13}$...	0.56
SiO	35	$(2.5 \pm 0.2) \times 10^{12}$	$(2.5 \pm 0.3) \times 10^{12}$	0.65
CS	36	$(1.5 \pm 0.2) \times 10^{14}$	$(2.0 \pm 0.3) \times 10^{14}$	>1.5
C ³⁴ S	36	$(3.1 \pm 0.1) \times 10^{13}$...	0.70
C ³³ S	36^{+4}_{-3}	$(1.5 \pm 0.2) \times 10^{13}$...	0.61
OCS	106^{+6}_{-5}	$(6.5 \pm 0.5) \times 10^{14}$	$(6.4 \pm 0.7) \times 10^{14}$	0.55
¹³ OCS	200	$(8.7 \pm 2.4) \times 10^{13}$...	0.45
H ₂ CS	43^{+3}_{-2}	$(1.5 \pm 0.1) \times 10^{14}$	$(1.4 \pm 0.2) \times 10^{14}$ ^a	0.62
SO	35^{+1}_{-1}	$(4.0 \pm 0.3) \times 10^{14}$	$(4.5 \pm 0.5) \times 10^{14}$	0.70 ^d
³⁴ SO	35	$(5.9 \pm 0.1) \times 10^{13}$...	0.66
³³ SO	35	$(1.1 \pm 0.1) \times 10^{13}$...	0.53
SO ₂	166^{+5}_{-5}	$(1.2 \pm 0.1) \times 10^{15}$...	0.53
³⁴ SO ₂	166	$(5.9 \pm 0.9) \times 10^{13}$...	0.51
CH ₃ SH	200	<3 × 10 ¹⁴
HDO	217^{+14}_{-12}	$(2.2 \pm 0.2) \times 10^{15}$...	0.52
CH ₃ OH	245^{+4}_{-4}	$(1.9 \pm 0.1) \times 10^{16}$	$(2.6 \pm 0.1) \times 10^{16}$ ^b	0.51
¹³ CH ₃ OH	181^{+10}_{-9}	$(2.8 \pm 0.2) \times 10^{15}$...	0.46
CH ₂ DOH	155^{+18}_{-15}	$(4.6 \pm 0.3) \times 10^{15}$...	0.52
HCOOCH ₃	181^{+6}_{-5}	$(8.6 \pm 0.4) \times 10^{15}$...	0.51
CH ₃ OCH ₃	137^{+5}_{-4}	$(2.6 \pm 0.1) \times 10^{15}$...	0.52
C ₂ H ₅ OH	136^{+14}_{-12}	$(9.6 \pm 1.3) \times 10^{14}$...	0.50
CH ₃ CHO	192^{+52}_{-34}	$(6.4 \pm 0.8) \times 10^{14}$...	0.49
trans-HCOOH	71^{+11}_{-9}	$(2.7 \pm 0.6) \times 10^{14}$...	0.58
cis-HCOOH	69^{+50}_{-21}	$(2.4 \pm 1.2) \times 10^{13}$...	0.49
H ₂ CCO	92^{+14}_{-11}	$(1.0 \pm 0.2) \times 10^{14}$...	0.55
c-C ₂ H ₄ O	200	$(8.9 \pm 2.0) \times 10^{13}$...	0.47

Note—For T_{rot} and $N(X)$, those derived by rotation diagrams are shown in italics. Uncertainties and upper limits are of the 2 σ level and do not include systematic errors due to adopted spectroscopic constants. See Sections 3.3.1–3.3.3 and 4.2 for details.

^a Assuming ortho/para ratio of three.

^b Assuming E-CH₃OH/A-CH₃OH ratio of unity (Wirström et al. 2011).

^c Size of continuum emission.

^d Associated with extended component.

Table 4. Estimated fractional abundances

Molecule	$N(X)/N_{\text{H}_2}$	
	0.026 pc area	0.1 pc area
HCO ^a	$(9.5 \pm 3.2) \times 10^{-10}$	$(1.5 \pm 0.3) \times 10^{-9}$
H ₂ CO	$(1.0 \pm 0.3) \times 10^{-10}$	$(1.2 \pm 0.1) \times 10^{-10}$
HDCO	$(4.7 \pm 1.3) \times 10^{-11}$	$(3.9 \pm 0.2) \times 10^{-11}$
D ₂ CO	$(2.1 \pm 0.7) \times 10^{-11}$	$(2.0 \pm 0.3) \times 10^{-11}$
C ₂ H	$(2.5 \pm 0.7) \times 10^{-10}$	$(5.8 \pm 1.2) \times 10^{-10}$
c-C ₃ H ₂	$(8.6 \pm 3.1) \times 10^{-11}$	$(5.9 \pm 1.2) \times 10^{-11}$
CN	$(3.0 \pm 0.8) \times 10^{-10}$	$(6.6 \pm 1.3) \times 10^{-10}$
HCN ^a	$(1.7 \pm 0.6) \times 10^{-9}$	$(1.2 \pm 0.3) \times 10^{-9}$
HC ₃ N	$(2.5 \pm 0.7) \times 10^{-11}$	$(1.4 \pm 0.1) \times 10^{-11}$
NO	$(8.1 \pm 3.2) \times 10^{-10}$	$(1.6 \pm 0.1) \times 10^{-9}$
HNCO	$(2.7 \pm 0.8) \times 10^{-10}$	$(7.1 \pm 0.6) \times 10^{-11}$
CH ₃ CN ^b	$(4.2 \pm 2.7) \times 10^{-10}$	$(3.7 \pm 2.8) \times 10^{-10}$
C ₂ H ₅ CN	$(5.8 \pm 2.2) \times 10^{-11}$	$(2.4 \pm 0.9) \times 10^{-11}$
NH ₂ CHO	$(3.8 \pm 1.2) \times 10^{-11}$	$(1.8 \pm 0.1) \times 10^{-11}$
SiO	$(2.2 \pm 0.6) \times 10^{-12}$	$(1.2 \pm 0.1) \times 10^{-12}$
CS ^c	$(9.7 \pm 3.3) \times 10^{-10}$	$(6.4 \pm 1.3) \times 10^{-10}$
SO ^c	$(1.9 \pm 0.5) \times 10^{-9}$	$(1.3 \pm 0.3) \times 10^{-9}$
OCS ^a	$(1.2 \pm 0.5) \times 10^{-8}$	$(4.1 \pm 1.4) \times 10^{-9}$
H ₂ CS	$(1.4 \pm 0.4) \times 10^{-10}$	$(9.0 \pm 1.0) \times 10^{-11}$
SO ₂	$(1.1 \pm 0.3) \times 10^{-9}$	$(2.9 \pm 0.1) \times 10^{-10}$
CH ₃ SH	<3 × 10 ⁻¹⁰	<2 × 10 ⁻¹⁰
HDO	$(2.0 \pm 0.6) \times 10^{-9}$	$(7.7 \pm 0.9) \times 10^{-10}$
CH ₃ OH ^a	$(3.8 \pm 1.3) \times 10^{-7}$	$(1.7 \pm 0.3) \times 10^{-7}$
CH ₂ DOH	$(4.2 \pm 1.2) \times 10^{-9}$	$(1.5 \pm 0.2) \times 10^{-9}$
HCOOCH ₃	$(7.8 \pm 2.2) \times 10^{-9}$	$(3.0 \pm 0.2) \times 10^{-9}$
CH ₃ OCH ₃	$(2.3 \pm 0.6) \times 10^{-9}$	$(1.0 \pm 0.1) \times 10^{-9}$
C ₂ H ₅ OH	$(8.7 \pm 2.7) \times 10^{-10}$	$(3.3 \pm 0.8) \times 10^{-10}$
CH ₃ CHO	$(5.8 \pm 1.8) \times 10^{-10}$	$(2.1 \pm 0.4) \times 10^{-10}$
HCOOH ^d	$(2.7 \pm 1.0) \times 10^{-10}$	$(1.2 \pm 0.4) \times 10^{-10}$
H ₂ CCO	$(9.2 \pm 3.0) \times 10^{-11}$	$(3.7 \pm 0.9) \times 10^{-11}$
c-C ₂ H ₄ O	$(8.1 \pm 2.8) \times 10^{-11}$	$(5.9 \pm 1.2) \times 10^{-11}$

Note—Uncertainties and upper limits are of the 2 σ level. Column densities of molecules for a 0.026 pc area are summarized in Table 3. An empirical uncertainty of 30 % is assumed for N_{H_2} .

^a Estimated from ¹³C isotopologue with ¹²C/¹³C = 150

^b Rotation diagram analysis of CH₃CN is used to derive a lower limit and the non-detection of ¹³CH₃CN for an upper limit.

^c Estimated from ³⁴S isotopologue with ³²S/³⁴S = 35

^d Sum of *trans*- and *cis*-species.

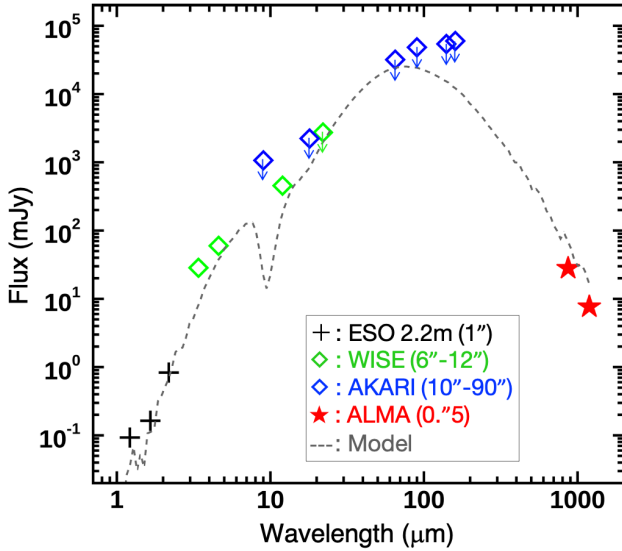


Figure 7. The SED of WB89-789 SMM1. The plotted data are obtained by the ESO 2.2 m telescope (pluses, black; Brand & Wouterloot 2007), the WISE all-sky survey (open diamonds, light green; Wright et al. 2010), AKARI FIS all-sky survey (open diamonds, blue; Yamamura et al. 2010), and ALMA (filled star, red, this work). The angular resolution of each data is indicated in brackets. The gray dashed line indicates the best-fitted SED with the model of Robitaille et al. (2007).

(ii) the high gas temperature that can trigger the ice sublimation (≥ 100 K, Section 3.3.1), (iii) the high density (2×10^7 cm $^{-3}$, Section 3.3.3), (iv) the association with a luminous protostar (see below), and (v) the presence of chemically rich molecular gas. Those properties suggest that the source is associated with a hot molecular core.

Figure 7 shows a SED of SMM1, where the data are collected from available databases and literatures (Brand & Wouterloot 2007; Wright et al. 2010; Yamamura et al. 2010). The bolometric luminosity of the source is estimated to be 8.4×10^3 L $_{\odot}$ based on the SED fitting with the model of Robitaille et al. (2007). This luminosity is equivalent to a stellar mass of about 10 M $_{\odot}$ according to the mass-luminosity relationship of zero age main sequence (ZAMS) stars (Zinnecker & Yorke 2007).

Note that far-infrared data, which is important for the luminosity determination of embedded sources, is insufficient for SMM1. Only upper limits are provided due to the low angular resolution of available AKARI FIS all-sky survey data. Thus the derived luminosity (and therefore mass) may be lower than the current estimate. Future high spatial resolution infrared observations in those missing wavelengths are highly required.

Alternatively, we can estimate the luminosity of SMM1 by scaling the luminosity of a low-metallicity LMC hot core,

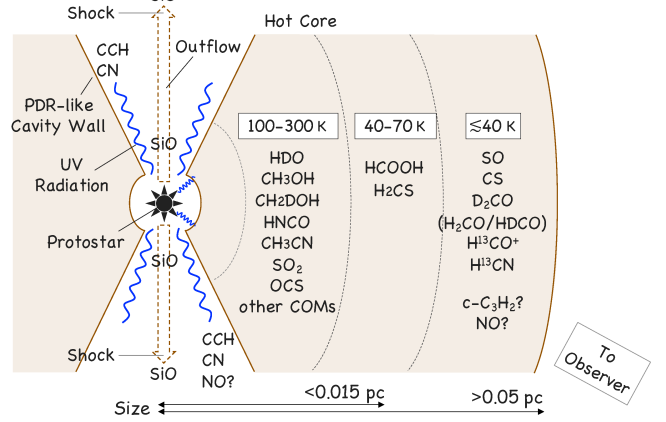


Figure 8. Schematic illustration of the molecular gas distribution and the temperature structure in WB89-789 SMM1.

ST16, whose SED is well determined based on a comprehensive infrared dataset from 1 to 1200 μm (Shimonishi et al. 2020). This LMC hot core has a total luminosity of 3.1×10^5 L $_{\odot}$ and a K_s -band magnitude ($[K_s]$) of 13.4 mag at 50 kpc, while SMM1 has $[K_s] = 14.7$ mag at 10.7 kpc. Scaling the luminosity of ST16 with the distance and K_s -band magnitude, we obtain 4.3×10^3 L $_{\odot}$ for SMM1, which is a factor of two lower than the estimate by the SED fitting. In either case, present estimates suggest that the luminosity of SMM1 would correspond to the lower-end of high-mass ZAMS or upper-end of intermediate-mass ZAMS.

4.2. Distribution of molecular line emission and dust continuum

The observed emission lines and continuum show different spatial distributions depending on species. Those distributions have important clues to understand their origins. A schematic illustration of the temperature structure and molecular gas distribution in WB89-789 SMM1 are shown in Figure 8 based on the discussion in this section.

We have estimated the spatial extent of observed emission by fitting a two-dimensional Gaussian to the continuum center (Table 3). Compact distributions (FWHM = 0'.5–0'.6, 0.026–0.031 pc), that is comparable with the beam size, are seen in HDO, COMs, CH₃CN, HNCO, OCS, and high-excitation SO₂ lines. HC₃N is slightly extended (FWHM = 0'.65). They are concentrated at the hot core position, suggesting that they are originated from a warm region where ice mantles are sublimated.

SO, ³⁴SO, ³³SO, and low-excitation SO₂ show relatively compact distributions (FWHM = 0'.5–0'.7, 0.026–0.036 pc) at the hot core position, but also show a secondary peak at the south side of the hot core. This secondary peak coincides with the peak of the NO emission. Other sulfur-bearing species such as C³⁴S, C³³S, and H₂CS show compact distri-

butions ($\text{FWHM} = 0''.6\text{--}0''.7$, $0.031\text{--}0.052$ pc) centered at the hot core.

A characteristic distribution that is symmetric to the hot core position is seen in SiO. It shows a compact emission ($\text{FWHM} = 0''.65$) at the hot core center, but also shows other peaks at the north-east and south-west sides of the hot core. Those secondary peaks are slightly elongated. SiO is a well-known shock tracer. The observed structure would be originated from the shocked gas produced by bipolar protostellar outflows. A driving source of the outflows would be a protostar embedded in a hot core, since the distribution of SiO is symmetric to the hot core position.

Even extended distributions ($\text{FWHM} > 1''.0$) are seen in CN, CCH, H^{13}CO^+ , HC^{18}O^+ , H^{13}CN , HC^{15}N , NO, CS, H_2CO , and HDCO , D_2CO , and low-excitation CH_3OH . Gas-phase reactions and non-thermal desorption of icy species would have non-negligible contribution to the formation of those species, because they are widely distributed beyond the hot core. We note that dust continuum, H^{13}CN , HC^{15}N have a moderately sharp peak ($\text{FWHM} < 1''.0$) at the hot core position in addition to the extended component. $\text{c-C}_3\text{H}_2$ shows a patchy distribution, whose secondary peak at the south-west of the hot core does not coincide with those of other species.

Molecular radicals (CN, CCH, and NO) do not have their emission peak at the hot core position. This would suggest that the chemistry outside the hot core region largely contributes to their production. CN and CCH are known to be abundant in photodissociation regions (PDRs), because atomic carbon is efficiently provided by photodissociation of CO under moderate UV fields (e.g., Fuente et al. 1993; Sternberg & Dalgarno 1995; Jansen et al. 1995; Rodriguez-Franco et al. 1998; Pety et al. 2017). In the present source, their emission shows a similar spatial distribution. A similar distribution between CN and CCH has been also observed in a LMC hot core (Shimonishi et al. 2020); they argue that CN and CCH would trace PDR-like outflow cavity structures that are irradiated by the UV light from a protostar associated with a hot core. We speculate that this is also the case for WB89-789 SMM1.

Figure 9 shows velocity maps (moment 1) of CN and CCH lines. CN and CCH emission are elongated in the south-west direction from the hot core (see also Figure 4). The figure also shows a possible direction of protostellar outflows expected from the spatial distribution of SiO. The elongated directions of CN and CCH coincide with the inferred direction of outflows. In addition, the elongated south-west parts of CN and CCH are blue-shifted by $\sim 1\text{--}2 \text{ km s}^{-1}$ compared to the hot core position. This may be due to outflow gas motion, although CN and CCH would trace an outflow cavity wall rather than outflow gas itself. Actually the observed velocity shift is smaller than a typical value of high-velocity wing components in massive protostellar outflows ($\geq 5 \text{ km s}^{-1}$,

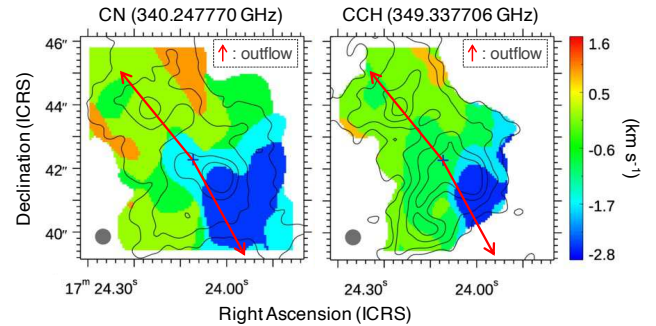


Figure 9. Velocity maps (moment 1) of CN and CCH lines. The color scale indicates the offset velocity relative to the systemic velocity of 34.5 km s^{-1} . A possible direction of outflows expected from the distributions of SiO is shown by the red arrows. Contours represent the integrated intensity distribution and the contour levels are 8%, 20%, 40%, and 60% of the peak value. Low signal-to-noise regions ($S/N < 5$) are masked. The blue cross represents the 1.2 mm continuum center.

s^{-1} , e.g., Beuther et al. 2002; Maud et al. 2015). We note that a clear velocity structure is not seen in the SiO velocity map, except for the position of another embedded protostar discussed in Section 4.5. Future observations of optically-thick outflow tracers such as CO are necessary to confirm the presence of high-velocity gas associated with protostellar outflows.

4.3. Molecular abundances: Comparison with Galactic hot cores

Figure 10 shows a comparison of molecular abundances between WB89-789 SMM1 and other known Galactic hot cores. The data for an intermediate-mass hot core, NGC7192 FIRS2, is adopted from Fuente et al. (2014). The abundances are based on the 220 GHz region observations for a 0.009 pc diameter area centered at the hot core. The luminosity of NGC7192 FIRS2 ($\sim 500 L_\odot$) corresponds to that of a $5 M_\odot$ ZAMS. The data for a high-mass source, the Orion hot core, is adopted from Sutton et al. (1995), which is based on the 340 GHz region observations for a 0.027 pc diameter area at the hot core. The abundance of HNCO is taken from Schutte & Greenberg (1997).

The molecular abundances in WB89-789 SMM1 is generally lower than those of inner Galactic counterparts. The degree of the abundance decrease is roughly consistent with the lower metallicity of the WB89-789 region as indicated by the scale bar in Figure 10. Particularly, SMM1 and the intermediate-mass hot core NGC7192 FIRS2 show similar molecular abundances after taking into account the four times lower metallicity of the former source. For the comparison with Orion, it seems that HC_3N , $\text{C}_2\text{H}_5\text{CN}$, and SO_2 are significantly less abundant in SMM1 even taking into ac-

count the lower metallicity, while CH_3OH is overabundant in SMM1 despite the low metallicity.

To further focus on chemical complexity at low metallicity, Figure 11 shows a comparison of fractional abundances of COMs normalized by the CH_3OH column density for WB89-789 SMM1 and NGC7192 FIRS2. Such a comparison is useful for investigating chemistry of organic molecules in warm and dense gas around protostars (Herbst & van Dishoeck 2009; Drozdovskaya et al. 2019), because CH_3OH is believed to be a parental molecule for the formation of even larger COMs (e.g., Nomura & Millar 2004; Garrod & Herbst 2006). In addition, CH_3OH is a product of grain surface reaction, thus warm CH_3OH gas mainly arise from a high-temperature region, where ices are sublimated and characteristic hot core chemistry proceeds. Furthermore, the normalization by CH_3OH can cancel the metallicity effect in the abundance comparison.

The $N(\text{X})/N(\text{CH}_3\text{OH})$ ratios are remarkably similar between WB89-789 SMM1 and NGC7192 FIRS2 as shown in Figure 11 (a). The ratios of SMM1 coincide with those of NGC7192 FIRS2 within a factor of 2 for the most molecular species. The correlation coefficient is calculated to be 0.94, while it is 0.96 if CH_3CN is excluded. It seems that CH_3CN deviates from the overall trend, although the uncertainty is large due to the opacity effect (see 3.3.4). $\text{C}_2\text{H}_5\text{OH}$ also slightly deviates from the trend. The reason for their behavior is still unclear, but it may be related to the formation pathway of those molecules.

The above two comparisons suggest that chemical compositions of the hot core in the extreme outer Galaxy scale with the metallicity. In the WB89-789 region, the metallicity is expected to be four times lower compared to the solar neighborhood. The observed abundances of COMs in the SMM1 hot core is lower than the other Galactic hot cores, but the decrease is proportional to this metallicity. Furthermore, similar $N(\text{COMs})/N(\text{CH}_3\text{OH})$ ratios suggest that CH_3OH is an important parental species for the formation of larger COMs in a hot core, as suggested by aforementioned theoretical studies.

CH_3OH ice is believed to form on grain surfaces and several formation processes are proposed by laboratory experiments; i.e., hydrogenation of CO, ultraviolet photolysis and radiolysis of ice mixtures (e.g., Hudson & Moore 1999; Watanabe et al. 2007). It is known that CH_3OH is already formed in quiescent prestellar cores before star formation occurs (Boogert et al. 2011). Solid CH_3OH will chemically evolve to larger COMs by a combination of photolysis, radiolysis, and grain heating during the warm-up phase that leads to the formation of a hot core (Garrod & Herbst 2006). High-temperature gas-phase chemistry of sublimated CH_3OH would also contribute to the COMs formation (Nomura & Millar 2004; Taquet et al. 2016). The present re-

sults suggest that various COMs can form even in a low-metallicity environment, if their parental molecule, CH_3OH , is efficiently produced in a star-forming core. The detection of a chemically-rich star-forming core in the extreme outer Galaxy has an impact on the understanding of the occurrence of the chemical complexity in a primordial environment of the early phase of the Galaxy formation. We here note that observations of ice mantle compositions are not reported for the outer Galaxy so far. Future infrared observations of ice absorption bands towards embedded sources in the outer Galaxy are important.

4.4. Molecular abundances: Comparison with LMC hot cores

It is still unknown if the observed simply-metallicity-scaled chemistry of COMs in the WB89-789 SMM1 hot core is common in other hot core sources in the outer Galaxy. A comparison of the present data with those of hot cores in the LMC would provide a hint for understanding the universality of low-metallicity hot core chemistry. The metallicity of the LMC is reported to be lower than the solar value by a factor of two to three (e.g., Dufour et al. 1982; Westerlund 1990; Russell & Dopita 1992; Choudhury et al. 2016), which is in common with the outer Galaxy.

Figure 12 shows a comparison of molecular abundances between WB89-789 SMM1 and three LMC hot cores. The plotted molecular column densities for LMC hot cores are adopted from Shimonishi et al. (2016a) for ST11, Shimonishi et al. (2020) for ST16, and Sewilo et al. (2018) for N113 A1. Another LMC hot core in Sewilo et al. (2018), N113 B3, have similar molecular abundances with those of N113 A1. The N_{H_2} value of ST11 and N113 A1 is re-estimated using the same dust opacity data and dust temperature ($T_d = 60$ K) as in this work; We obtained $N_{\text{H}_2} = 1.2 \times 10^{24} \text{ cm}^{-2}$ for ST11 and $N_{\text{H}_2} = 9.2 \times 10^{23} \text{ cm}^{-2}$ for N113 A1. The dust temperature assumed in ST16 is 60 K as described in Section 3.3.3. Molecular column densities are estimated for circular/elliptical regions of 0.12×0.12 pc, 0.10×0.10 pc, and 0.21×0.13 pc for ST11, ST16, and N113 A1, respectively. For a fair comparison, we have re-calculated N_{H_2} and molecular column densities of SMM1 for a 0.1 pc ($1.^{\prime\prime}93$) diameter region. Those abundances are plotted in Figure 12 and summarized in Table 4.

The chemical composition of the outer Galaxy hot core does not resemble those of LMC hot cores as seen in Figure 12. The dissimilarity is also seen in the $N(\text{X})/N(\text{CH}_3\text{OH})$ comparison between SMM1 and ST16 as shown in Figure 11 (b), where the correlation coefficient is calculated to be 0.69.

Shimonishi et al. (2020) argue that SO_2 will be a good tracer of low-metallicity hot core chemistry, because (i) it is commonly detected in LMC hot cores with similar abundances, and (ii) it is originated from a compact hot core re-

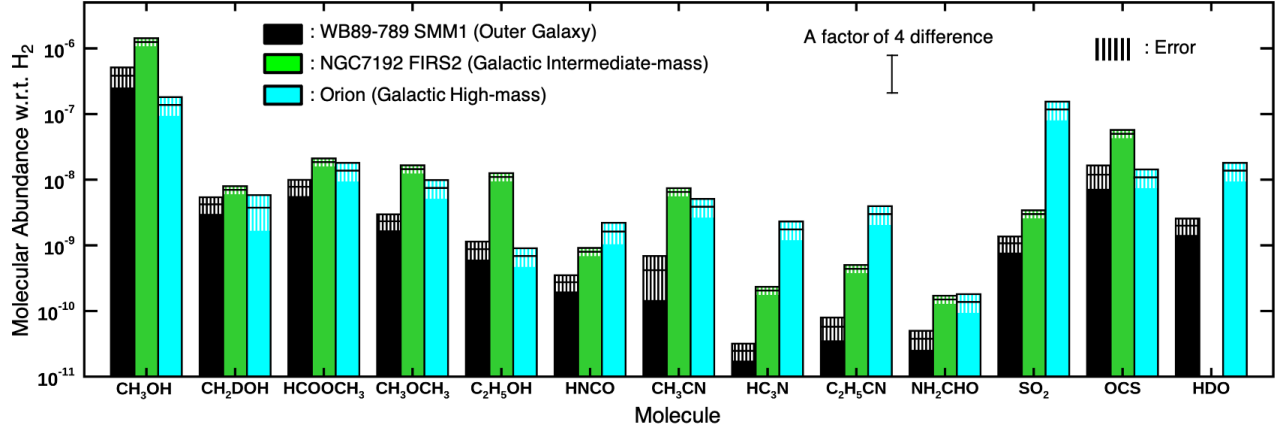


Figure 10. Comparison of molecular abundances between an outer Galactic hot core (black, WB89-789 SMM1), an intermediate-mass hot core (green, NGC7192 FIRS2), and a high-mass hot core (cyan, Orion). An abundance difference by a factor of four is indicated by the black solid line with hats. The area with thin vertical lines indicate the error bar. No data is available for HDO in NGC7192 FIRS2. See Section 4.3 for details.

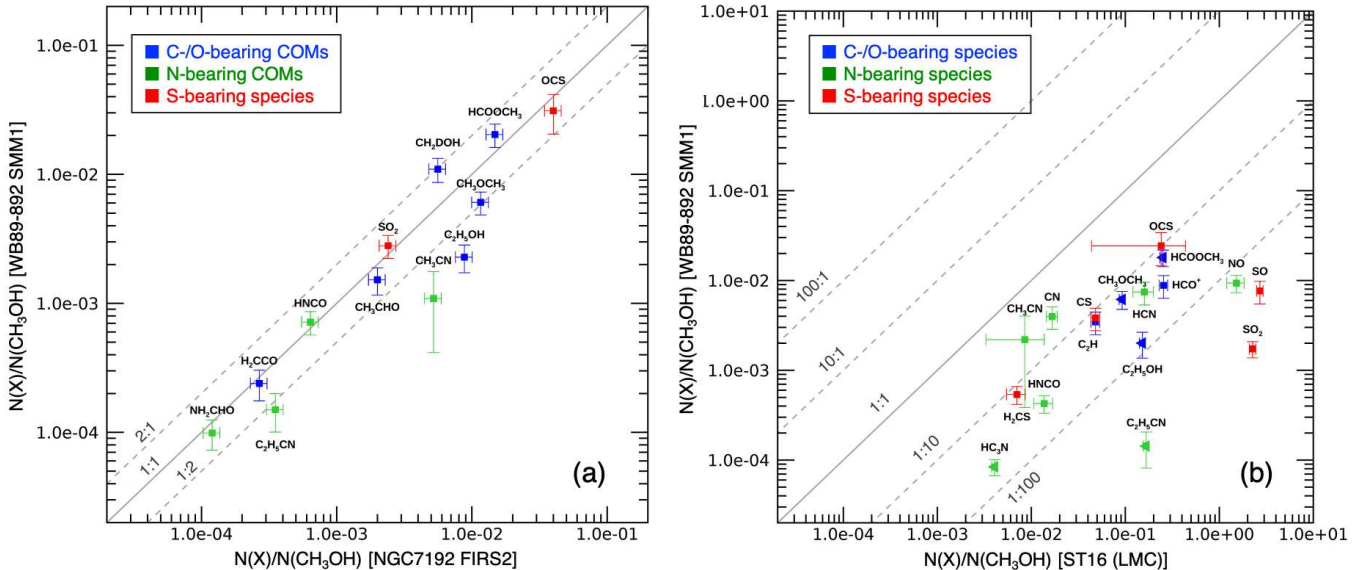


Figure 11. Comparison of molecular abundances normalized by the CH_3OH column density for (a) WB89-789 SMM1 vs. NGC7192 FIRS2 and (b) WB89-789 SMM1 vs. ST16 (LMC). Carbon- and oxygen-bearing species are shown by the blue squares, nitrogen-bearing species in green, and sulfur-bearing species in red. The dotted lines in the panel (a) represent an abundance ratio of 2:1 and 1:2 for WB89-789 SMM1 : NGC7192 FIRS2, while the solid line represent that of 1:1. Similarly, the dotted lines in the panel (b) represent a ratio of 100:1, 10:1, 1:10, and 1:100 for WB89-789 SMM1:ST16, while 1:1 for the solid line. The leftward triangles in the panel (b) indicate the upper limit for ST16. See Section 4.3 for details.

gion. SO also shows similar abundances within LMC hot cores. In WB89-789 SMM1, however, the abundances of SO_2 and SO relative to H_2 are lower by a factor of 28 and 5 compared with LMC hot cores. The measured rotation temperatures of SO_2 are similar between those hot cores, i.e., 166 K (SO_2) for SMM1, 232 K (SO_2) and 86 K ($^{34}\text{SO}_2$) for ST16, 190 K (SO_2) and 95 K ($^{34}\text{SO}_2$) for ST11. The SO_2 column densities for ST16 and ST11 are estimated from $^{34}\text{SO}_2$, while

that for SMM1 is from SO_2 . However, the SO_2 column density of SMM1 increases only by a factor of up to three when it is estimated from $^{34}\text{SO}_2$ (see Section 3.3.4). Thus the low SO_2 abundance in the outer Galactic hot core would not be due to the optical thickness.

In contrast to the S-O bond bearing species, the C-S bond bearing species such as CS, H_2CS , and OCS do not show significant abundance decrease in WB89-789 SMM1. Thus

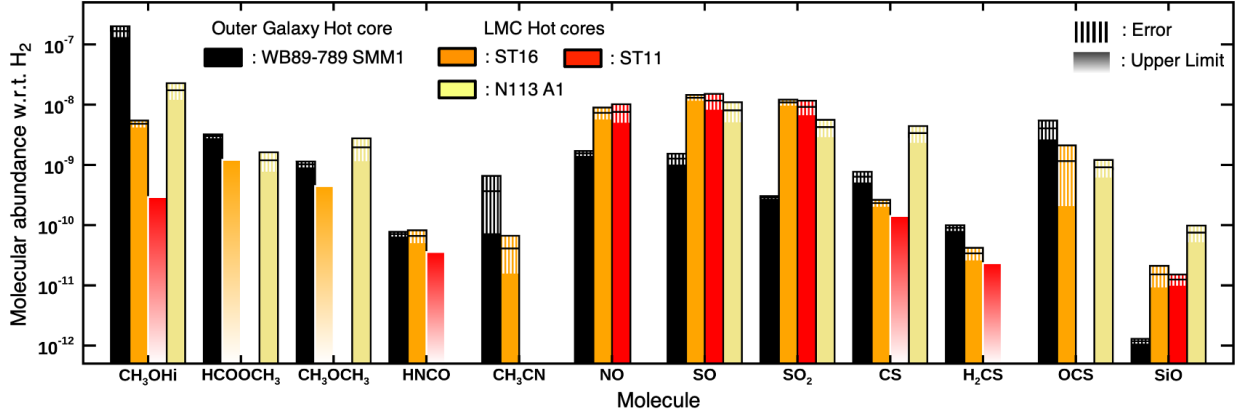


Figure 12. Comparison of molecular abundances between an outer Galactic hot core, WB89-789 SMM1 (black), and three LMC hot cores, ST11 (red), ST16 (orange), and N113 A1 (light yellow). Abundances of SMM1 are calculated for a 0.1 pc diameter region. The area with thin vertical lines indicate the error bar. The bar with a color gradient indicate an upper limit. The absence of bars indicate the lack of available data. See Section 4.4 for details.

it is not straightforward to attribute the low abundance of SO₂ (and perhaps SO) to the low elemental abundance ratio of sulfur in the outer Galaxy. Hot core chemistry models suggest that SO₂ is mainly produced in high-temperature gas-phase reactions in warm gas, using H₂S sublimated from ice mantles (Charnley 1997; Nomura & Millar 2004). This also applies to the SO₂ formation in low-metallicity sources as shown in astrochemical simulations for LMC hot cores (Shimonishi et al. 2020). We speculate that the different behavior of SO₂ in outer Galaxy and LMC hot cores may be related to differences in the evolutionary stage of hot cores. A different luminosity of host protostars may also contribute to the different sulfur chemistry; i.e., $\sim 8 \times 10^3$ L_⊙ for WB89-789-SMM1, while several $\times 10^5$ L_⊙ for LMC hot cores. A different cosmic-ray ionization rate between the outer Galaxy and the LMC may also affect the chemical evolution, although the rate is not known for the outer Galaxy.

Among nitrogen-bearing molecules, NO shows interesting behavior in LMC hot cores. After corrected for the metallicity, NO is overabundant in LMC hot cores compared with Galactic counterparts despite the low elemental abundance of nitrogen in the LMC (Shimonishi et al. 2020). Only NO shows such behavior among the nitrogen-bearing molecules observed in LMC hot cores. In WB89-789 SMM1, however, such an overabundance of NO is not observed. The NO abundance of SMM1 is 1.6×10^{-9} for a 0.1 pc region data. This is a factor of five lower than a typical NO abundance in Galactic high-mass hot cores (8×10^{-9} , Ziurys et al. 1991), which is consistent with a factor of four lower metallicity in WB89-789. The present high-spatial resolution data have revealed that NO does not mainly arise from a hot core region, as shown in Figure 4. It has an intensity peak at the south part of the hot core, where low-excitation lines of SO and SO₂ also have a secondary peak (Section 4.2). Thus, shock chemistry

or photochemistry, rather than high-temperature chemistry, would contribute to the production of NO in low-metallicity protostellar cores. In that case, a lower luminosity of SMM1 than those of LMC hot cores may contribute to the different behavior of NO.

For other nitrogen-bearing molecules, HNCO and CH₃CN, a clear difference is not identified between outer Galactic and LMC hot cores, although the number of data points is limited and the abundance uncertainty is large. The reason of the unusually low abundance of SiO in SMM1 is unknown. It may be related to different shock conditions or grain compositions, because dust sputtering by shock is mainly responsible for the production of SiO gas.

Formation of COMs is one of the important standpoints for low-metallicity hot core chemistry. It is reported that CH₃OH show a large abundance variation in LMC hot cores (Shimonishi et al. 2020). There are organic-poor hot cores such as ST11 and ST16, while N113 A1 and B3 are organic-rich. The CH₃OH abundance of WB89-789 SMM1 is higher than those of any known LMC hot cores. The abundances of HCOOCH₃ and CH₃OCH₃ in SMM1 are comparable with those of an organic-rich LMC hot core, N113 A1. The detection of many other COMs in SMM1 suggests the source have experienced rich organic chemistry despite its low-metallicity nature.

Astrochemical simulations for LMC hot cores suggest that dust temperature at the initial ice-forming stage have a major effect on the abundance of CH₃OH gas in the subsequent hot core stage (Acharyya & Herbst 2018; Shimonishi et al. 2020). Simulations of grain surface chemistry dedicated to the LMC environment also suggest that dust temperature is one of the key parameters for the formation of CH₃OH in dense cores (Acharyya & Herbst 2015; Pauly & Garrod 2018). This is because (i) CH₃OH is mainly formed by the

grain surface reaction, and (ii) the hydrogenation reaction of CO, which is a dominant pathway for the CH₃OH formation, is sensitive to the dust temperature due to the high volatility of atomic hydrogen. For this reason, it is inferred that organic-rich hot cores had experienced a cold stage ($\lesssim 10$ K) that is sufficient for the CH₃OH formation before the hot core stage, while organic-poor ones might have missed such a condition for some reason. Alternatively, the slight difference in the hot core's evolutionary stage may contribute to the CH₃OH abundance variation, because the high-temperature gas-phase chemistry is rapid and it can decrease CH₃OH gas at a late stage (e.g., Nomura & Millar 2004; Garrod & Herbst 2006; Vasyunin & Herbst 2013; Balucani et al. 2015).

Low-metallicity hot core chemistry simulations in Shimonishi et al. (2020) argue that the maximum achievable abundances of CH₃OH gas in a hot core stage significantly decrease as the visual extinction of the initial ice-forming stage decreases. On the other hand, the simulations show that the CH₃OH gas abundance is simply metallicity-scaled if the initial ice-forming stage is sufficiently shielded. In a well-shielded initial condition, the grain surface is cold enough to trigger the CO hydrogenation, and the resultant CH₃OH abundance is roughly regulated by the elemental abundances. The observed metallicity-scaled chemistry of COMs in WB89-789 SMM1 implies that the source had experienced such an initial condition before the hot core stage.

Deuterium chemistry is widely used in interpreting chemical and physical history of interstellar molecules (e.g., Caselli & Ceccarelli 2012; Ceccarelli et al. 2014). The measured CH₂DOH/CH₃OH ratio in WB89-789 SMM1 is $1.1 \pm 0.2\%$, which is comparable to the higher end of those ratios observed in high-mass protostars and the lower end of those in low-mass protostars (e.g., see Fig.2 in Drozdovskaya et al. 2021). The ratio is orders of magnitude higher than the deuterium-to-hydrogen ratio in the solar neighborhood (2×10^{-5} ; Linsky et al. 2006; Prodanović et al. 2010) and that in the big-bang nucleosynthesis (3×10^{-5} ; Burles 2002, references therein). This suggests that the efficient deuterium fractionation occurred upon the formation of CH₃OH in SMM1. The D₂CO/HDCO ratio is $45 \pm 10\%$, which is comparable to those observed in low-mass and high-mass protostars (e.g., Zahorecz et al. 2021). This would suggest that physical conditions for deuterium fractionation could be similar between WB89-789 SMM1 and inner Galactic protostars. Note that higher spatial resolution observations and detailed multiline analyses would affect the measured abundance of deuterated species as reported in Persson et al. (2018) for the case of a nearby low-mass protostar. The H₂CO column density derived in this work may be a lower limit because the line is often optically thick, thus we do not discuss the abundance ratio relative to H₂CO.

It is known that the deuterium fractionation efficiently proceeds at low temperature (e.g., Roberts et al. 2003; Caselli & Ceccarelli 2012; Taquet et al. 2014; Furuya et al. 2016). This is because the key reaction for the trigger of deuterium fractionation, $H_3^+ + HD \rightarrow H_2D^+ + H_2 + 232$ K, is exothermic and its backward reaction cannot efficiently proceed below 20 K. In addition, gaseous neutral species such as CO and O efficiently destruct H₂D⁺, thus their depletion at low temperature further enhances the deuterium fractionation (e.g., Caselli & Ceccarelli 2012). A sign of high deuterium fractionation observed in WB89-789 SMM1 suggests that the source had experienced such a cold environment during its formation. This picture is consistent with the implication obtained from the metallicity-scaled chemistry of COMs, which also suggests the occurrence of a cold and well-shielded initial condition as discussed above.

Although the low metallicity is common between the outer Galaxy and the LMC, their star-forming environments would be different; the LMC has more harsh environments as inferred from active massive star formation over the whole galaxy, while that for the outer Galaxy might be quiescent due to its low star formation activity. Those environmental differences need to be taken into account for further understanding of the chemical evolution of star-forming regions at low metallicity. Future extensive survey of protostellar objects towards the outer Galaxy is thus vitally important for further discussion. Astrochemical simulations dedicated to the environment of the outer Galaxy, and the application to lower-mass protostars, are also important.

4.5. Another embedded protostar traced by high-velocity SiO gas

We have also detected a compact source associated with high-velocity SiO gas at the east side of WB89-789 SMM1. Hereafter, we refer to this source as WB89-789-SMM2. According to the SiO emission, the source is located at RA = $06^{\text{h}}17^{\text{m}}24.246$ and Dec = $14^{\circ}54'43.25$ (ICRS), which is $2.7'$ (0.14 pc) away from SMM2. Figure 13(a) shows the SiO(6-5) spectrum extracted from a $0.6''$ diameter region centered at the above position. The SiO line is largely shifted to the blue and red sides relative to the systemic velocity in a symmetric fashion. The peaks of the shifted emission are located at $V_{\text{sys}} \pm 25 \text{ km s}^{-1}$.

Figure 13(b) shows a velocity map and integrated intensity distribution of SiO(6-5). In the figure, to focus on SiO in WB89-789-SMM2, the intensity is integrated over much wider velocity range (0 – 60 km s^{-1}) compared with that adopted in Figure 4 (31 – 38 km s^{-1}). The velocity map clearly indicates that the velocity structure of SiO in SMM2 is spatially symmetric to the SiO center. At this position, a local peak is seen in $1200 \mu\text{m}$ continuum as shown in the figure, suggesting the presence of an embedded source. SMM2

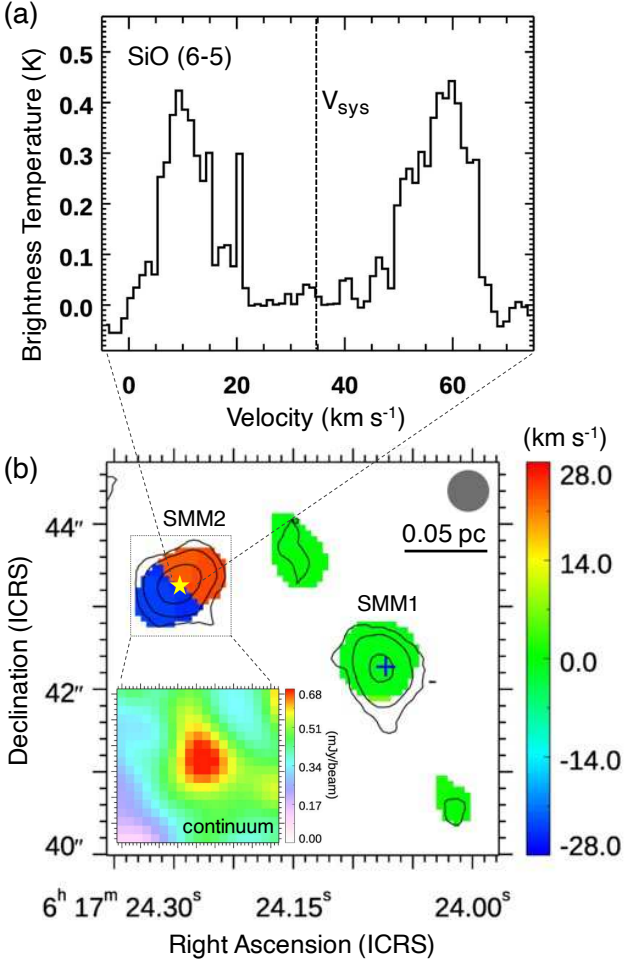


Figure 13. (a) SiO(6-5) spectrum of WB89-789-SMM2. The dotted line indicates a systemic velocity of 34.5 km s^{-1} . High-velocity ($V_{\text{sys}} \pm 25 \text{ km s}^{-1}$) SiO components are seen at the blue-/red-shifted sides of the systemic velocity. (b) Velocity map (moment 1) of the SiO(6-5) line. The color scale indicates the offset velocity relative to the systemic velocity. Low signal-to-noise ratio regions ($S/N < 5$) are masked. Gray contours represent the intensity distribution of SiO(6-5) integrated from 0 to 60 km s^{-1} , and the contour levels are 1.5σ , 4σ , and 12σ of the rms level. The yellow star indicates the SiO center of SMM2, while the blue cross indicates the hot core position (SMM1). The subset panel shows the $1200 \mu\text{m}$ continuum image for a $1.2' \times 1.2'$ region centered at SMM2. See Section 4.5 for details.

does not show any emission lines of COMs, and no alternative molecular lines are identified at the frequencies of doppler-shifted SiO emission. Also taking into account the clear spectral and spatial symmetry, the observed lines must be attributed to high-velocity SiO gas.

The spectral characteristics of the observed high-velocity SiO resemble those of extremely high velocity (EHV) outflows observed in Class 0 protostars (Bachiller et al. 1991; Tafalla et al. 2010, 2015; Tychoniec et al. 2019). The EHV

flows are known to appear as a discrete high-velocity ($V \gtrsim 30 \text{ km s}^{-1}$) peak, and observed in the youngest stage of star formation (Bachiller 1996; Matsushita et al. 2019, references therein). The EHV flows extends up to several thousands au from the central protostar in SiO, and usually have collimated bipolar structures (e.g., Bachiller et al. 1991; Hirano et al. 2010; Tychoniec et al. 2019; Matsushita et al. 2019). The beam size of the present data is about 5000 au, thus such structures will not be fully spatially resolved. Actually, a symmetric spatial distribution of blue-/red-shifted SiO is only marginally resolved into two beam size regions (Fig. 13(b)). A spatial extent of SiO emission is about $1''$ (0.052 pc). Assuming an outflow velocity of 25 km s^{-1} , we estimate a dynamical timescale of EHV flows to be at least 2000 years. This is roughly consistent with dynamical timescales of other EHV sources, which range from a few hundred to a few thousand years (Bachiller 1996, references therein).

A $1200 \mu\text{m}$ continuum flux in a $0''.6$ diameter region centered at SMM2 is $0.60 \pm 0.05 \text{ mJy/beam}$. Assuming $T_d = 20 \text{ K}$, we obtain $N_{\text{H}_2} = 3.2 \times 10^{23} \text{ cm}^{-2}$. This is equivalent to a gas number density of $n_{\text{H}_2} = 4.9 \times 10^6 \text{ cm}^{-3}$. If we assume a higher T_d , i.e. 40 K , then the derived column density is 2.5 times lower than the 20 K case. In either case, the continuum data suggests the presence of high-density gas at this position.

A column density and fractional abundance of SiO gas at the above position is estimated to be $N(\text{SiO}) \sim 2 \times 10^{13} \text{ cm}^{-2}$ and $N(\text{SiO})/N_{\text{H}_2} \sim 6 \times 10^{-11}$, where we assume optically thin emission in the LTE and the gas/dust temperature of 20 K . The fractional abundance will be two times higher if we assume the gas/dust temperature of 10 K or 40 K . The SiO abundance in SMM2 is at least 30 times higher than that observed in SMM1. The observed enhancement of SiO in SMM2 would be related to shock chemistry triggered by EHV outflows.

Previous single-dish observations of CO detected extended ($\sim 20''$) molecular outflows in the WB89-789 region (Brand & Wouterloot 1994, 2007). The center of the outflow gas coincides with the position of the IRAS source (IRAS 06145+1455; $06^{\text{h}} 17^{\text{m}} 24.2^{\text{s}}$, $14^{\circ} 54' 42''$, J2000). This position is consistent with those of SMM1 or SMM2, given the large beam size of CO(3-2) observations ($14''$) in Brand & Wouterloot (2007). The observed CO outflow gas has an extended blue-shifted component ($20 < V_{\text{LSR}} < 31 \text{ km s}^{-1}$) towards the south-east direction from the center, while a red-shifted component ($37 < V_{\text{LSR}} < 55 \text{ km s}^{-1}$) is extended towards the north-west direction (see Figure 9 in Brand & Wouterloot 2007). This outflow direction coincides with that of the high-velocity SiO outflows observed in this work. The SiO outflows from SMM2 may have a common origin with the large-scale CO outflows.

In summary, it is likely that a compact, high-density, and embedded object is located at the position of WB89-789-SMM2. Presumably, a protostar associated with SMM2 is driving the observed high-velocity SiO gas flows. Its short dynamical timescale and similarity with EHV flows suggest that the object is at the youngest stage of star formation (Class 0/I). Non-detection of warm gas emission also supports its young nature. We note that the detailed structure of high-velocity SiO gas is not fully spatially resolved, and CO lines, which often trace high-velocity outflows, are not covered in the present data. Future high-spatial resolution observations of CO and other outflow tracers are key to further clarify the nature of WB89-789-SMM2.

5. SUMMARY

The extreme outer Galaxy is an excellent laboratory to study star formation and interstellar medium in a Galactic low-metallicity environment. The following conclusions are obtained in this work.

1. A hot molecular core is for the first time detected in the extreme outer Galaxy (WB89-789-SMM1), based on submillimeter observations with ALMA towards the WB89-789 star-forming region located at the galactocentric distance of 19 kpc.
2. A variety of carbon-, oxygen-, nitrogen-, sulfur-, and silicon-bearing species, including complex organic molecules containing up to nine atoms and larger than CH₃OH, are detected towards a warm (>100 K) and compact (< 0.03 pc) region associated with a protostar ($\sim 8 \times 10^3 L_\odot$). The results suggest that a great molecular complexity exists even in a lower metallicity environment of the extreme outer Galaxy.
3. For deuterated species, we have detected HDO, HDCO, D₂CO, and CH₂DOH. HDO and CH₂DOH arise from a compact and high-temperature ($T_{rot} = 155\text{--}220$) region, while HDCO and D₂CO are in lower temperature ($T_{rot} \sim 40$ K) and slightly extended. The measured ratios of CH₂DOH/CH₃OH and D₂CO/HDCO are $1.1 \pm 0.2\%$ and $45 \pm 10\%$, respectively.
4. Fractional abundances of CH₃OH and other COMs relative to H₂ generally scale with the metallicity of WB89-789, which is a factor of four lower than the solar value.

5. A comparison of fractional abundances of COMs relative to the CH₃OH column density between the outer Galactic hot core and a Galactic intermediate-mass hot core show a remarkable similarity. The results suggest the metallicity-scaled chemistry for the formation of COMs in this source. CH₃OH is an important parental molecule for the COMs formation even in a lower metallicity environment.
6. On the other hand, the molecular abundances of the present hot core do not resemble those of LMC hot cores. We speculate that different luminosities or star-forming environments between outer Galactic and LMC hot cores may contribute to this.
7. According to astrochemical simulations of low-metallicity hot cores, the observed metallicity-scaled chemistry of COMs in WB89-789-SMM1 implies that the source had experienced well-shielded and cold ice-forming stage before the hot core stage.
8. We have also detected another compact source (WB89-789-SMM2) associated with high-velocity SiO gas ($V_{sys} \pm 25 \text{ km s}^{-1}$) in the same region. The characteristics of the source resemble those of EHV outflows observed in Class 0 protostars. Physical properties and dynamical timescale of this outflow source are discussed.

This paper makes use of the following ALMA data: ADS/JAO.ALMA#2017.1.01002.S and 2018.1.00627.S. ALMA is a partnership of ESO (representing its member states), NSF (USA) and NINS (Japan), together with NRC (Canada), MOST and ASIAA (Taiwan), and KASI (Republic of Korea), in cooperation with the Republic of Chile. The Joint ALMA Observatory is operated by ESO, AUI/NRAO and NAOJ. This work has made extensive use of the Cologne Database for Molecular Spectroscopy and the molecular database of the Jet Propulsion Laboratory. This work makes use of data products from the Two Micron All Sky Survey, which is a joint project of the University of Massachusetts and the Infrared Processing and Analysis Center/California Institute of Technology, funded by the National Aeronautics and Space Administration and the National Science Foundation. This work was supported by JSPS KAKENHI Grant Number 19H05067, 21H00037, and 21H01145. Finally, we would like to thank an anonymous referee for insightful comments, which substantially improved this paper.

Software: CASA (McMullin et al. 2007))

REFERENCES

Acharyya, K., & Herbst, E. 2015, ApJ, 812, 142

—. 2018, ApJ, 859, 51

- Anderson, L. D., Armentrout, W. P., Johnstone, B. M., et al. 2015, *ApJS*, 221, 26
- Anderson, L. D., Armentrout, W. P., Luisi, M., et al. 2018, *ApJS*, 234, 33
- Arellano-Córdova, K. Z., Esteban, C., García-Rojas, J., & Méndez-Delgado, J. E. 2020, *MNRAS*, 496, 1051
- . 2021, *MNRAS*, 502, 225
- Bachiller, R. 1996, *ARA&A*, 34, 111
- Bachiller, R., Martin-Pintado, J., & Fuente, A. 1991, *A&A*, 243, L21
- Balucani, N., Ceccarelli, C., & Taquet, V. 2015, *MNRAS*, 449, L16
- Beuther, H., Schilke, P., Sridharan, T. K., et al. 2002, *A&A*, 383, 892
- Boogert, A. C. A., Huard, T. L., Cook, A. M., et al. 2011, *ApJ*, 729, 92
- Bragança, G. A., Daflon, S., Lanz, T., et al. 2019, *A&A*, 625, A120
- Brand, J., & Wouterloot, J. G. A. 1994, *A&AS*, 103, 503
- . 2007, *A&A*, 464, 909
- Burles, S. 2002, *Planet. Space Sci.*, 50, 1245
- Caselli, P., & Ceccarelli, C. 2012, *A&A Rev*, 20, 56
- Ceccarelli, C., Caselli, P., Bockelée-Morvan, D., et al. 2014, in *Protostars and Planets VI*, ed. H. Beuther, R. S. Klessen, C. P. Dullemond, & T. Henning, 859
- Charnley, S. B. 1997, *ApJ*, 481, 396
- Chin, Y.-N., Henkel, C., Whiteoak, J. B., Langer, N., & Churchwell, E. B. 1996, *A&A*, 305, 960
- Choudhury, S., Subramaniam, A., & Cole, A. A. 2016, *MNRAS*, 455, 1855
- Cox, A. N. 2000, *Allen's astrophysical quantities* (Springer)
- Draine, B. T. 2003, *ARA&A*, 41, 241
- Drozdovskaya, M. N., van Dishoeck, E. F., Rubin, M., Jørgensen, J. K., & Altweig, K. 2019, *MNRAS*, 490, 50
- Drozdovskaya, M. N., Schroeder I, I. R. H. G., Rubin, M., et al. 2021, *MNRAS*, 500, 4901
- Dufour, R. J., Shields, G. A., & Talbot, Jr., R. J. 1982, *ApJ*, 252, 461
- Ferguson, A. M. N., Gallagher, J. S., & Wyse, R. F. G. 1998, *AJ*, 116, 673
- Fernández-Martín, A., Pérez-Montero, E., Vílchez, J. M., & Mampaso, A. 2017, *A&A*, 597, A84
- Fuente, A., Martin-Pintado, J., Cernicharo, J., & Bachiller, R. 1993, *A&A*, 276, 473
- Fuente, A., Cernicharo, J., Caselli, P., et al. 2014, *A&A*, 568, A65
- Furuya, K., van Dishoeck, E. F., & Aikawa, Y. 2016, *A&A*, 586, A127
- Garrod, R. T., & Herbst, E. 2006, *A&A*, 457, 927
- Goldsmith, P. F., & Langer, W. D. 1999, *ApJ*, 517, 209
- Herbst, E., & van Dishoeck, E. F. 2009, *ARA&A*, 47, 427
- Hirano, N., Ho, P. P. T., Liu, S.-Y., et al. 2010, *ApJ*, 717, 58
- Hudson, R. L., & Moore, M. H. 1999, *Icarus*, 140, 451
- Humire, P. K., Thiel, V., Henkel, C., et al. 2020, *A&A*, 642, A222
- Izumi, N., Kobayashi, N., Yasui, C., Saito, M., & Hamano, S. 2017, *AJ*, 154, 163
- Jansen, D. J., Spaans, M., Hogerheijde, M. R., & van Dishoeck, E. F. 1995, *A&A*, 303, 541
- Kobayashi, N., Yasui, C., Tokunaga, A. T., & Saito, M. 2008, *ApJ*, 683, 178
- Kurtz, S., Cesaroni, R., Churchwell, E., Hofner, P., & Walmsley, C. M. 2000, *Protostars and Planets IV*, 299
- Linsky, J. L., Draine, B. T., Moos, H. W., et al. 2006, *ApJ*, 647, 1106
- Matsushita, Y., Takahashi, S., Machida, M. N., & Tomisaka, K. 2019, *ApJ*, 871, 221
- Maud, L. T., Moore, T. J. T., Lumsden, S. L., et al. 2015, *MNRAS*, 453, 645
- McMullin, J. P., Waters, B., Schiebel, D., Young, W., & Golap, K. 2007, in *Astronomical Society of the Pacific Conference Series*, Vol. 376, *Astronomical Data Analysis Software and Systems XVI*, ed. R. A. Shaw, F. Hill, & D. J. Bell, 127
- Müller, H. S. P., Schlöder, F., Stutzki, J., & Winnewisser, G. 2005, *Journal of Molecular Structure*, 742, 215
- Müller, H. S. P., Thorwirth, S., Roth, D. A., & Winnewisser, G. 2001, *A&A*, 370, L49
- Nakanishi, H., & Sofue, Y. 2016, *PASJ*, 68, 5
- Nomura, H., & Millar, T. J. 2004, *A&A*, 414, 409
- Ossenkopf, V., & Henning, T. 1994, *A&A*, 291, 943
- Pauly, T., & Garrod, R. T. 2018, *ApJ*, 854, 13
- Persson, M. V., Jørgensen, J. K., Müller, H. S. P., et al. 2018, *A&A*, 610, A54
- Pety, J., Guzmán, V. V., Orkisz, J. H., et al. 2017, *A&A*, 599, A98
- Pickett, H. M., Poynter, R. L., Cohen, E. A., et al. 1998, *JQSRT*, 60, 883
- Prodanović, T., Steigman, G., & Fields, B. D. 2010, *MNRAS*, 406, 1108
- Roberts, H., Herbst, E., & Millar, T. J. 2003, *ApJL*, 591, L41
- Robitaille, T. P., Whitney, B. A., Indebetouw, R., & Wood, K. 2007, *ApJS*, 169, 328
- Rodríguez-Franco, A., Martin-Pintado, J., & Fuente, A. 1998, *A&A*, 329, 1097
- Russell, S. C., & Dopita, M. A. 1992, *ApJ*, 384, 508
- Schutte, W. A., & Greenberg, J. M. 1997, *A&A*, 317, L43
- Sewiło, M., Indebetouw, R., Charnley, S. B., et al. 2018, *ApJL*, 853, L19
- Shimonishi, T., Dartois, E., Onaka, T., & Boulanger, F. 2016a, *A&A*, 585, A107
- Shimonishi, T., Das, A., Sakai, N., et al. 2020, *ApJ*, 891, 164
- Shimonishi, T., Onaka, T., Kawamura, A., & Aikawa, Y. 2016b, *ApJ*, 827, 72
- Skrutskie, M. F., Cutri, R. M., Stiening, R., et al. 2006, *AJ*, 131, 1163

- Sternberg, A., & Dalgarno, A. 1995, ApJS, 99, 565
- Sutton, E. C., Peng, R., Danchi, W. C., et al. 1995, ApJS, 97, 455
- Tafalla, M., Bachiller, R., Lefloch, B., et al. 2015, A&A, 573, L2
- Tafalla, M., Santiago-García, J., Hacar, A., & Bachiller, R. 2010, A&A, 522, A91
- Taquet, V., Charnley, S. B., & Sipilä, O. 2014, ApJ, 791, 1
- Taquet, V., Wirström, E. S., & Charnley, S. B. 2016, ApJ, 821, 46
- Tychoniec, Ł., Hull, C. L. H., Kristensen, L. E., et al. 2019, A&A, 632, A101
- van der Tak, F. F. S., Black, J. H., Schöier, F. L., Jansen, D. J., & van Dishoeck, E. F. 2007, A&A, 468, 627
- van Dishoeck, E. F., & Blake, G. A. 1998, ARA&A, 36, 317
- Vasyunin, A. I., & Herbst, E. 2013, ApJ, 769, 34
- Watanabe, N., Mourí, O., Nagaoka, A., et al. 2007, ApJ, 668, 1001
- Wenger, T. V., Balser, D. S., Anderson, L. D., & Bania, T. M. 2019, ApJ, 887, 114
- Wenger, T. V., Dawson, J. R., Dickey, J. M., et al. 2021, ApJS, 254, 36
- Westerlund, B. E. 1990, A&A Rv, 2, 29
- Whittet, D. C. B., Gerakines, P. A., Hough, J. H., & Shenoy, S. S. 2001, ApJ, 547, 872
- Wilson, T. L., & Rood, R. 1994, ARA&A, 32, 191
- Wirström, E. S., Geppert, W. D., Hjalmarson, Å., et al. 2011, A&A, 533, A24
- Wouterloot, J. G. A., Brand, J., & Fiegle, K. 1993, A&AS, 98, 589
- Wright, E. L., Eisenhardt, P. R. M., Mainzer, A. K., et al. 2010, AJ, 140, 1868
- Yamamura, I., Makiuti, S., Ikeda, N., et al. 2010, VizieR Online Data Catalog, II/298
- Yasui, C., Kobayashi, N., Tokunaga, A. T., Terada, H., & Saito, M. 2006, ApJ, 649, 753
- Zahorecz, S., Jimenez-Serra, I., Testi, L., et al. 2021, A&A, 653, A45
- Zinnecker, H., & Yorke, H. W. 2007, ARA&A, 45, 481
- Ziurys, L. M., McGonagle, D., Minh, Y., & Irvine, W. M. 1991, ApJ, 373, 535

APPENDIX

A. MEASURED LINE PARAMETERS

Tables A1–A9 summarize measured line parameters (see Section 3.1 for details). The tabulated uncertainties and upper limits are of 2σ level and do not include systematic errors due to continuum subtraction. Upper limits are estimated assuming $\Delta V = 4$ km s $^{-1}$.

Table A1. Line Parameters for HDO, H 13 CO $^+$, HC 18 O $^+$, CCH, c-C $_3$ H $_2$, H $_2$ CO, HDCO, D $_2$ CO

Molecule	Transition	E_u	Frequency	T_{br}	ΔV	$\int T_{br} dV$	V_{LSR}	RMS	Note
		(K)	(GHz)	(K)	(km/s)	(K km/s)	(km/s)	(K)	
HDO	2 _{1,1} –2 _{1,2}	95	241.56155	0.99 ± 0.03	4.8	5.05 ± 0.29	34.6	0.04	...
HDO	7 _{3,4} –6 _{4,3}	837	241.97357	0.28 ± 0.02	2.1	0.63 ± 0.12	34.1	0.04	...
H 13 CO $^+$	3–2	25	260.25534	5.85 ± 0.02	2.3	14.23 ± 0.13	34.1	0.03	...
HC 18 O $^+$	4–3	41	340.63069	0.64 ± 0.05	1.9	1.29 ± 0.20	34.1	0.07	...
CCH	N = 4–3, J = $\frac{9}{2}$ – $\frac{7}{2}$, F = 5–4	42	349.33771	4.39 ± 0.04	2.6	12.32 ± 0.24	33.7	0.08	(1)
CCH	N = 4–3, J = $\frac{7}{2}$ – $\frac{5}{2}$, F = 4–3	42	349.39928	3.54 ± 0.04	2.8	10.49 ± 0.26	33.7	0.08	(1)
c-C $_3$ H $_2$	3 _{2,1} –2 _{1,2}	18	244.22215	0.23 ± 0.02	4.8	1.18 ± 0.27	33.6	0.04	...
c-C $_3$ H $_2$	5 _{3,2} –4 _{4,1}	45	260.47975	0.09 ± 0.02	1.6	0.15 ± 0.10	32.9	0.03	(2)
H $_2$ CO	5 _{1,5} –4 _{1,4}	62	351.76864	7.02 ± 0.05	3.7	27.32 ± 0.40	34.2	0.08	...
HDCO	4 _{2,3} –3 _{2,2}	63	257.74870	0.94 ± 0.02	2.8	2.80 ± 0.14	34.3	0.03	...
HDCO	4 _{2,2} –3 _{2,1}	63	259.03491	0.97 ± 0.02	2.9	3.00 ± 0.18	34.3	0.03	...
D $_2$ CO	4 _{1,3} –3 _{1,2}	35	245.53275	0.64 ± 0.03	2.3	1.54 ± 0.15	34.2	0.04	...
D $_2$ CO	6 _{2,5} –5 _{2,4}	80	349.63061	0.76 ± 0.04	2.4	1.92 ± 0.23	33.9	0.08	...

NOTE—(1) Blend of two hyperfine components. (2) Tentative detection.

Table A2. Line Parameters for N-bearing molecules

Molecule	Transition	E_u	Frequency	T_{br}	ΔV	$\int T_{br} dV$	V_{LSR}	RMS	Note
		(K)	(GHz)	(K)	(km/s)	(K km/s)	(km/s)	(K)	
H 13 CN	3–2	25	259.01180	3.25 ± 0.02	4.2	14.45 ± 0.19	34.3	0.03	...
HC 15 N	3–2	25	258.15700	1.95 ± 0.02	3.6	7.45 ± 0.19	34.3	0.03	...
CN	N = 3–2, J = $\frac{5}{2}$ – $\frac{5}{2}$, F = $\frac{3}{2}$ – $\frac{3}{2}$	33	339.44678	0.30 ± 0.04	2.6	0.82 ± 0.22	34.6	0.07	...
CN	N = 3–2, J = $\frac{5}{2}$ – $\frac{5}{2}$, F = $\frac{5}{2}$ – $\frac{5}{2}$	33	339.47590	0.39 ± 0.04	1.7	0.71 ± 0.17	34.0	0.07	...
CN	N = 3–2, J = $\frac{5}{2}$ – $\frac{5}{2}$, F = $\frac{7}{2}$ – $\frac{7}{2}$	33	339.51664	0.73 ± 0.04	1.8	1.38 ± 0.18	34.1	0.07	...
CN	N = 3–2, J = $\frac{5}{2}$ – $\frac{5}{2}$, F = $\frac{5}{2}$ – $\frac{5}{2}$	33	340.00813	0.95 ± 0.04	2.1	2.16 ± 0.20	33.9	0.07	...
CN	N = 3–2, J = $\frac{5}{2}$ – $\frac{3}{2}$, F = $\frac{3}{2}$ – $\frac{3}{2}$	33	340.01963	0.93 ± 0.04	1.8	1.81 ± 0.17	34.1	0.07	...
CN	N = 3–2, J = $\frac{5}{2}$ – $\frac{3}{2}$, F = $\frac{7}{2}$ – $\frac{5}{2}$	33	340.03155	3.08 ± 0.04	2.7	8.71 ± 0.25	33.8	0.07	...
CN	N = 3–2, J = $\frac{5}{2}$ – $\frac{3}{2}$, F = $\frac{5}{2}$ – $\frac{3}{2}$	33	340.03541	3.04 ± 0.04	2.1	6.87 ± 0.26	33.7	0.07	(1)
CN	N = 3–2, J = $\frac{7}{2}$ – $\frac{5}{2}$, F = $\frac{9}{2}$ – $\frac{7}{2}$	33	340.24777	4.38 ± 0.03	2.4	11.32 ± 0.22	33.4	0.07	(1)
CN	N = 3–2, J = $\frac{7}{2}$ – $\frac{5}{2}$, F = $\frac{5}{2}$ – $\frac{5}{2}$	33	340.26177	0.91 ± 0.04	1.9	1.85 ± 0.18	34.1	0.07	...
CN	N = 3–2, J = $\frac{7}{2}$ – $\frac{5}{2}$, F = $\frac{7}{2}$ – $\frac{7}{2}$	33	340.26495	1.02 ± 0.04	2.0	2.12 ± 0.18	33.9	0.07	...
NO	J = $\frac{7}{2}$ – $\frac{5}{2}$, $\Omega = \frac{1}{2}$, F = $\frac{9}{2}$ – $\frac{7}{2}$ –	36	351.04352	0.29 ± 0.03	2.5	0.78 ± 0.22	33.7	0.08	...
NO	J = $\frac{7}{2}$ – $\frac{5}{2}$, $\Omega = \frac{1}{2}$, F = $\frac{7}{2}$ – $\frac{5}{2}$ –	36	351.05171	0.50 ± 0.04	2.1	1.10 ± 0.20	34.3	0.08	(2)
HNC O	11 _{4,7} –10 _{4,6}	720	241.49864	0.32 ± 0.08	4.8	1.20 ± 0.13	33.8	0.04	(2)

Table A2 *continued*

Table A2 (continued)

Molecule	Transition	E_u	Frequency	T_{br}	ΔV	$\int T_{br} dV$	V_{LSR}	RMS	Note
		(K)	(GHz)	(K)	(km/s)	(K km/s)	(km/s)	(K)	
HNCO	11 _{3,9} –10 _{3,8}	445	241.61930	0.51 ± 0.02	4.1	2.19 ± 0.25	33.6	0.04	(2)
HNCO	11 _{2,10} –10 _{2,9}	240	241.70385	<0.60	...	<2.6	...	0.04	(3)
HNCO	11 _{0,11} –10 _{0,10}	70	241.77403	0.93 ± 0.02	4.9	4.87 ± 0.26	34.6	0.04	...
HNCO	11 _{1,10} –10 _{1,9}	113	242.63970	0.79 ± 0.02	5.0	4.18 ± 0.27	34.7	0.04	...
HNCO	16 _{1,16} –15 _{1,15}	186	350.33306	0.69 ± 0.04	5.1	3.73 ± 0.44	34.5	0.08	...
HNCO	16 _{4,13} –15 _{4,12}	794	351.24085	<0.25	...	<1.1	...	0.08	(3)
HNCO	16 _{3,14} –15 _{3,13}	518	351.41680	0.33 ± 0.04	5.2	1.83 ± 0.45	34.4	0.08	(2)
HNCO	16 _{2,15} –15 _{2,14}	314	351.53780	0.43 ± 0.03	5.4	2.47 ± 0.49	34.1	0.08	...
HNCO	16 _{2,14} –15 _{2,13}	314	351.55157	0.46 ± 0.03	5.8	2.82 ± 0.53	35.2	0.08	...
HNCO	16 _{0,16} –15 _{0,15}	143	351.63326	0.72 ± 0.04	4.0	3.02 ± 0.41	34.6	0.08	...
HNCO	23 _{1,23} –24 _{0,24}	333	351.99487	0.33 ± 0.03	5.5	1.91 ± 0.47	35.9	0.08	...
CH ₃ CN	14 ₁₀ –13 ₁₀	806	257.03344	0.14 ± 0.02	2.4	0.36 ± 0.10	34.0	0.03	(2)
CH ₃ CN	14 ₉ –13 ₋₉	671	257.12704	<0.35	...	<1.5	...	0.03	(2) (4)
CH ₃ CN	14 ₈ –13 ₈	549	257.21088	0.24 ± 0.01	6.3	1.64 ± 0.27	34.9	0.03	(2)
CH ₃ CN	14 ₇ –13 ₇	442	257.28494	0.42 ± 0.02	4.9	2.20 ± 0.21	34.3	0.03	(2)
CH ₃ CN	14 ₆ –13 ₋₆	350	257.34918	0.90 ± 0.02	4.7	4.51 ± 0.20	34.4	0.03	(2)
CH ₃ CN	14 ₅ –13 ₅	271	257.40358	<1.00	...	<4.3	...	0.03	(2) (3)
CH ₃ CN	14 ₄ –13 ₄	207	257.44813	1.14 ± 0.02	4.3	5.22 ± 0.19	34.4	0.03	(2)
CH ₃ CN	14 ₃ –13 ₋₃	157	257.48279	1.55 ± 0.02	4.6	7.55 ± 0.20	34.5	0.03	(2)
CH ₃ CN	14 ₂ –13 ₂	121	257.50756	1.56 ± 0.02	4.4	7.34 ± 0.20	34.6	0.03	(2)
CH ₃ CN	14 ₁ –13 ₁	100	257.52243	1.63 ± 0.02	3.8	6.61 ± 0.18	34.7	0.03	(2)
CH ₃ CN	14 ₀ –13 ₀	93	257.52738	1.69 ± 0.02	4.3	7.79 ± 0.18	34.4	0.03	...
CH ₃ CN	19 ₆ –18 ₋₆	425	349.21231	0.73 ± 0.04	3.9	3.07 ± 0.35	34.2	0.08	(2)
CH ₃ CN	19 ₅ –18 ₅	346	349.28601	0.81 ± 0.04	3.4	2.97 ± 0.30	34.3	0.08	(2)
CH ₃ CN	19 ₄ –18 ₄	282	349.34634	0.92 ± 0.03	4.3	4.18 ± 0.40	34.4	0.08	(2)
CH ₃ CN	19 ₃ –18 ₋₃	232	349.39330	1.24 ± 0.03	4.1	5.38 ± 0.39	34.4	0.08	(5)
CH ₃ CN	19 ₂ –18 ₂	196	349.42685	1.04 ± 0.04	4.2	4.72 ± 0.37	34.6	0.08	(2)
CH ₃ CN	19 ₁ –18 ₁	175	349.44699	1.25 ± 0.03	4.1	5.42 ± 0.38	34.5	0.08	(5)
CH ₃ CN	19 ₀ –18 ₀	168	349.45370	1.23 ± 0.04	3.9	5.10 ± 0.38	34.2	0.08	...
¹³ CH ₃ CN	19 ₀ –18 ₀	163	339.36630	<0.11	...	<0.45	...	0.05	...
HC ₃ N	27–26	165	245.60632	1.55 ± 0.03	4.2	7.02 ± 0.25	34.3	0.04	...

NOTE— (1) Blend of three hyperfine components. (2) Blend of three two components. (3) Blend with CH₃OH. (4) Blend with HCOOCH₃. (5) Blend of four hyperfine components.

Table A3. Line Parameters for Si- and S-bearing molecules

Molecule	Transition	E_u	Frequency	T_{br}	ΔV	$\int T_{br} dV$	V_{LSR}	RMS	Note
		(K)	(GHz)	(K)	(km/s)	(K km/s)	(km/s)	(K)	
SiO	6–5	44	260.51801	0.64 ± 0.02	2.7	1.86 ± 0.13	34.1	0.03	...
SO	$N_J = 6_6$ – 5_5	56	258.25583	5.34 ± 0.02	3.6	20.20 ± 0.19	34.1	0.03	...
SO	$N_J = 3_3$ – 2_3	26	339.34146	0.49 ± 0.04	3.4	1.76 ± 0.34	34.0	0.07	...
SO	$N_J = 8_7$ – 7_6	81	340.71416	3.85 ± 0.04	3.9	15.81 ± 0.39	34.2	0.07	...
³⁴ SO	$N_J = 3_3$ – 2_3	25	337.89225	<0.15	...	<0.6	...	0.07	...
³⁴ SO	$N_J = 8_9$ – 7_8	77	339.85727	0.69 ± 0.04	4.4	3.26 ± 0.38	33.0	0.07	...
³³ SO	$N_J = 6_7$ – 5_6	47	259.28403	0.34 ± 0.07	6.8	0.81 ± 0.06	33.5	0.03	(1) (2)
CS	5–4	35	244.93556	14.57 ± 0.03	3.2	49.51 ± 0.20	33.9	0.04	...
C ³³ S	5–4	35	242.91361	1.31 ± 0.02	3.7	5.18 ± 0.21	34.2	0.04	...

Table A3 continued

Table A3 (continued)

Molecule	Transition	E_u	Frequency	T_{br}	ΔV	$\int T_{br} dV$	V_{LSR}	RMS	Note
		(K)	(GHz)	(K)	(km/s)	(K km/s)	(km/s)	(K)	
C ³³ S	7–6	65	340.05257	1.05 ± 0.04	3.9	4.35 ± 0.34	34.3	0.07	...
C ³⁴ S	7–6	65	337.39646	2.46 ± 0.04	3.3	8.65 ± 0.31	34.1	0.07	...
H ₂ CS	7 _{1,6} –6 _{1,5}	60	244.04850	2.91 ± 0.03	3.0	9.37 ± 0.19	34.2	0.04	...
H ₂ CS	10 _{1,10} –9 _{1,9}	102	338.08319	1.68 ± 0.04	3.9	7.04 ± 0.36	34.2	0.07	...
OCS	20–19	123	243.21804	1.82 ± 0.03	4.2	8.17 ± 0.24	34.3	0.04	...
OCS	28–27	237	340.44927	1.26 ± 0.04	4.0	5.40 ± 0.39	34.5	0.07	...
OCS	29–28	254	352.59957	1.05 ± 0.04	4.5	5.01 ± 0.40	34.3	0.08	...
O ¹³ CS	20–19	122	242.43543	0.20 ± 0.02	4.8	1.00 ± 0.32	34.9	0.04	...
SO ₂	5 _{2,4} –4 _{1,3}	24	241.61580	0.88 ± 0.02	5.1	4.79 ± 0.28	34.2	0.04	(3)
SO ₂	26 _{8,18} –27 _{7,21}	480	243.24543	<0.10	...	<0.4	...	0.04	...
SO ₂	14 _{0,14} –13 _{1,13}	94	244.25422	1.15 ± 0.02	6.3	7.67 ± 0.33	34.2	0.04	...
SO ₂	26 _{3,23} –25 _{4,22}	351	245.33923	0.41 ± 0.02	2.8	1.21 ± 0.15	34.5	0.04	...
SO ₂	10 _{3,7} –10 _{2,8}	73	245.56342	1.04 ± 0.02	5.3	5.86 ± 0.27	34.3	0.04	...
SO ₂	7 _{3,5} –7 _{2,6}	48	257.09997	0.96 ± 0.02	5.6	5.76 ± 0.24	34.2	0.03	(4)
SO ₂	32 _{4,28} –32 _{3,29}	531	258.38872	0.46 ± 0.02	4.1	2.01 ± 0.21	33.9	0.03	...
SO ₂	20 _{7,13} –21 _{6,16}	313	258.66697	0.32 ± 0.07	3.4	0.76 ± 0.08	33.1	0.03	(2)
SO ₂	9 _{3,7} –9 _{2,8}	63	258.94220	0.91 ± 0.02	5.4	5.26 ± 0.23	34.4	0.03	...
SO ₂	18 _{4,14} –18 _{3,15}	197	338.30599	0.65 ± 0.03	4.4	3.09 ± 0.37	34.0	0.07	...
SO ₂	20 _{1,19} –19 _{2,18}	199	338.61181	<0.90	...	<3.8	...	0.07	(5)
SO ₂	28 _{2,26} –28 _{1,27}	392	340.31641	0.48 ± 0.03	6.0	3.02 ± 0.50	34.5	0.07	...
SO ₂	5 _{3,3} –4 _{2,2}	36	351.25722	0.75 ± 0.04	5.9	4.73 ± 0.51	34.1	0.08	...
SO ₂	14 _{4,10} –14 _{3,11}	136	351.87387	0.70 ± 0.03	4.4	3.32 ± 0.38	34.0	0.08	...
³⁴ SO ₂	14 _{0,14} –13 _{1,13}	94	244.48152	0.34 ± 0.02	1.5	0.54 ± 0.09	33.6	0.04	...
¹³ CH ₃ SH	14 _{1,14} –13 _{1,13} A	131	350.00956	<0.15	...	<0.7	...	0.08	...

Note—(1) Blend of four hyperfine components. (2) The integrated intensity is calculated by directly integrating the spectrum.

(3) Partial blend with HNCO. (4) Blend with HCOOCH₃. (5) Blend with CH₃OH.**Table A4.** Line Parameters for CH₃OH, ¹³CH₃OH, and CH₂DOH

Molecule	Transition	E_u	Frequency	T_{br}	ΔV	$\int T_{br} dV$	V_{LSR}	RMS	Note
		(K)	(GHz)	(K)	(km/s)	(K km/s)	(km/s)	(K)	
CH ₃ OH	25 ₃ A [–] –25 ₂ A ⁺	804	241.58876	0.72 ± 0.02	4.5	3.49 ± 0.25	34.5	0.04	...
CH ₃ OH	5 ₀ E–4 ₀ E	48	241.70016	2.45 ± 0.03	4.0	10.57 ± 0.24	34.2	0.04	...
CH ₃ OH	5 _{–1} E–4 _{–1} E	40	241.76723	3.70 ± 0.03	3.2	12.53 ± 0.20	34.2	0.04	...
CH ₃ OH	5 ₀ A ⁺ –4 ₀ A ⁺	35	241.79135	4.15 ± 0.03	3.0	13.29 ± 0.19	34.1	0.04	...
CH ₃ OH	5 ₄ A [–] –4 ₄ A [–]	115	241.80652	1.46 ± 0.02	4.3	6.65 ± 0.23	34.7	0.04	(1)
CH ₃ OH	5 _{–4} E–4 _{–4} E	123	241.81325	1.33 ± 0.02	4.3	6.13 ± 0.23	34.7	0.04	...
CH ₃ OH	5 ₃ A ⁺ –4 ₃ A ⁺	85	241.83272	2.08 ± 0.02	4.2	9.35 ± 0.25	34.3	0.04	(2)
CH ₃ OH	5 ₂ A [–] –4 ₂ A [–]	73	241.84228	2.13 ± 0.02	5.0	11.37 ± 0.26	33.7	0.04	(1)
CH ₃ OH	5 _{–3} E–4 _{–3} E	98	241.85230	1.54 ± 0.02	4.4	7.13 ± 0.23	34.6	0.04	...
CH ₃ OH	5 ₁ E–4 ₁ E	56	241.87903	2.26 ± 0.03	3.9	9.26 ± 0.23	34.4	0.04	...
CH ₃ OH	5 ₂ A ⁺ –4 ₂ A ⁺	73	241.88767	1.82 ± 0.03	3.9	7.63 ± 0.23	34.5	0.04	...
CH ₃ OH	5 _{–2} E–4 _{–2} E	61	241.90415	2.94 ± 0.03	3.8	11.83 ± 0.21	34.0	0.04	(1)
CH ₃ OH	14 _{–1} E–13 _{–2} E	249	242.44608	1.28 ± 0.02	4.8	6.55 ± 0.25	34.6	0.04	(3)
CH ₃ OH	24 ₃ A [–] –24 ₂ A ⁺	746	242.49024	0.88 ± 0.02	4.6	4.30 ± 0.25	34.4	0.04	...
CH ₃ OH	5 ₁ A [–] –4 ₁ A [–]	50	243.91579	2.75 ± 0.02	3.6	10.69 ± 0.21	34.3	0.04	...
CH ₃ OH	22 ₃ A [–] –22 ₂ A ⁺	637	244.33037	1.06 ± 0.02	4.9	5.54 ± 0.27	34.6	0.04	...

Table A4 continued

Table A4 (continued)

Molecule	Transition	E_u	Frequency	T_{br}	ΔV	$\int T_{br} dV$	V_{LSR}	RMS	Note
		(K)	(GHz)	(K)	(km/s)	(K km/s)	(km/s)	(K)	
CH ₃ OH	9 ₁ E-8 ₀ E, $v_t = 1$	396	244.33798	1.08 ± 0.02	4.7	5.38 ± 0.25	34.6	0.04	...
CH ₃ OH	18 ₋₆ E-17 ₋₇ E, $v_t = 1$	889	245.09450	0.31 ± 0.02	4.1	1.35 ± 0.26	34.3	0.04	...
CH ₃ OH	21 ₃ A ⁻ -21 ₂ A ⁺	586	245.22302	1.22 ± 0.03	4.2	5.50 ± 0.24	34.4	0.04	...
CH ₃ OH	18 ₃ A ⁺ -18 ₂ A ⁻	447	257.40209	1.50 ± 0.02	6.0	9.52 ± 0.25	34.0	0.03	(4)
CH ₃ OH	19 ₃ A ⁺ -19 ₂ A ⁻	491	258.78025	1.22 ± 0.02	5.4	7.05 ± 0.23	34.1	0.03	...
CH ₃ OH	17 ₂ A ⁻ -16 ₁ A ⁻ , $v_t = 1$	653	259.27369	0.79 ± 0.02	4.2	3.54 ± 0.19	34.6	0.03	...
CH ₃ OH	24 ₁ E-24 ₀ E	717	259.58140	0.62 ± 0.02	4.4	2.89 ± 0.18	34.7	0.03	...
CH ₃ OH	20 ₋₈ E-21 ₋₇ E	808	260.06432	0.43 ± 0.02	3.8	1.75 ± 0.17	34.8	0.03	...
CH ₃ OH	20 ₃ A ⁺ -20 ₂ A ⁻	537	260.38146	1.22 ± 0.01	4.7	6.02 ± 0.25	34.3	0.03	...
CH ₃ OH	7 ₄ A ⁺ -6 ₄ A ⁺ , $v_t = 2$	679	337.27356	0.59 ± 0.04	4.3	2.68 ± 0.49	34.5	0.07	(1)
CH ₃ OH	7 ₋₂ E-6 ₋₂ E, $v_t = 2$	710	337.27918	0.54 ± 0.03	2.7	1.54 ± 0.48	34.8	0.07	...
CH ₃ OH	7 ₀ A ⁺ -6 ₀ A ⁺ , $v_t = 2$	573	337.28432	0.78 ± 0.03	5.3	4.36 ± 0.45	34.7	0.07	...
CH ₃ OH	7 ₁ A ⁺ -6 ₁ A ⁺ , $v_t = 1$	390	337.29748	0.97 ± 0.03	4.1	4.25 ± 0.39	35.3	0.07	(1)
CH ₃ OH	7 ₂ E-6 ₂ E, $v_t = 2$	651	337.30264	0.65 ± 0.03	4.2	2.94 ± 0.39	34.5	0.07	...
CH ₃ OH	7 ₋₁ E-6 ₋₁ E, $v_t = 2$	597	337.31236	0.57 ± 0.04	4.7	2.87 ± 0.41	34.3	0.07	...
CH ₃ OH	7 ₆ A ⁺ -6 ₆ A ⁺ , $v_t = 1$	533	337.46370	0.62 ± 0.04	5.5	3.62 ± 0.47	34.6	0.07	(1)
CH ₃ OH	10 ₀ E-9 ₋₉ E, $v_t = 1$	916	337.47259	0.40 ± 0.04	5.6	2.38 ± 0.47	33.8	0.07	...
CH ₃ OH	7 ₋₆ E-6 ₋₆ E, $v_t = 1$	558	337.49056	0.71 ± 0.04	4.3	3.23 ± 0.36	34.8	0.07	(5)
CH ₃ OH	7 ₃ E-6 ₃ E, $v_t = 1$	482	337.51914	0.80 ± 0.04	4.3	3.68 ± 0.38	34.9	0.07	...
CH ₃ OH	7 ₅ A ⁺ -6 ₅ A ⁺ , $v_t = 1$	485	337.54612	0.84 ± 0.04	4.7	4.19 ± 0.39	34.7	0.07	(1)
CH ₃ OH	7 ₄ E-6 ₄ E, $v_t = 1$	428	337.58168	<1.00	...	<4.3	...	0.07	(6)
CH ₃ OH	7 ₋₂ E-6 ₋₂ E, $v_t = 1$	429	337.60529	0.87 ± 0.03	3.8	3.51 ± 0.53	35.0	0.07	...
CH ₃ OH	7 ₋₃ E-6 ₋₃ E, $v_t = 1$	387	337.61066	1.01 ± 0.03	3.7	4.03 ± 0.32	34.6	0.07	(1)
CH ₃ OH	7 ₂ A ⁺ -6 ₂ A ⁺ , $v_t = 1$	363	337.62575	1.03 ± 0.04	3.4	3.71 ± 0.30	34.7	0.07	...
CH ₃ OH	7 ₂ A ⁻ -6 ₂ A ⁻ , $v_t = 1$	364	337.63575	1.00 ± 0.03	4.1	4.34 ± 0.39	34.6	0.07	...
CH ₃ OH	7 ₀ E-6 ₀ E, $v_t = 1$	365	337.64391	1.26 ± 0.03	7.9	10.58 ± 0.70	34.3	0.07	(2)
CH ₃ OH	7 ₃ A ⁺ -6 ₃ A ⁺ , $v_t = 1$	461	337.65520	0.98 ± 0.03	3.2	3.34 ± 0.33	34.4	0.07	(1)
CH ₃ OH	7 ₄ A ⁺ -6 ₄ A ⁺ , $v_t = 1$	546	337.68561	0.92 ± 0.04	4.0	3.89 ± 0.37	34.9	0.07	(2)
CH ₃ OH	7 ₋₁ E-6 ₋₁ E, $v_t = 1$	478	337.70757	0.83 ± 0.04	4.9	4.39 ± 0.44	34.5	0.07	...
CH ₃ OH	7 ₀ A ⁺ -6 ₀ A ⁺ , $v_t = 1$	488	337.74883	0.88 ± 0.04	4.2	3.96 ± 0.36	34.9	0.07	...
CH ₃ OH	20 ₋₆ E-21 ₋₅ E	676	337.83780	0.45 ± 0.04	3.5	1.69 ± 0.30	34.6	0.07	...
CH ₃ OH	7 ₁ A ⁺ -6 ₁ A ⁻ , $v_t = 2$	748	337.87755	0.51 ± 0.04	3.2	1.75 ± 0.28	34.6	0.07	...
CH ₃ OH	7 ₁ A ⁺ -6 ₁ A ⁻ , $v_t = 1$	390	337.96944	0.89 ± 0.04	4.4	4.13 ± 0.38	34.5	0.07	...
CH ₃ OH	7 ₀ E-6 ₀ E	78	338.12449	2.19 ± 0.04	3.4	7.84 ± 0.30	34.4	0.07	...
CH ₃ OH	7 ₋₁ E-6 ₋₁ E	71	338.34459	2.91 ± 0.04	3.5	10.81 ± 0.32	34.2	0.07	...
CH ₃ OH	7 ₆ E-6 ₆ E	244	338.40461	0.98 ± 0.04	3.8	4.00 ± 0.33	34.7	0.07	...
CH ₃ OH	7 ₀ A ⁺ -6 ₀ A ⁺	65	338.40870	3.41 ± 0.03	2.9	10.59 ± 0.28	34.1	0.07	...
CH ₃ OH	7 ₋₆ E-6 ₋₆ E	254	338.43097	0.88 ± 0.03	4.6	4.25 ± 0.38	34.6	0.07	...
CH ₃ OH	7 ₆ A ⁺ -6 ₆ A ⁺	259	338.44237	1.04 ± 0.04	4.3	4.79 ± 0.36	34.7	0.07	(1)
CH ₃ OH	7 ₋₅ E-6 ₋₅ E	189	338.45654	1.12 ± 0.03	4.7	5.62 ± 0.39	34.5	0.07	...
CH ₃ OH	7 ₅ E-6 ₅ E	201	338.47523	1.15 ± 0.03	4.1	5.02 ± 0.34	34.6	0.07	...
CH ₃ OH	7 ₅ A ⁺ -6 ₅ A ⁺	203	338.48632	1.22 ± 0.03	4.9	6.42 ± 0.42	34.5	0.07	(1)
CH ₃ OH	7 ₋₄ E-6 ₋₄ E	153	338.50407	1.31 ± 0.03	4.7	6.52 ± 0.41	34.8	0.07	...
CH ₃ OH	7 ₄ E-6 ₄ E	161	338.53026	1.30 ± 0.04	4.2	5.87 ± 0.35	34.4	0.07	...
CH ₃ OH	7 ₃ A ⁺ -6 ₃ A ⁺	115	338.54083	1.95 ± 0.04	5.5	11.45 ± 0.47	33.3	0.07	(1)
CH ₃ OH	7 ₋₃ E-6 ₋₃ E	128	338.55996	1.40 ± 0.04	4.5	6.74 ± 0.38	34.4	0.07	...
CH ₃ OH	7 ₃ E-6 ₃ E	113	338.58322	1.46 ± 0.04	4.3	6.70 ± 0.37	34.6	0.07	...
CH ₃ OH	7 ₁ E-6 ₁ E	86	338.61494	1.95 ± 0.04	4.4	9.18 ± 0.38	34.4	0.07	...
CH ₃ OH	7 ₂ A ⁺ -6 ₂ A ⁺	103	338.63980	1.60 ± 0.04	4.1	6.97 ± 0.34	34.5	0.07	...
CH ₃ OH	7 ₋₂ E-6 ₋₂ E	91	338.72290	2.52 ± 0.04	4.1	10.98 ± 0.35	34.9	0.07	(1)
CH ₃ OH	21 ₃ E-21 ₂ E, $v_t = 1$	951	339.42217	<0.18	...	<0.8	...	0.07	...
CH ₃ OH	2 ₂ A ⁺ -3 ₁ A ⁺	45	340.14114	1.08 ± 0.03	4.4	5.05 ± 0.38	35.2	0.07	...

Table A4 continued

Table A4 (continued)

Molecule	Transition	E_u	Frequency	T_{br}	ΔV	$\int T_{br} dV$	V_{LSR}	RMS	Note
		(K)	(GHz)	(K)	(km/s)	(K km/s)	(km/s)	(K)	
CH ₃ OH	16 ₆ A ⁻ –17 ₅ A ⁻	509	340.39366	0.90 ± 0.04	4.0	3.87 ± 0.34	34.7	0.07	...
CH ₃ OH	11 ₁ E–10 ₀ E, $\nu_t = 1$	444	340.68397	0.98 ± 0.03	5.1	5.29 ± 0.46	34.8	0.07	...
CH ₃ OH	15 ₃ E–16 ₄ E, $\nu_t = 1$	695	350.28649	0.70 ± 0.03	4.9	3.65 ± 0.42	34.6	0.08	...
CH ₃ OH	4 ₀ E–3 ₋₁ E	36	350.68766	1.87 ± 0.04	4.6	9.18 ± 0.40	34.1	0.08	...
CH ₃ OH	18 ₃ E–18 ₂ E, $\nu_t = 1$	812	350.72388	<0.25	...	<1.1	...	0.08	...
CH ₃ OH	1 ₁ A ⁺ –0 ₀ A ⁺	17	350.90510	2.38 ± 0.04	3.7	9.29 ± 0.33	34.4	0.08	...
CH ₃ OH	9 ₅ E–10 ₄ E	241	351.23648	0.97 ± 0.04	4.7	4.82 ± 0.40	34.5	0.08	...
¹³ CH ₃ OH	4 ₂ A ⁻ –5 ₁ A ⁻	60	242.37315	0.17 ± 0.02	5.1	0.93 ± 0.27	36.3	0.04	...
¹³ CH ₃ OH	15 ₃ A ⁺ –15 ₂ A ⁻	322	257.42179	0.48 ± 0.02	3.9	2.02 ± 0.18	34.5	0.03	...
¹³ CH ₃ OH	16 ₃ A ⁺ –16 ₂ A ⁻	358	258.15300	0.59 ± 0.02	4.6	2.90 ± 0.19	34.8	0.03	(7)
¹³ CH ₃ OH	17 ₃ A ⁺ –17 ₂ A ⁻	396	259.03649	<0.20	...	<0.9	...	0.03	(8)
¹³ CH ₃ OH	2 ₁ E–1 ₀ E	28	259.98653	0.54 ± 0.02	2.9	1.68 ± 0.16	34.5	0.03	(9)
¹³ CH ₃ OH	13 ₀ A ⁺ –12 ₁ A ⁺	206	338.75995	0.60 ± 0.04	3.7	2.33 ± 0.32	34.4	0.07	...
¹³ CH ₃ OH	1 ₁ A ⁺ –0 ₀ A ⁺	17	350.10312	0.58 ± 0.04	3.1	1.87 ± 0.28	34.7	0.08	...
¹³ CH ₃ OH	8 ₁ E–7 ₂ E	103	350.42158	0.49 ± 0.04	4.6	2.38 ± 0.41	34.0	0.08	...
CH ₂ DOH	11 _{2,9} o ₁ –11 _{1,10} o ₁	177	242.03360	0.32 ± 0.03	1.8	0.60 ± 0.14	33.2	0.04	...
CH ₂ DOH	5 _{2,3} e ₀ –5 _{1,4} e ₀	48	243.22599	0.56 ± 0.02	2.9	1.74 ± 0.17	35.5	0.04	...
CH ₂ DOH	4 _{2,2} e ₀ –4 _{1,3} e ₀	38	244.84113	0.35 ± 0.02	4.2	1.55 ± 0.25	34.4	0.04	...
CH ₂ DOH	10 _{2,8} o ₁ –10 _{1,9} o ₁	153	244.98885	0.13 ± 0.02	3.9	0.54 ± 0.22	34.7	0.04	...
CH ₂ DOH	5 _{2,3} o ₁ –5 _{1,4} o ₁	68	257.39451	0.26 ± 0.02	2.2	0.61 ± 0.10	34.4	0.03	...
CH ₂ DOH	4 _{2,3} e ₁ –3 _{1,3} o ₁	48	257.89567	0.30 ± 0.02	2.3	0.72 ± 0.09	34.6	0.03	...
CH ₂ DOH	4 _{2,3} e ₀ –4 _{1,4} e ₀	38	258.33711	0.42 ± 0.02	2.8	1.25 ± 0.12	34.3	0.03	...
CH ₂ DOH	9 _{0,9} e ₀ –8 _{1,8} e ₀	96	337.34866	0.63 ± 0.04	2.8	1.84 ± 0.25	35.1	0.07	...
CH ₂ DOH	6 _{1,6} e ₀ –5 _{0,5} e ₀	48	338.95711	0.39 ± 0.04	3.5	1.46 ± 0.32	35.1	0.07	...
CH ₂ DOH	15 _{2,14} o ₁ –15 _{1,14} e ₁	292	339.48572	0.24 ± 0.03	2.2	0.56 ± 0.20	34.9	0.07	...
CH ₂ DOH	6 _{2,4} e ₁ –5 _{1,4} o ₁	72	340.12709	0.42 ± 0.03	3.5	1.55 ± 0.43	34.8	0.07	...
CH ₂ DOH	13 _{1,13} e ₀ –12 _{0,12} e ₁	196	340.24344	0.57 ± 0.03	2.9	1.76 ± 0.33	34.2	0.07	(10)
CH ₂ DOH	2 _{2,1} e ₀ –1 _{0,1} e ₀	23	340.34829	0.29 ± 0.04	3.7	1.15 ± 0.32	34.1	0.07	...
CH ₂ DOH	13 _{4,9} e ₁ –13 _{3,11} o ₁	267	349.18383	0.24 ± 0.04	2.2	0.57 ± 0.22	34.3	0.08	...
CH ₂ DOH	12 _{4,8} e ₁ –12 _{3,10} o ₁	239	349.35613	0.22 ± 0.04	3.1	0.75 ± 0.30	35.3	0.08	...
CH ₂ DOH	11 _{4,8} e ₁ –11 _{3,8} o ₁	213	349.49521	0.22 ± 0.04	3.7	0.85 ± 0.32	34.3	0.08	(11)
CH ₂ DOH	11 _{4,7} e ₁ –11 _{3,9} o ₁	213	349.50887	0.47 ± 0.04	1.6	0.80 ± 0.22	34.8	0.08	...
CH ₂ DOH	10 _{4,6} e ₁ –10 _{3,8} o ₁	190	349.64360	0.32 ± 0.04	2.8	0.97 ± 0.28	34.4	0.08	...
CH ₂ DOH	9 _{4,5} e ₁ –9 _{3,7} o ₁	168	349.76168	0.30 ± 0.04	7.2	2.31 ± 0.62	36.4	0.08	(12)
CH ₂ DOH	8 _{4,5} e ₁ –8 _{3,5} o ₁	149	349.86211	0.34 ± 0.04	6.0	2.15 ± 0.55	33.4	0.08	(12)
CH ₂ DOH	7 _{4,4} e ₁ –7 _{3,4} o ₁	132	349.95168	0.48 ± 0.03	3.4	1.73 ± 0.29	34.3	0.08	(12)
CH ₂ DOH	6 _{4,3} e ₁ –6 _{3,3} o ₁	117	350.02735	0.64 ± 0.04	2.4	1.60 ± 0.26	34.2	0.08	(12)
CH ₂ DOH	5 _{4,2} e ₁ –5 _{3,2} o ₁	104	350.09024	0.57 ± 0.04	2.0	1.21 ± 0.23	34.2	0.08	(12)
CH ₂ DOH	4 _{4,1} e ₁ –4 _{3,1} o ₁	94	350.14130	0.33 ± 0.03	4.0	1.41 ± 0.37	33.8	0.08	(12)
CH ₂ DOH	6 _{2,5} e ₁ –5 _{1,5} o ₁	72	350.45387	0.53 ± 0.03	2.6	1.46 ± 0.28	34.2	0.08	...
CH ₂ DOH	5 _{1,4} e ₁ –5 _{0,5} e ₀	49	350.63207	0.58 ± 0.04	3.2	1.98 ± 0.32	35.2	0.08	...
CH ₂ DOH	2 _{2,1} o ₁ –1 _{0,1} o ₁	42	351.60685	<0.15	...	<0.7	...	0.08	...
CH ₂ DOH	8 _{1,8} e ₀ –7 _{1,7} e ₀	80	351.79643	0.54 ± 0.04	2.5	1.44 ± 0.30	34.4	0.08	...
CH ₂ DOH	2 _{2,0} o ₁ –1 _{1,1} o ₁	42	352.34437	<0.15	...	<0.7	...	0.08	...
CH ₂ DOH	8 _{1,8} e ₁ –7 _{1,7} e ₁	93	352.80196	0.40 ± 0.04	2.6	1.10 ± 0.23	34.4	0.08	...

NOTE—(1) Blend of two CH₃OH lines with similar spectroscopic constants. (2) Blend of three CH₃OH lines with similar spectroscopic constants. (3) Possible blend with C₂H₅OH. (4) Blend with CH₃CN. (5) Blend with HCOOCH₃. (6) Blend with ³⁴SO. (7) Partial blend with HC¹⁵N. (8) Possible blend with HDCO. (9) Blend with CH₃OCH₃. (10) Partial blend with CN. (11) Tentative detection. (12) Blend of two CH₂DOH lines with similar spectroscopic constants.

Table A5. Line Parameters for C₂H₅OH

Molecule	Transition	E_u	Frequency	T_{br}	ΔV	$\int T_{br} dV$	V_{LSR}	RMS	Note
		(K)	(GHz)	(K)	(km/s)	(K km/s)	(km/s)	(K)	
C ₂ H ₅ OH	14 _{11,3} –13 _{11,2}	297	242.17548	0.15 ± 0.02	5.4	0.87 ± 0.40	34.7	0.04	(1)
C ₂ H ₅ OH	14 _{9,5} –13 _{9,4}	248	242.22129	0.16 ± 0.02	5.5	0.93 ± 0.29	33.7	0.04	(1)
C ₂ H ₅ OH	14 _{8,6} –13 _{8,5}	228	242.27115	0.13 ± 0.02	4.1	0.57 ± 0.23	34.6	0.04	(1)
C ₂ H ₅ OH	14 _{7,8} –13 _{7,7}	209	242.34984	0.30 ± 0.02	4.1	1.30 ± 0.23	35.7	0.04	(1)
C ₂ H ₅ OH	14 _{10,4} –13 _{10,3}	266	242.42987	0.36 ± 0.02	1.6	0.62 ± 0.08	35.3	0.04	(2)
C ₂ H ₅ OH	14 _{6,9} –13 _{6,8}	193	242.47550	0.35 ± 0.02	4.3	1.60 ± 0.23	34.6	0.04	(1)
C ₂ H ₅ OH	14 _{7,8} –13 _{7,7}	204	242.52422	0.37 ± 0.02	1.5	0.57 ± 0.08	34.9	0.04	(1)
C ₂ H ₅ OH	14 _{6,9} –13 _{6,8}	188	242.62561	0.42 ± 0.02	1.5	0.67 ± 0.08	34.6	0.04	(1)
C ₂ H ₅ OH	14 _{5,10} –13 _{5,9}	180	242.68502	0.13 ± 0.02	3.6	0.51 ± 0.19	34.6	0.04	(1)
C ₂ H ₅ OH	14 _{5,9} –13 _{5,8}	180	242.69305	0.35 ± 0.02	1.5	0.56 ± 0.08	34.7	0.04	...
C ₂ H ₅ OH	14 _{3,12} –13 _{3,11}	160	242.77011	0.15 ± 0.02	3.4	0.55 ± 0.17	35.2	0.04	...
C ₂ H ₅ OH	14 _{5,10} –13 _{5,9}	175	242.81644	0.09 ± 0.02	3.3	0.33 ± 0.18	33.8	0.04	(3)
C ₂ H ₅ OH	14 _{5,9} –13 _{5,8}	175	242.82512	0.10 ± 0.02	3.9	0.42 ± 0.21	35.6	0.04	...
C ₂ H ₅ OH	14 _{4,11} –13 _{4,10}	169	242.99597	0.28 ± 0.03	3.1	0.91 ± 0.19	34.2	0.04	...
C ₂ H ₅ OH	14 _{4,11} –13 _{4,10}	164	243.12034	0.38 ± 0.02	1.5	0.58 ± 0.08	35.2	0.04	...
C ₂ H ₅ OH	14 _{4,10} –13 _{4,9}	169	243.20653	0.36 ± 0.02	1.7	0.64 ± 0.09	34.3	0.04	...
C ₂ H ₅ OH	14 _{1,13} –13 _{1,12}	152	244.63396	0.24 ± 0.02	3.8	0.99 ± 0.21	34.5	0.04	...
C ₂ H ₅ OH	14 _{3,11} –13 _{3,10}	160	245.32715	0.39 ± 0.02	1.4	0.60 ± 0.08	34.6	0.04	...
C ₂ H ₅ OH	16 _{1,15} –15 _{2,14}	117	257.06090	0.26 ± 0.02	5.3	1.49 ± 0.23	34.1	0.03	...
C ₂ H ₅ OH	14 _{3,11} –13 _{2,11}	156	259.32264	0.09 ± 0.02	4.3	0.40 ± 0.19	34.2	0.03	(3)
C ₂ H ₅ OH	15 _{9,6} –14 _{9,5}	261	259.53913	0.28 ± 0.02	2.4	0.71 ± 0.10	34.4	0.03	(1)
C ₂ H ₅ OH	15 _{7,9} –14 _{7,8}	222	259.69790	0.11 ± 0.02	4.7	0.57 ± 0.21	34.4	0.03	(1)
C ₂ H ₅ OH	15 _{10,5} –14 _{10,4}	279	259.75653	0.27 ± 0.02	2.4	0.69 ± 0.14	34.9	0.03	(1)
C ₂ H ₅ OH	15 _{9,6} –14 _{9,5}	255	259.77714	0.28 ± 0.02	1.5	0.43 ± 0.07	34.5	0.03	(1)
C ₂ H ₅ OH	15 _{8,8} –14 _{8,7}	235	259.81444	0.29 ± 0.02	2.3	0.72 ± 0.10	34.0	0.03	(1)
C ₂ H ₅ OH	15 _{6,10} –14 _{6,9}	206	259.85218	0.30 ± 0.02	2.3	0.74 ± 0.10	34.7	0.03	(1)
C ₂ H ₅ OH	15 _{7,9} –14 _{7,8}	216	259.88507	0.28 ± 0.02	3.1	0.93 ± 0.13	34.7	0.03	(1)
C ₂ H ₅ OH	15 _{3,13} –14 _{3,12}	172	260.04664	0.28 ± 0.02	2.2	0.64 ± 0.10	35.2	0.03	...
C ₂ H ₅ OH	15 _{5,11} –14 _{5,10}	192	260.10761	0.09 ± 0.01	4.7	0.43 ± 0.24	34.5	0.03	(3)
C ₂ H ₅ OH	15 _{5,10} –14 _{5,9}	192	260.12276	0.11 ± 0.02	4.6	0.52 ± 0.20	34.5	0.03	...
C ₂ H ₅ OH	15 _{3,13} –14 _{3,12}	168	260.14168	0.29 ± 0.02	3.5	1.06 ± 0.15	34.9	0.03	...
C ₂ H ₅ OH	15 _{5,10} –14 _{5,9}	187	260.26613	0.27 ± 0.02	2.5	0.71 ± 0.11	33.9	0.03	...
C ₂ H ₅ OH	15 _{4,12} –14 _{4,11}	181	260.45773	0.12 ± 0.02	4.4	0.57 ± 0.19	35.1	0.03	...
C ₂ H ₅ OH	15 _{4,12} –14 _{4,11}	176	260.59133	0.28 ± 0.02	2.4	0.74 ± 0.10	34.5	0.03	...
C ₂ H ₅ OH	20 _{2,19} –19 _{2,18}	234	338.88792	0.39 ± 0.04	5.0	2.07 ± 0.43	35.5	0.07	(4)
C ₂ H ₅ OH	16 _{7,9} –16 _{6,10}	176	338.67173	0.35 ± 0.04	4.7	1.76 ± 0.40	33.4	0.07	(1)
C ₂ H ₅ OH	14 _{7,7} –14 _{6,8}	150	339.06106	0.28 ± 0.03	4.0	1.21 ± 0.34	34.5	0.07	(1)
C ₂ H ₅ OH	13 _{7,6} –13 _{6,7}	138	339.20154	0.38 ± 0.03	1.9	0.79 ± 0.25	33.9	0.07	(1)
C ₂ H ₅ OH	12 _{7,5} –12 _{6,6}	127	339.31253	0.24 ± 0.03	4.9	1.24 ± 0.40	35.9	0.07	...
C ₂ H ₅ OH	11 _{7,4} –11 _{6,5}	117	339.39844	0.25 ± 0.03	4.0	1.07 ± 0.33	34.6	0.07	(1)
C ₂ H ₅ OH	8 _{7,1} –8 _{6,2}	92	339.54409	0.30 ± 0.04	2.1	0.67 ± 0.20	34.4	0.07	(1)
C ₂ H ₅ OH	9 _{4,6} –8 _{3,5}	58	339.97892	0.24 ± 0.04	3.8	0.97 ± 0.32	35.0	0.07	...
C ₂ H ₅ OH	20 _{4,16} –19 _{4,15}	252	350.36506	0.40 ± 0.04	3.9	1.65 ± 0.33	35.7	0.08	(5)
C ₂ H ₅ OH	20 _{2,19} –19 _{1,18}	179	350.53435	0.30 ± 0.04	3.3	1.06 ± 0.29	34.9	0.08	...
C ₂ H ₅ OH	13 _{5,8} –12 _{4,8}	163	351.96548	0.25 ± 0.03	2.0	0.55 ± 0.18	35.3	0.08	...

NOTE— (1) Blend of two C₂H₅OH lines with similar spectroscopic constants. (2) Blend of four C₂H₅OH lines with similar spectroscopic constants. (3) Tentative detection. (4) Blend of three C₂H₅OH lines with similar spectroscopic constants. (5) Possible blend with CH₃CHO.

Table A6. Line Parameters for HCOOCH₃

Molecule	Transition	E_u	Frequency	T_{br}	ΔV	$\int T_{br} dV$	V_{LSR}	RMS	Note
		(K)	(GHz)	(K)	(km/s)	(K km/s)	(km/s)	(K)	
HCOOCH ₃	20 _{4,17} –19 _{4,16} A $\nu_t = 1$	322	242.61007	0.35 ± 0.02	2.4	0.92 ± 0.14	34.3	0.04	...
HCOOCH ₃	19 _{5,14} –18 _{5,13} A	130	242.89603	0.74 ± 0.02	3.6	2.85 ± 0.19	34.5	0.04	...
HCOOCH ₃	19 _{4,15} –18 _{4,14} A $\nu_t = 1$	313	244.06667	0.35 ± 0.02	3.4	1.28 ± 0.18	34.4	0.04	...
HCOOCH ₃	20 _{10,10} –19 _{10,9} E $\nu_t = 1$	378	244.11242	0.13 ± 0.02	4.0	0.56 ± 0.22	33.9	0.04	...
HCOOCH ₃	20 _{12,8} –19 _{12,7} A $\nu_t = 1$	407	244.19830	0.17 ± 0.02	4.8	0.89 ± 0.25	34.5	0.04	(1)
HCOOCH ₃	20 _{10,11} –19 _{10,10} A $\nu_t = 1$	377	244.52854	0.38 ± 0.02	3.0	1.21 ± 0.16	34.7	0.04	(1)
HCOOCH ₃	20 _{4,17} –19 _{4,16} E	135	244.58034	0.74 ± 0.02	4.6	3.64 ± 0.24	34.7	0.04	...
HCOOCH ₃	20 _{4,17} –19 _{4,16} A	135	244.59405	0.78 ± 0.02	3.6	3.02 ± 0.19	34.8	0.04	...
HCOOCH ₃	20 _{11,10} –19 _{11,9} E $\nu_t = 1$	391	244.72966	0.29 ± 0.03	2.2	0.67 ± 0.12	34.1	0.04	...
HCOOCH ₃	20 _{9,12} –19 _{9,11} A $\nu_t = 1$	365	244.84534	0.43 ± 0.02	2.9	1.33 ± 0.17	34.3	0.04	(1)
HCOOCH ₃	19 _{4,15} –18 _{4,14} E $\nu_t = 1$	313	244.90213	0.30 ± 0.02	3.6	1.17 ± 0.19	34.4	0.04	...
HCOOCH ₃	20 _{10,11} –19 _{10,10} E $\nu_t = 1$	377	245.08271	0.15 ± 0.02	4.0	0.65 ± 0.22	35.3	0.04	...
HCOOCH ₃	20 _{8,12} –19 _{8,11} E $\nu_t = 1$	354	245.26174	0.17 ± 0.02	5.0	0.88 ± 0.26	34.7	0.04	...
HCOOCH ₃	20 _{8,13} –19 _{8,12} A $\nu_t = 1$	354	245.34255	0.34 ± 0.02	3.2	1.14 ± 0.19	34.2	0.04	...
HCOOCH ₃	20 _{9,12} –19 _{9,11} E $\nu_t = 1$	365	245.54388	0.28 ± 0.02	2.5	0.75 ± 0.13	35.0	0.04	...
HCOOCH ₃	20 _{15,5} –19 _{15,4} A	273	245.65121	0.42 ± 0.02	3.2	1.43 ± 0.17	34.7	0.04	(1)
HCOOCH ₃	20 _{15,5} –19 _{15,4} E	273	245.65678	0.29 ± 0.02	3.1	0.98 ± 0.17	34.5	0.04	...
HCOOCH ₃	20 _{15,6} –19 _{15,5} E	273	245.67298	0.33 ± 0.02	2.4	0.83 ± 0.13	34.1	0.04	...
HCOOCH ₃	23 _{2,22} –22 _{2,21} A $\nu_t = 1$	343	256.99936	0.36 ± 0.02	4.2	1.62 ± 0.18	34.8	0.03	...
HCOOCH ₃	23 _{1,22} –22 _{1,21} A $\nu_t = 1$	343	257.01547	0.36 ± 0.02	3.6	1.39 ± 0.16	34.3	0.03	...
HCOOCH ₃	21 _{9,12} –20 _{9,11} E $\nu_t = 1$	377	257.04978	0.46 ± 0.02	4.5	2.18 ± 0.19	34.2	0.03	...
HCOOCH ₃	20 _{5,15} –19 _{5,14} E	143	257.22661	0.69 ± 0.02	4.1	3.03 ± 0.17	34.6	0.03	...
HCOOCH ₃	20 _{5,15} –19 _{5,14} A	143	257.25267	0.76 ± 0.02	4.4	3.58 ± 0.21	34.4	0.03	(1)
HCOOCH ₃	21 _{9,13} –20 _{9,12} A $\nu_t = 1$	377	257.29779	0.42 ± 0.02	3.7	1.66 ± 0.16	34.0	0.03	(1)
HCOOCH ₃	20 _{4,16} –19 _{4,15} E $\nu_t = 1$	325	257.58889	0.38 ± 0.02	4.6	1.86 ± 0.21	35.4	0.03	...
HCOOCH ₃	22 _{3,20} –21 _{3,19} E	152	257.69033	0.72 ± 0.02	3.7	2.88 ± 0.16	34.6	0.03	...
HCOOCH ₃	22 _{3,20} –21 _{3,19} A	152	257.69949	0.73 ± 0.02	3.5	2.75 ± 0.15	34.5	0.03	...
HCOOCH ₃	21 _{8,13} –20 _{8,12} E $\nu_t = 1$	366	257.83109	0.27 ± 0.02	3.7	1.05 ± 0.16	34.1	0.03	...
HCOOCH ₃	21 _{8,14} –20 _{8,13} A $\nu_t = 1$	366	257.88987	0.24 ± 0.02	2.3	0.59 ± 0.11	33.8	0.03	...
HCOOCH ₃	21 _{8,13} –20 _{8,12} A $\nu_t = 1$	366	257.90613	0.26 ± 0.02	2.4	0.66 ± 0.11	35.3	0.03	...
HCOOCH ₃	21 _{16,5} –20 _{16,4} E	306	257.91989	0.25 ± 0.02	3.5	0.93 ± 0.15	34.0	0.03	...
HCOOCH ₃	21 _{16,6} –20 _{16,5} E	306	257.93383	0.21 ± 0.02	3.2	0.73 ± 0.15	34.7	0.03	...
HCOOCH ₃	21 _{15,6} –20 _{15,5} A	285	258.00176	0.46 ± 0.02	3.2	1.55 ± 0.14	34.4	0.03	(1)
HCOOCH ₃	24 _{1,24} –23 _{1,23} A $\nu_t = 1$	345	258.01075	0.63 ± 0.01	3.9	2.58 ± 0.18	34.5	0.03	(2)
HCOOCH ₃	21 _{15,7} –20 _{15,6} E	285	258.02424	0.30 ± 0.02	2.2	0.69 ± 0.11	35.0	0.03	...
HCOOCH ₃	21 _{9,13} –20 _{9,12} E $\nu_t = 1$	377	258.03797	0.31 ± 0.02	1.4	0.48 ± 0.06	33.7	0.03	...
HCOOCH ₃	24 _{1,24} –23 _{1,23} E $\nu_t = 1$	345	258.05504	0.69 ± 0.02	4.9	3.57 ± 0.21	35.0	0.03	(1)
HCOOCH ₃	22 _{2,20} –21 _{2,19} E	152	258.08104	0.85 ± 0.02	5.4	4.93 ± 0.23	34.3	0.03	...
HCOOCH ₃	22 _{2,20} –21 _{2,19} A	152	258.08949	0.76 ± 0.02	3.9	3.14 ± 0.18	34.6	0.03	...
HCOOCH ₃	21 _{14,7} –20 _{14,6} A	266	258.12119	0.69 ± 0.02	4.5	3.26 ± 0.20	33.9	0.03	(2)
HCOOCH ₃	21 _{14,8} –20 _{14,7} E	266	258.14209	0.35 ± 0.02	3.8	1.41 ± 0.16	34.7	0.03	...
HCOOCH ₃	21 _{13,8} –20 _{13,7} A	248	258.27743	0.84 ± 0.01	6.3	5.64 ± 0.36	36.0	0.03	(2)
HCOOCH ₃	21 _{12,9} –20 _{12,8} E	232	258.47645	0.47 ± 0.01	5.1	2.58 ± 0.24	35.3	0.03	...
HCOOCH ₃	21 _{12,9} –20 _{12,8} A	232	258.48298	0.62 ± 0.02	5.8	3.84 ± 0.27	34.9	0.03	(1)
HCOOCH ₃	23 _{2,22} –22 _{2,21} E	156	258.49087	0.79 ± 0.02	3.9	3.27 ± 0.17	34.7	0.03	...
HCOOCH ₃	23 _{2,22} –22 _{2,21} A	156	258.49624	0.83 ± 0.01	5.0	4.38 ± 0.28	34.4	0.03	(1)
HCOOCH ₃	23 _{1,22} –22 _{1,21} E	156	258.50273	0.81 ± 0.01	3.5	3.00 ± 0.18	34.6	0.03	...
HCOOCH ₃	23 _{1,22} –22 _{1,21} A	156	258.50818	0.85 ± 0.02	3.3	2.97 ± 0.14	34.5	0.03	...
HCOOCH ₃	21 _{5,17} –20 _{5,16} A $\nu_t = 1$	341	258.70105	0.33 ± 0.02	2.7	0.93 ± 0.12	34.3	0.03	...
HCOOCH ₃	21 _{11,10} –20 _{11,9} E	217	258.74625	0.50 ± 0.02	3.5	1.84 ± 0.15	35.0	0.03	...
HCOOCH ₃	21 _{11,11} –20 _{11,10} A	217	258.75667	0.62 ± 0.02	4.9	3.20 ± 0.21	34.9	0.03	(1)
HCOOCH ₃	21 _{11,11} –20 _{11,10} E	217	258.76997	0.59 ± 0.02	4.8	3.03 ± 0.20	35.1	0.03	(1)

Table A6 *continued*

Table A6 (continued)

Molecule	Transition	E_u	Frequency	T_{br}	ΔV	$\int T_{br} dV$	V_{LSR}	RMS	Note
		(K)	(GHz)	(K)	(km/s)	(K km/s)	(km/s)	(K)	
HCOOCH ₃	21 _{3,18} –20 _{3,17} A $\nu_t = 1$	333	258.77532	0.35 ± 0.02	2.9	1.07 ± 0.12	35.1	0.03	...
HCOOCH ₃	21 _{7,14} –20 _{7,13} A $\nu_t = 1$	356	259.00387	0.39 ± 0.02	4.3	1.77 ± 0.32	34.2	0.03	...
HCOOCH ₃	21 _{7,14} –20 _{7,13} E $\nu_t = 1$	356	259.02583	0.29 ± 0.02	2.2	0.67 ± 0.09	34.6	0.03	...
HCOOCH ₃	21 _{10,11} –20 _{10,10} E	203	259.11395	0.46 ± 0.02	4.3	2.09 ± 0.19	34.6	0.03	...
HCOOCH ₃	21 _{10,12} –20 _{10,11} A	203	259.12818	0.77 ± 0.02	4.1	3.37 ± 0.17	34.7	0.03	(1)
HCOOCH ₃	21 _{10,12} –20 _{10,11} E	203	259.13793	0.45 ± 0.02	3.4	1.63 ± 0.14	34.6	0.03	...
HCOOCH ₃	21 _{3,18} –20 _{3,17} E $\nu_t = 1$	333	259.26499	0.28 ± 0.02	3.3	0.99 ± 0.14	34.2	0.03	...
HCOOCH ₃	20 _{4,16} –19 _{4,15} A	139	259.52181	0.68 ± 0.02	4.1	2.98 ± 0.17	35.0	0.03	...
HCOOCH ₃	21 _{9,12} –20 _{9,11} E	190	259.62930	0.46 ± 0.02	3.6	1.76 ± 0.16	34.7	0.03	...
HCOOCH ₃	21 _{9,13} –20 _{9,12} A	190	259.64653	0.85 ± 0.02	4.8	4.37 ± 0.21	33.8	0.03	(1)
HCOOCH ₃	21 _{9,13} –20 _{9,12} E	190	259.65308	0.53 ± 0.02	3.5	2.01 ± 0.15	34.4	0.03	...
HCOOCH ₃	21 _{3,18} –20 _{3,17} E	147	260.24450	0.66 ± 0.02	4.1	2.89 ± 0.17	34.7	0.03	...
HCOOCH ₃	21 _{8,14} –20 _{8,13} A	179	260.39273	0.59 ± 0.02	3.5	2.22 ± 0.15	34.6	0.03	...
HCOOCH ₃	21 _{8,13} –20 _{8,12} A	179	260.41533	0.57 ± 0.02	4.0	2.42 ± 0.17	34.6	0.03	...
HCOOCH ₃	27 _{8,20} –26 _{8,19} A	267	337.50352	0.39 ± 0.04	2.9	1.19 ± 0.29	34.8	0.07	...
HCOOCH ₃	27 _{8,19} –26 _{8,18} A	267	338.35579	0.37 ± 0.04	3.4	1.33 ± 0.31	34.7	0.07	...
HCOOCH ₃	27 _{7,21} –26 _{7,20} E	258	338.39632	0.53 ± 0.03	4.4	2.46 ± 0.39	34.9	0.07	(1)
HCOOCH ₃	13 _{7,7} –12 _{6,6} A	86	339.18591	0.19 ± 0.04	1.5	0.30 ± 0.14	34.3	0.07	(3)
HCOOCH ₃	13 _{7,6} –12 _{6,7} A	86	339.19634	0.21 ± 0.03	2.7	0.63 ± 0.25	34.7	0.07	(3)
HCOOCH ₃	29 _{3,26} –28 _{3,25} A $\nu_t = 1$	450	339.88222	0.24 ± 0.04	3.8	0.99 ± 0.34	34.6	0.07	...
HCOOCH ₃	28 _{5,24} –27 _{5,23} E	257	340.74199	0.58 ± 0.04	4.9	3.03 ± 0.42	34.3	0.07	...
HCOOCH ₃	28 _{5,24} –27 _{5,23} A	257	340.75476	0.41 ± 0.03	5.3	2.33 ± 0.45	34.7	0.07	...
HCOOCH ₃	29 _{5,25} –28 _{5,24} E $\nu_t = 1$	460	349.68548	0.26 ± 0.04	2.1	0.58 ± 0.21	35.1	0.08	...
HCOOCH ₃	30 _{4,27} –29 _{4,26} A $\nu_t = 1$	467	350.13257	0.71 ± 0.03	2.0	1.48 ± 0.30	33.5	0.08	...
HCOOCH ₃	30 _{3,27} –29 _{3,26} A $\nu_t = 1$	467	350.30254	0.33 ± 0.04	4.2	1.48 ± 0.39	34.0	0.08	...
HCOOCH ₃	30 _{4,27} –29 _{4,26} E $\nu_t = 1$	467	350.55020	0.33 ± 0.04	3.7	1.27 ± 0.37	33.9	0.08	...
HCOOCH ₃	27 _{6,21} –26 _{6,20} E	252	350.91952	0.49 ± 0.03	4.4	2.27 ± 0.52	34.6	0.08	...
HCOOCH ₃	27 _{6,21} –26 _{6,20} A	252	350.94733	0.53 ± 0.04	3.9	2.21 ± 0.35	34.4	0.08	...
HCOOCH ₃	28 _{7,22} –27 _{7,21} E	275	350.99804	0.50 ± 0.04	4.3	2.29 ± 0.37	34.8	0.08	...
HCOOCH ₃	28 _{7,22} –27 _{7,21} A	275	351.01591	0.49 ± 0.04	4.9	2.57 ± 0.43	35.2	0.08	...
HCOOCH ₃	29 _{5,25} –28 _{5,24} E	274	351.51710	0.40 ± 0.04	4.7	1.99 ± 0.40	35.2	0.08	...
HCOOCH ₃	29 _{5,25} –28 _{5,24} A	274	351.52916	0.41 ± 0.04	4.6	2.02 ± 0.39	35.0	0.08	...
HCOOCH ₃	28 _{8,20} –27 _{8,19} E	284	351.82345	0.39 ± 0.04	4.0	1.67 ± 0.35	34.6	0.08	...
HCOOCH ₃	28 _{8,20} –27 _{8,19} A	284	351.84219	0.44 ± 0.04	3.4	1.59 ± 0.30	35.0	0.08	...
HCOOCH ₃	30 _{4,27} –29 _{4,26} E	281	352.28276	0.41 ± 0.04	3.0	1.31 ± 0.28	34.6	0.08	...
HCOOCH ₃	30 _{4,27} –29 _{4,26} A	281	352.29258	0.40 ± 0.04	4.5	1.87 ± 0.38	34.7	0.08	...
HCOOCH ₃	30 _{3,27} –29 _{3,26} E	281	352.40468	0.51 ± 0.04	2.0	1.09 ± 0.17	34.1	0.08	...
HCOOCH ₃	30 _{3,27} –29 _{3,26} A	281	352.41414	0.53 ± 0.04	3.7	2.09 ± 0.32	34.4	0.08	...
HCOOCH ₃	33 _{1,33} –32 _{1,32} A $\nu_t = 1$	479	352.81684	0.32 ± 0.04	3.0	1.00 ± 0.26	33.7	0.08	(1)

NOTE— (1) Blend of two HCOOCH₃ lines with similar spectroscopic constants. (2) Blend of three HCOOCH₃ lines with similar spectroscopic constants. (3) Tentative detection.

Table A7. Line Parameters for CH₃OCH₃

Molecule	Transition	E_u	Frequency	T_{br}	ΔV	$\int T_{br} dV$	V_{LSR}	RMS	Note
		(K)	(GHz)	(K)	(km/s)	(K km/s)	(km/s)	(K)	
CH ₃ OCH ₃	5 _{3,2} –4 _{2,3} EE	26	241.52872	0.59 ± 0.02	5.0	3.12 ± 0.26	33.3	0.04	(1)

Table A7 continued

Table A7 (continued)

Molecule	Transition	E_u	Frequency	T_{br}	ΔV	$\int T_{br} dV$	V_{LSR}	RMS	Note
		(K)	(GHz)	(K)	(km/s)	(K km/s)	(km/s)	(K)	
CH_3OCH_3	$5_{3,2}-4_{2,3}$ AA	26	241.53103	0.58 ± 0.02	5.2	3.23 ± 0.32	36.3	0.04	...
CH_3OCH_3	$21_{3,18}-20_{4,17}$ EE	226	241.63730	0.25 ± 0.02	4.7	1.25 ± 0.29	34.8	0.04	(1)
CH_3OCH_3	$13_{1,13}-12_{0,12}$ EE	81	241.94654	0.92 ± 0.02	4.2	4.12 ± 0.23	34.5	0.04	(2)
CH_3OCH_3	$23_{2,22}-23_{1,23}$ EE	253	244.50830	0.16 ± 0.02	4.2	0.72 ± 0.24	33.5	0.04	...
CH_3OCH_3	$23_{2,22}-23_{1,23}$ AA	253	244.51274	0.12 ± 0.02	3.3	0.40 ± 0.17	34.5	0.04	...
CH_3OCH_3	$18_{2,16}-17_{3,15}$ EE	164	257.04988	0.46 ± 0.02	4.4	2.16 ± 0.19	34.4	0.03	(2)
CH_3OCH_3	$27_{3,25}-27_{2,26}$ EE	356	257.61453	0.09 ± 0.02	8.1	0.79 ± 0.37	34.0	0.03	(2) (3)
CH_3OCH_3	$14_{1,14}-13_{0,13}$ EE	93	258.54906	1.17 ± 0.02	4.4	5.43 ± 0.19	34.2	0.03	(2)
CH_3OCH_3	$17_{5,12}-17_{4,13}$ EE	175	259.31195	0.46 ± 0.07	9.0	3.34 ± 0.16	35.0	0.03	(2)
CH_3OCH_3	$6_{3,4}-5_{2,3}$ EE	32	259.48973	0.47 ± 0.01	3.0	1.48 ± 0.20	34.4	0.03	(1)
CH_3OCH_3	$6_{3,4}-5_{2,3}$ AA	32	259.49375	0.39 ± 0.01	2.9	1.21 ± 0.19	34.4	0.03	...
CH_3OCH_3	$23_{5,19}-23_{4,20}$ EE	287	259.69007	0.41 ± 0.02	4.3	1.87 ± 0.18	34.1	0.03	(2)
CH_3OCH_3	$21_{5,17}-21_{4,18}$ EE	246	259.73215	0.47 ± 0.02	5.8	2.87 ± 0.25	34.4	0.03	(2)
CH_3OCH_3	$20_{5,16}-20_{4,17}$ EE	227	259.98441	0.53 ± 0.01	3.5	1.99 ± 0.20	35.6	0.03	(2)
CH_3OCH_3	$24_{5,20}-24_{4,21}$ EE	309	260.00439	0.43 ± 0.02	5.0	2.33 ± 0.21	34.0	0.03	(2)
CH_3OCH_3	$19_{5,15}-19_{4,16}$ EE	208	260.32922	0.46 ± 0.02	4.1	2.03 ± 0.21	34.4	0.03	(2)
CH_3OCH_3	$25_{5,21}-25_{4,22}$ EE	332	260.61685	0.35 ± 0.02	3.0	1.13 ± 0.15	35.0	0.03	(2)
CH_3OCH_3	$21_{2,19}-20_{3,18}$ AA	220	337.42046	0.57 ± 0.04	3.2	1.95 ± 0.32	34.6	0.07	...
CH_3OCH_3	$7_{4,4}-6_{3,3}$ AE	48	337.72300	0.55 ± 0.04	2.3	1.33 ± 0.28	35.1	0.07	...
CH_3OCH_3	$7_{4,3}-6_{3,3}$ EE	48	337.73219	0.40 ± 0.04	4.5	1.88 ± 0.38	35.4	0.07	...
CH_3OCH_3	$7_{4,4}-6_{3,4}$ EE	48	337.77802	0.40 ± 0.03	3.8	1.59 ± 0.32	33.8	0.07	...
CH_3OCH_3	$7_{4,3}-6_{3,4}$ AA	48	337.78721	0.71 ± 0.03	5.8	4.41 ± 0.51	34.8	0.07	...
CH_3OCH_3	$19_{1,18}-18_{2,17}$ EE	176	339.49153	0.60 ± 0.04	3.9	2.50 ± 0.33	34.5	0.07	...
CH_3OCH_3	$10_{3,7}-9_{2,8}$ EE	63	340.61262	0.45 ± 0.03	7.0	3.35 ± 0.59	35.1	0.07	...
CH_3OCH_3	$11_{2,9}-10_{1,10}$ EE	66	349.80618	0.31 ± 0.04	4.6	1.52 ± 0.41	33.6	0.08	...

NOTE—(1) Blend of three CH_3OCH_3 lines with similar spectroscopic constants. (2) Blend of four CH_3OCH_3 lines with similar spectroscopic constants. (3) Tentative detection.

Table A8. Line Parameters for $\text{C}_2\text{H}_5\text{CN}$ and NH_2CHO

Molecule	Transition	E_u	Frequency	T_{br}	ΔV	$\int T_{br} dV$	V_{LSR}	RMS	Note
		(K)	(GHz)	(K)	(km/s)	(K km/s)	(km/s)	(K)	
$\text{C}_2\text{H}_5\text{CN}$	$27_{3,25}-26_{3,24}$	173	241.62587	0.13 ± 0.02	4.9	0.69 ± 0.29	33.3	0.04	...
$\text{C}_2\text{H}_5\text{CN}$	$27_{9,18}-26_{9,17}$	253	241.93218	0.23 ± 0.03	3.6	0.86 ± 0.21	33.9	0.04	(1)
$\text{C}_2\text{H}_5\text{CN}$	$27_{12,15}-26_{12,14}$	322	241.95905	0.12 ± 0.02	3.1	0.40 ± 0.16	34.2	0.04	(2)
$\text{C}_2\text{H}_5\text{CN}$	$27_{8,20}-26_{8,19}$	234	241.97045	0.30 ± 0.02	1.8	0.56 ± 0.10	33.5	0.04	(2)
$\text{C}_2\text{H}_5\text{CN}$	$27_{13,14}-26_{13,13}$	350	241.99710	0.12 ± 0.02	3.2	0.40 ± 0.17	33.2	0.04	(2)
$\text{C}_2\text{H}_5\text{CN}$	$27_{7,21}-26_{7,20}$	217	242.05249	0.23 ± 0.02	4.0	0.97 ± 0.22	34.2	0.04	(2)
$\text{C}_2\text{H}_5\text{CN}$	$27_{6,22}-26_{6,21}$	203	242.20698	0.30 ± 0.02	6.3	2.03 ± 0.34	31.7	0.04	(2)
$\text{C}_2\text{H}_5\text{CN}$	$27_{4,24}-26_{4,23}$	181	242.66469	0.32 ± 0.03	2.4	0.83 ± 0.17	33.9	0.04	...
$\text{C}_2\text{H}_5\text{CN}$	$14_{3,11}-13_{2,12}$	55	245.02365	0.32 ± 0.02	2.3	0.77 ± 0.14	35.1	0.04	...
$\text{C}_2\text{H}_5\text{CN}$	$30_{0,30}-29_{0,29}$	194	257.31064	0.11 ± 0.02	3.7	0.43 ± 0.16	34.2	0.03	...
$\text{C}_2\text{H}_5\text{CN}$	$30_{1,30}-29_{0,29}$	194	257.58361	0.20 ± 0.02	1.5	0.32 ± 0.06	33.6	0.03	...
$\text{C}_2\text{H}_5\text{CN}$	$29_{9,21}-28_{9,20}$	277	259.86276	0.11 ± 0.02	3.5	0.42 ± 0.15	33.9	0.03	(2)
$\text{C}_2\text{H}_5\text{CN}$	$29_{12,17}-28_{12,16}$	347	259.86989	0.35 ± 0.02	1.4	0.53 ± 0.08	33.4	0.03	(2)
$\text{C}_2\text{H}_5\text{CN}$	$29_{13,16}-28_{13,15}$	374	259.90664	0.09 ± 0.02	3.2	0.31 ± 0.14	33.5	0.03	(2) (3)
$\text{C}_2\text{H}_5\text{CN}$	$29_{6,24}-28_{6,23}$	227	260.22166	0.24 ± 0.02	3.1	0.80 ± 0.15	34.8	0.03	...

Table A8 continued

Table A8 (continued)

Molecule	Transition	E_u	Frequency	T_{br}	ΔV	$\int T_{br} dV$	V_{LSR}	RMS	Note
		(K)	(GHz)	(K)	(km/s)	(K km/s)	(km/s)	(K)	
C ₂ H ₅ CN	29 _{5,25} –28 _{5,24}	215	260.53569	0.27 ± 0.02	3.7	1.04 ± 0.16	34.3	0.03	...
NH ₂ CHO	13 _{0,13} –12 _{1,12}	91	244.85421	<0.08	...	<0.3	...	0.04	...
NH ₂ CHO	13 _{2,12} –13 _{1,13}	104	258.63638	0.10 ± 0.02	3.9	0.40 ± 0.17	35.6	0.03	(3)
NH ₂ CHO	12 _{2,10} –11 _{2,9}	92	260.18909	0.36 ± 0.02	4.4	1.67 ± 0.19	34.7	0.03	...
NH ₂ CHO	16 _{9,7} –15 _{9,6}	380	339.68606	0.36 ± 0.03	4.3	1.63 ± 0.36	33.2	0.07	(4)
NH ₂ CHO	16 _{8,8} –15 _{8,7}	329	339.71519	0.30 ± 0.04	3.9	1.27 ± 0.34	35.2	0.07	(4)
NH ₂ CHO	16 _{7,10} –15 _{7,9}	284	339.77954	0.36 ± 0.04	3.3	1.26 ± 0.29	33.9	0.07	(5)
NH ₂ CHO	16 _{6,11} –15 _{6,10}	246	339.90250	0.29 ± 0.04	4.9	1.49 ± 0.42	34.0	0.07	(5)
NH ₂ CHO	16 _{3,14} –15 _{3,13}	166	340.48963	0.37 ± 0.04	4.2	1.65 ± 0.36	34.0	0.07	...
NH ₂ CHO	16 _{4,13} –15 _{4,12}	186	340.53439	0.36 ± 0.04	5.2	1.98 ± 0.44	34.1	0.07	...
NH ₂ CHO	16 _{4,12} –15 _{4,11}	186	340.69074	0.46 ± 0.03	2.5	1.19 ± 0.27	33.7	0.07	...
NH ₂ CHO	16 _{2,14} –15 _{2,13}	153	349.47820	0.36 ± 0.04	3.6	1.41 ± 0.33	33.9	0.08	...
NH ₂ CHO	9 _{2,8} –8 _{1,7}	58	349.63403	<0.30	...	<1.3	...	0.08	...

NOTE—(1) Blend of four C₂H₅CN lines with similar spectroscopic constants. (2) Blend of two C₂H₅CN lines with similar spectroscopic constants. (3) Tentative detection. (4) Blend of four NH₂CHO lines with similar spectroscopic constants. (5) Blend of two NH₂CHO lines with similar spectroscopic constants.

Table A9. Line Parameters for HCOOH, H₂CCO, and c-C₂H₄O

Molecule	Transition	E_u	Frequency	T_{br}	ΔV	$\int T_{br} dV$	V_{LSR}	RMS	Note
		(K)	(GHz)	(K)	(km/s)	(K km/s)	(km/s)	(K)	
trans-HCOOH	12 _{1,12} –11 _{1,11}	84	257.97501	0.52 ± 0.02	5.5	3.00 ± 0.23	34.5	0.03	...
trans-HCOOH	15 _{4,12} –14 _{4,11}	181	338.14384	0.42 ± 0.03	5.0	2.26 ± 0.43	34.6	0.07	...
trans-HCOOH	15 _{3,13} –14 _{3,12}	158	338.20186	0.36 ± 0.03	4.4	1.70 ± 0.39	34.7	0.07	...
trans-HCOOH	15 _{4,11} –14 _{4,10}	181	338.24882	0.35 ± 0.04	2.8	1.04 ± 0.26	34.7	0.07	...
trans-HCOOH	15 _{3,12} –14 _{3,11}	159	340.22910	0.31 ± 0.04	5.8	1.92 ± 0.49	35.1	0.07	...
cis-HCOOH	13 _{0,13} –12 _{1,12}	95	244.23510	0.33 ± 0.02	1.6	0.57 ± 0.09	35.7	0.04	...
cis-HCOOH	9 _{1,9} –8 _{0,8}	49	244.24786	0.27 ± 0.02	2.5	0.73 ± 0.16	34.2	0.04	(1)
H ₂ CCO	12 _{4,9} –11 _{4,8}	284	242.30938	0.12 ± 0.02	3.0	0.36 ± 0.16	34.3	0.04	(2)
H ₂ CCO	12 _{0,12} –11 _{0,11}	76	242.37573	0.23 ± 0.02	4.0	0.99 ± 0.27	33.8	0.04	...
H ₂ CCO	12 _{3,10} –11 _{3,9}	193	242.39845	0.41 ± 0.03	3.1	1.35 ± 0.19	34.4	0.04	(2)
H ₂ CCO	12 _{2,11} –11 _{2,10}	128	242.42466	<0.10	...	<0.4	...	0.04	...
H ₂ CCO	12 _{2,10} –11 _{2,9}	128	242.53616	0.13 ± 0.02	3.2	0.43 ± 0.19	35.5	0.04	...
H ₂ CCO	12 _{1,11} –11 _{1,10}	89	244.71227	0.61 ± 0.03	3.4	2.24 ± 0.20	34.4	0.04	...
H ₂ CCO	13 _{1,13} –12 _{1,12}	100	260.19198	0.67 ± 0.02	3.1	2.21 ± 0.18	34.6	0.03	...
H ₂ CCO	17 _{1,17} –16 _{1,16}	160	340.19308	0.41 ± 0.03	4.8	2.08 ± 0.61	34.6	0.07	(3)
c-C ₂ H ₄ O	11 _{2,10} –10 _{1,9}	104	338.77198	0.35 ± 0.03	4.2	1.57 ± 0.35	34.6	0.07	(4)

NOTE—(1) Partial blend with SO₂. (2) Blend of two H₂CCO lines with similar spectroscopic constants. (3) Partial blend with C₂H₅OH. (4) Blend of two c-C₂H₄O lines with similar spectroscopic constants.

B. FITTED SPECTRA

Figures B1–B11 show the results of the spectral line fitting (see Section 3.1 for details).

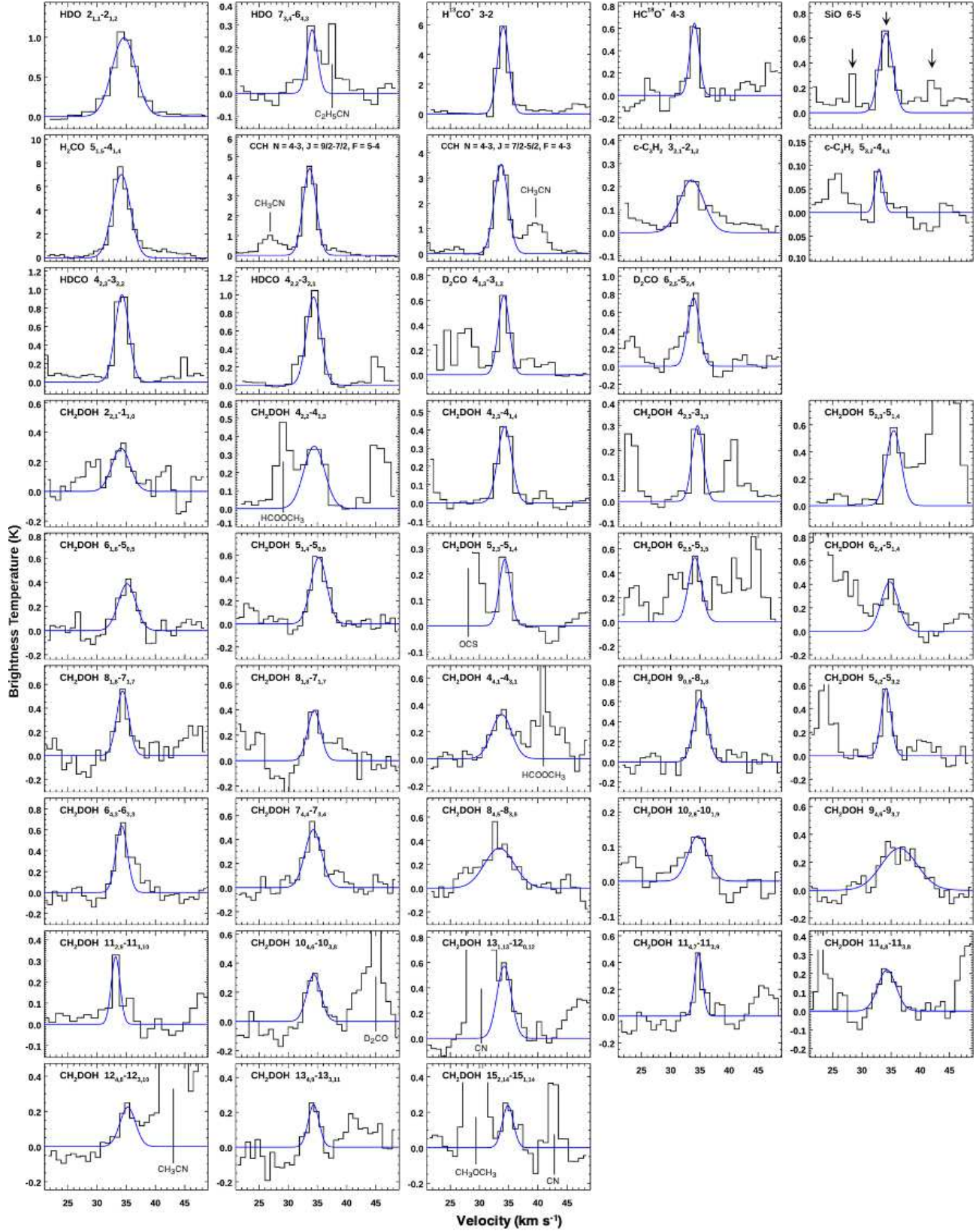


Figure B1. ALMA spectra of the detected molecular emission lines. The blue lines represent fitted Gaussian profiles. For the molecules with multiple line detection, the spectra are sorted in ascending order of the upper state energy (the emission line with the lowest upper state energy is shown in the upper left panel and that with the highest energy is in the lower right panel). For SiO, the positions of primary and secondary peaks are indicated by arrows.

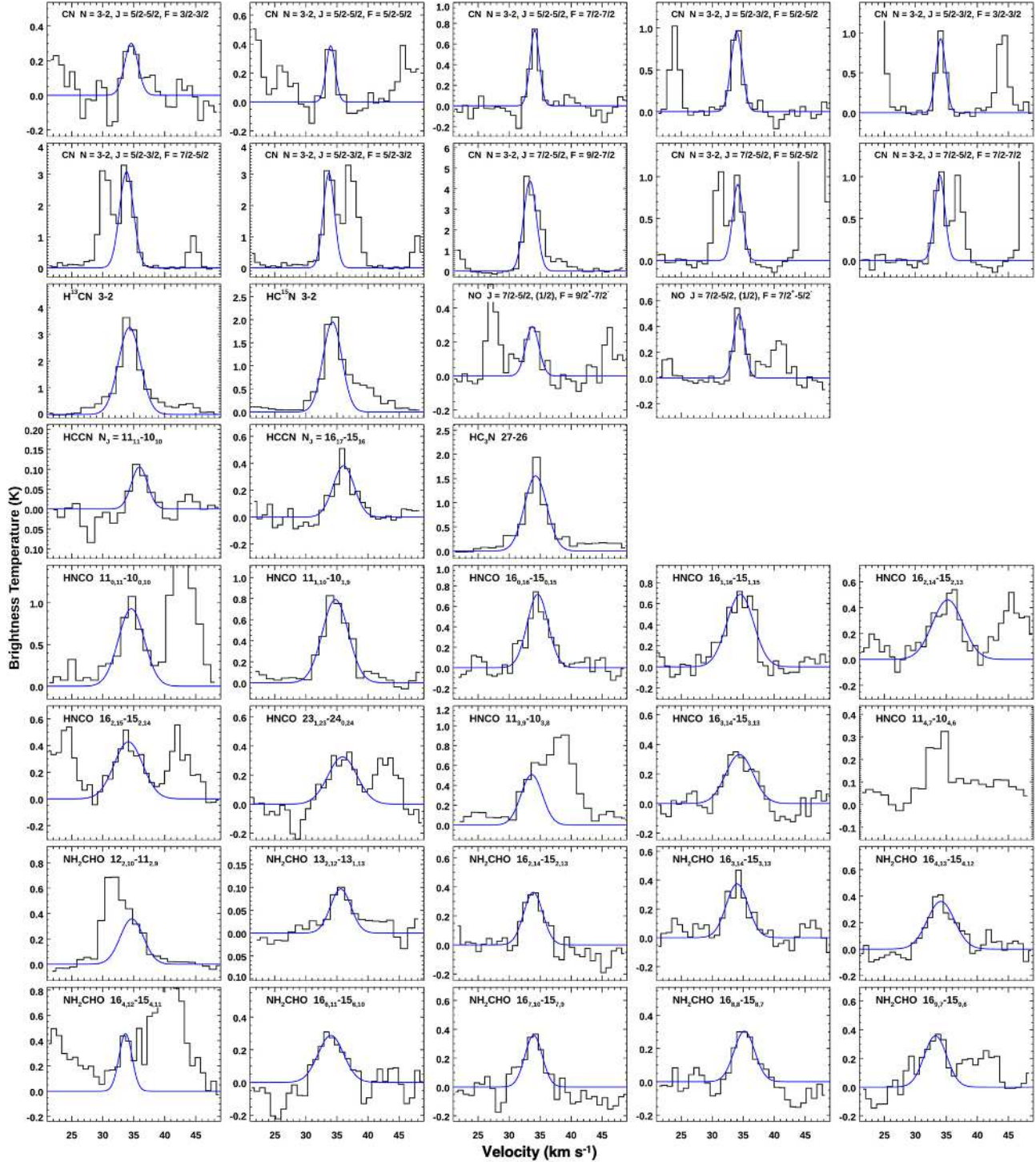


Figure B2. Same as in Figure B1 but for nitrogen-bearing molecules.

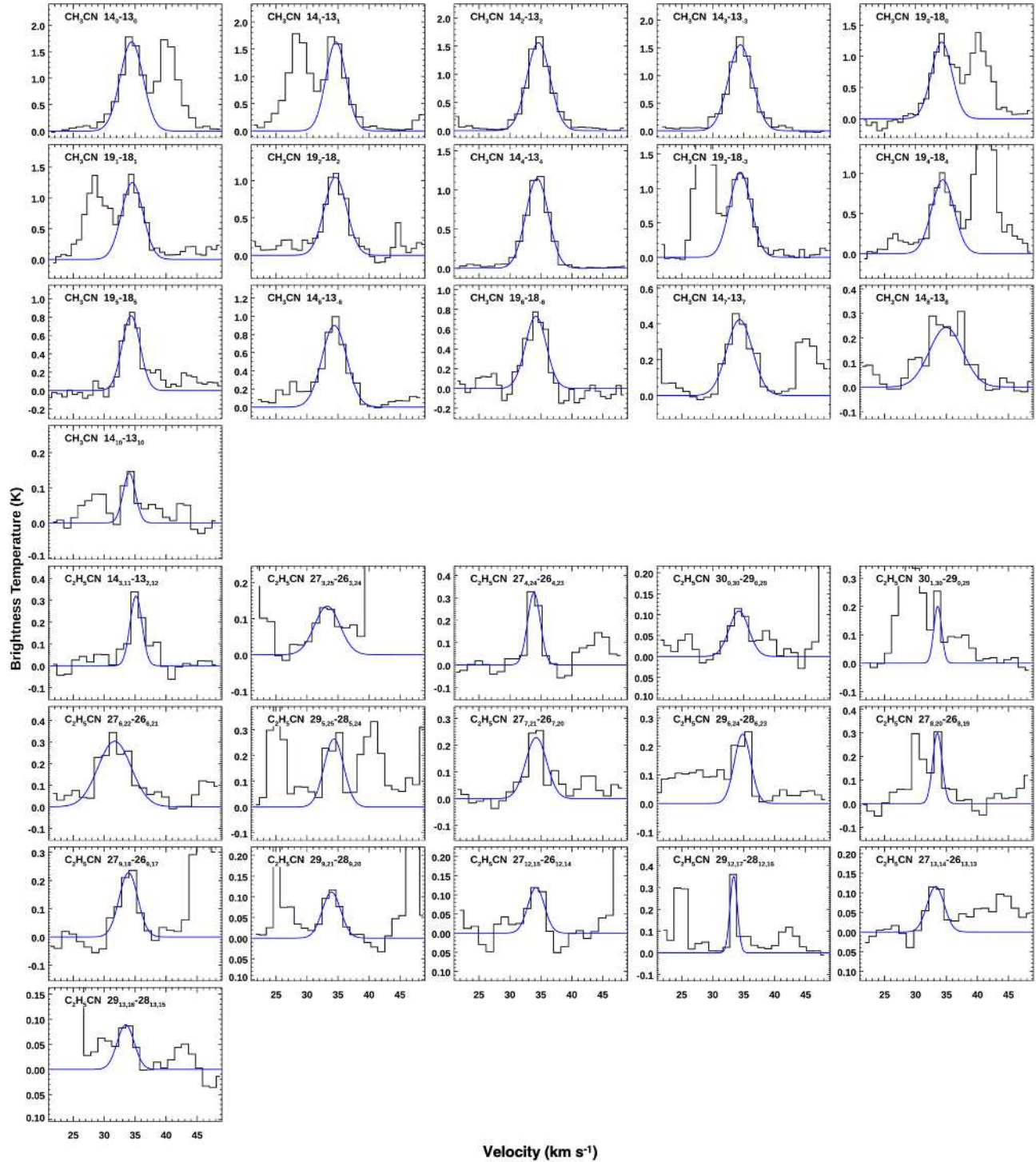


Figure B3. Same as in Figure B1 but for nitrogen-bearing molecules (continued).

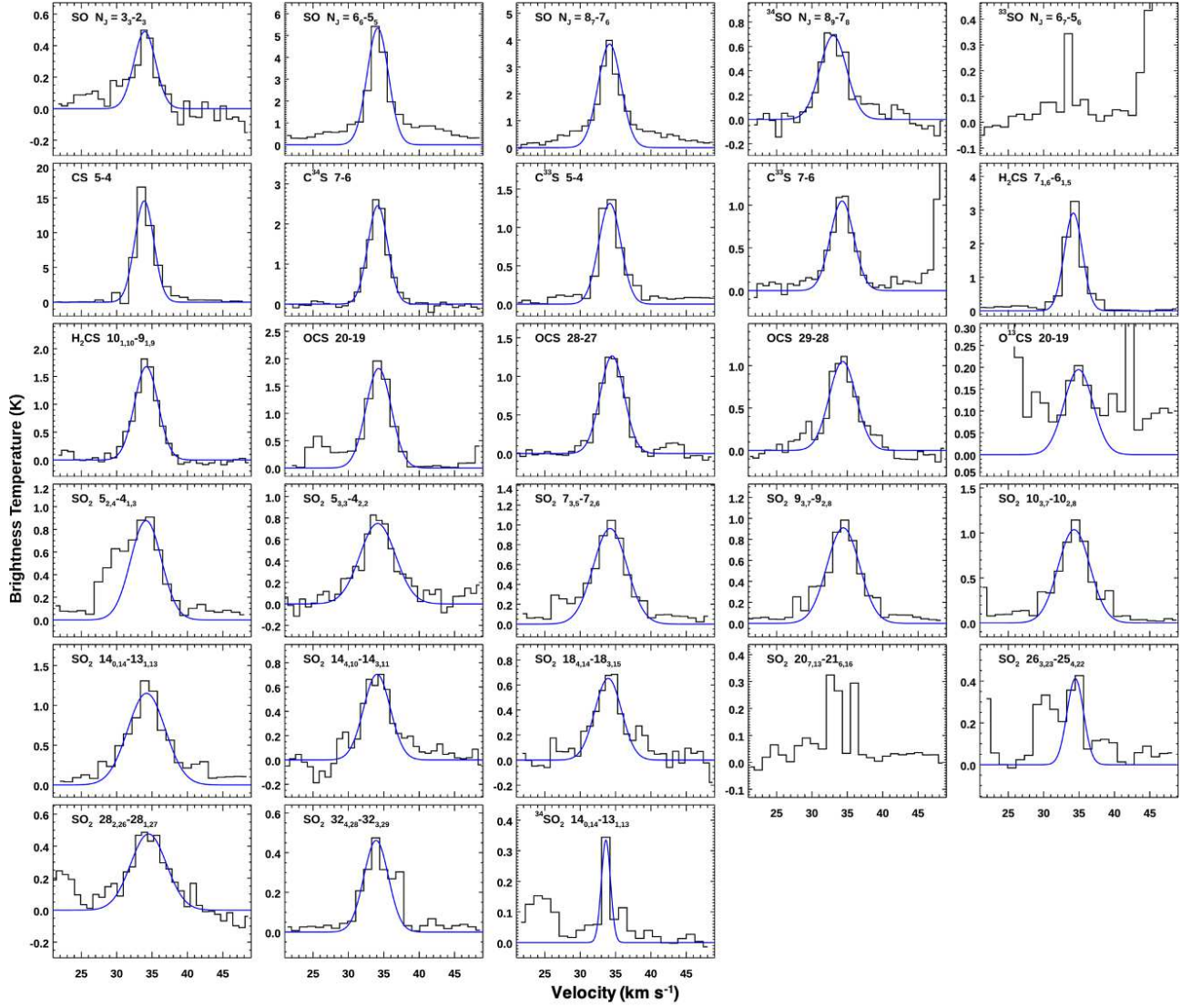


Figure B4. Same as in Figure B1 but for sulfur-bearing molecules.

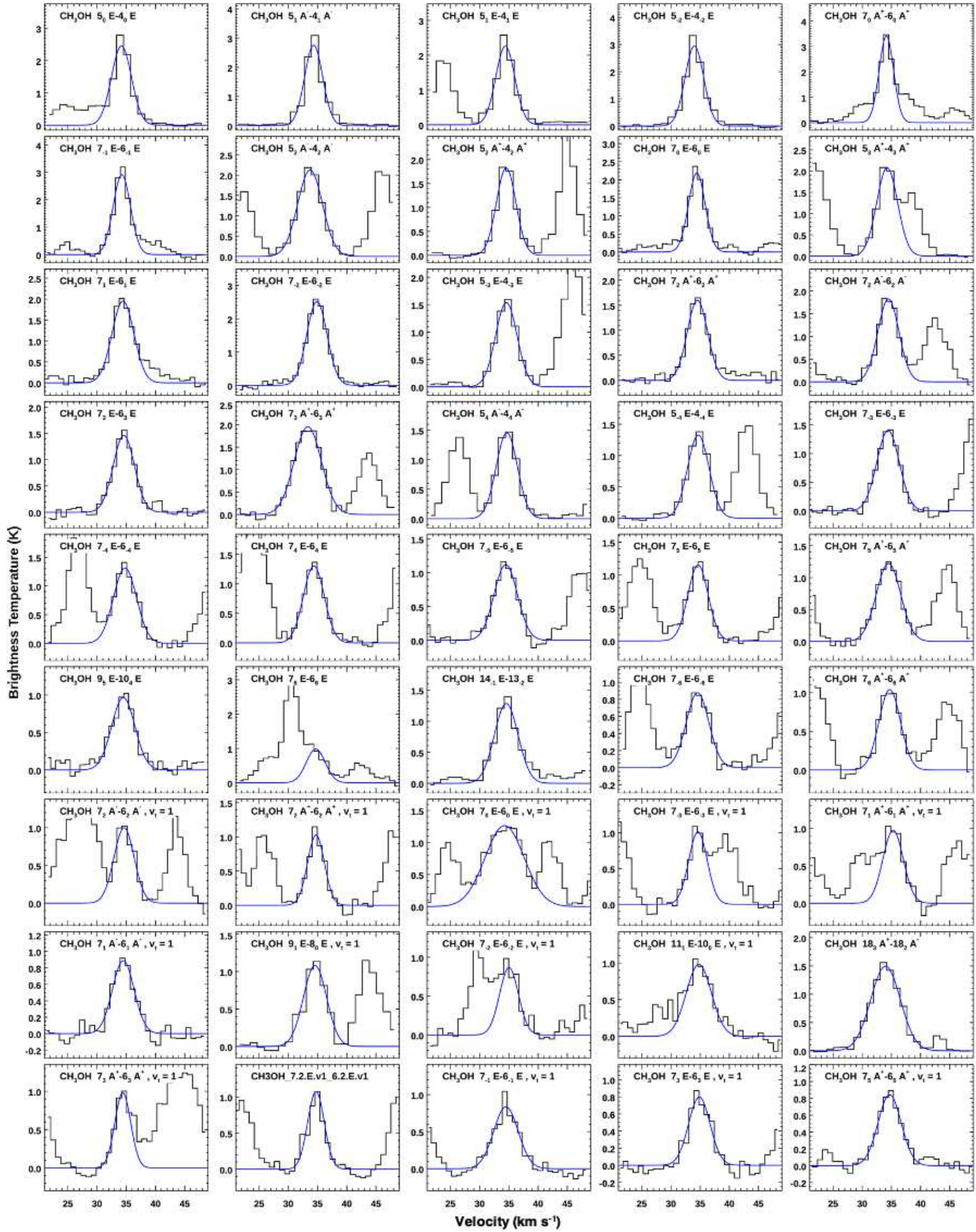


Figure B5. Same as in Figure B1 but for CH_3OH .

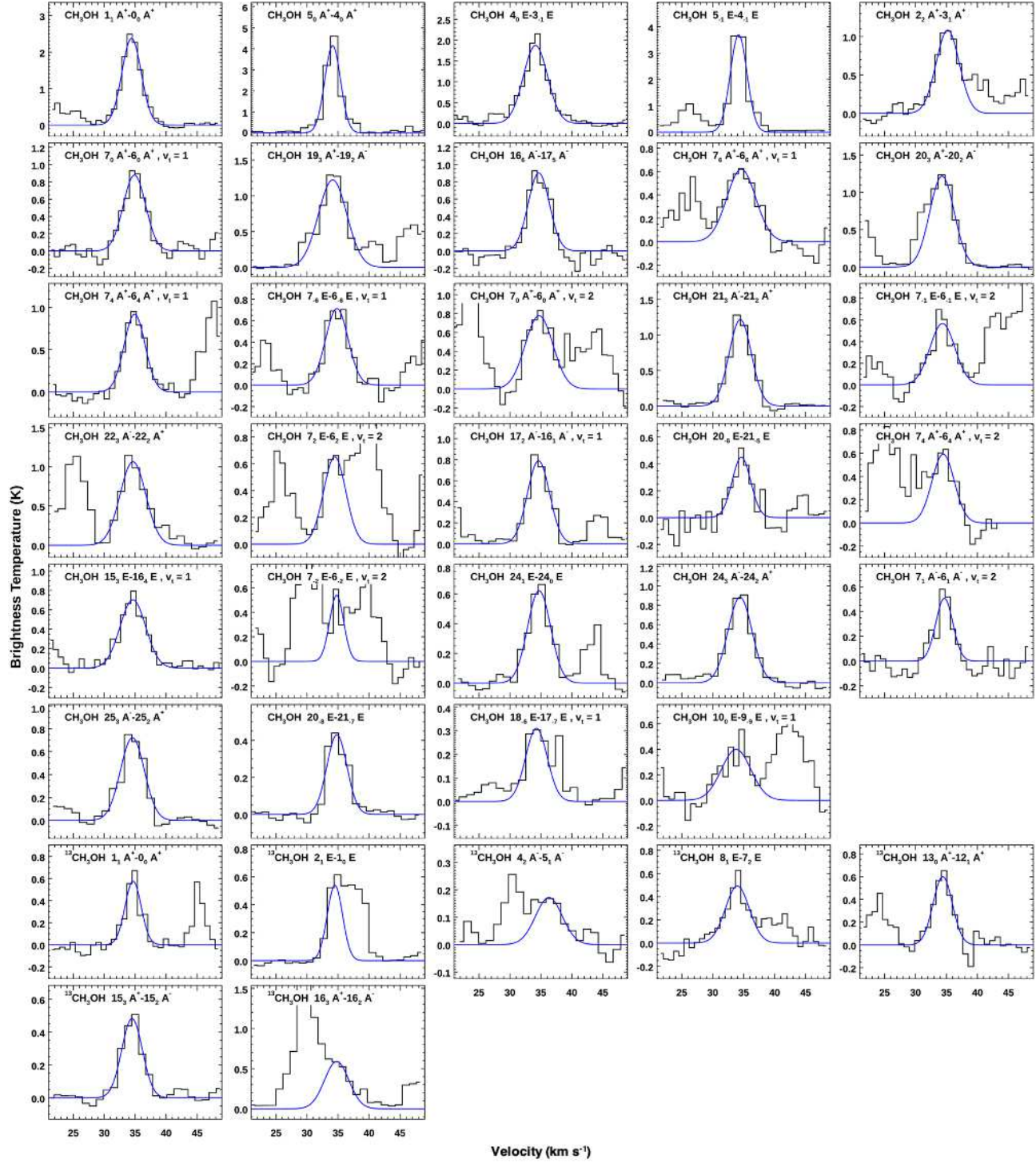


Figure B6. Same as in Figure B1 but for CH₃OH (continued) and ¹³CH₃OH.

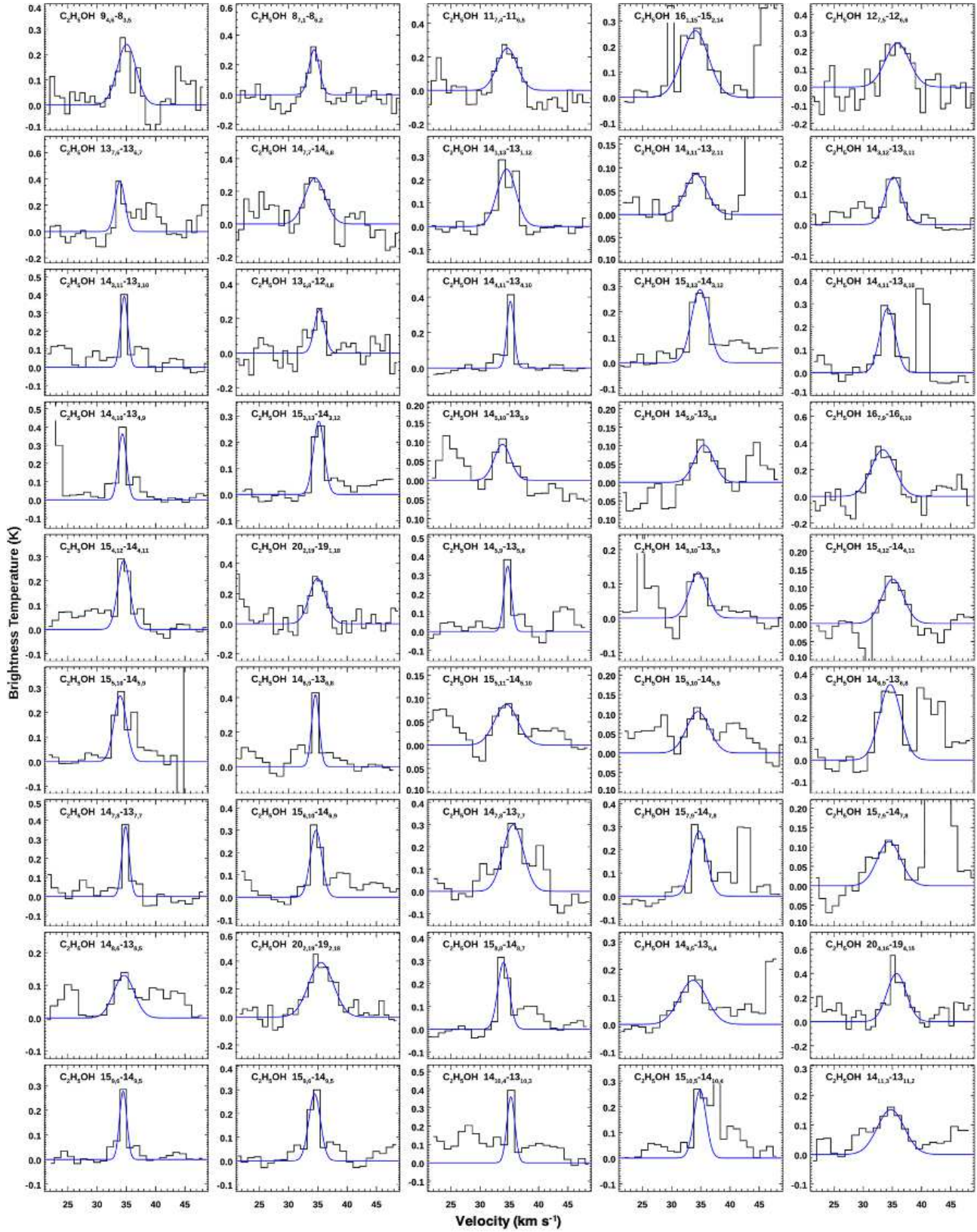


Figure B7. Same as in Figure B1 but for C₂H₅OH.

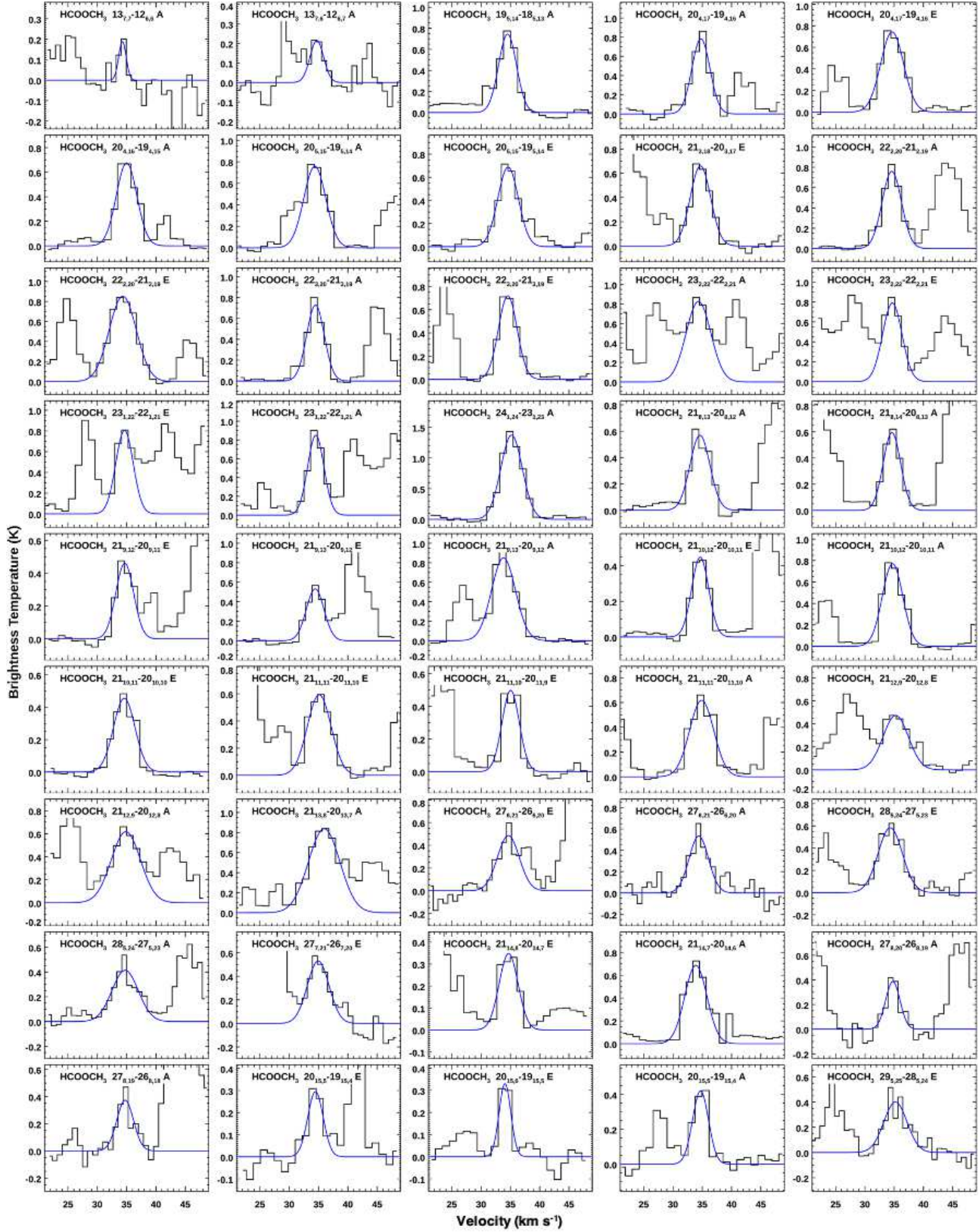


Figure B8. Same as in Figure B1 but for HCOOCH₃.

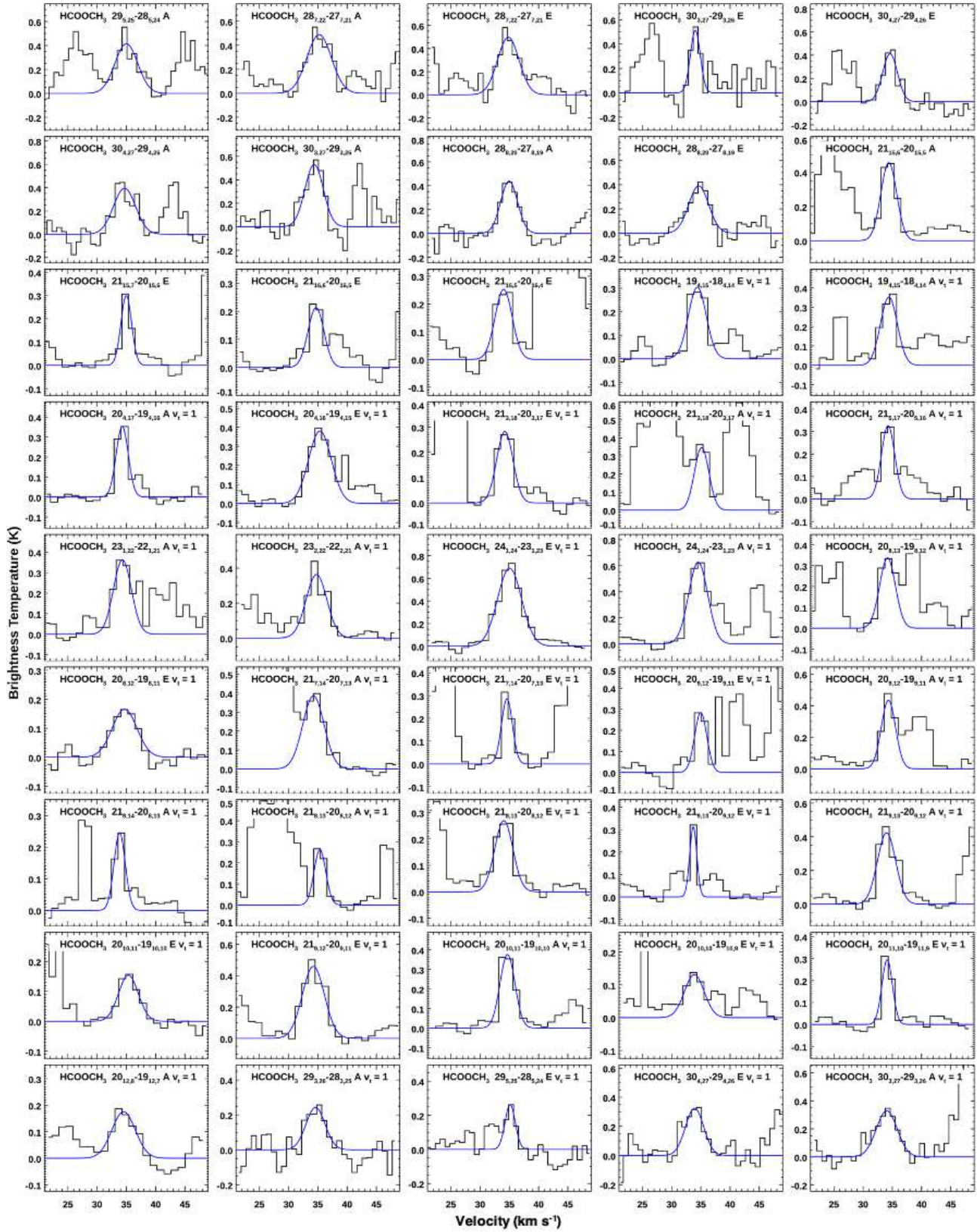


Figure B9. Same as in Figure B1 but for HCOOCH_3 (continued).

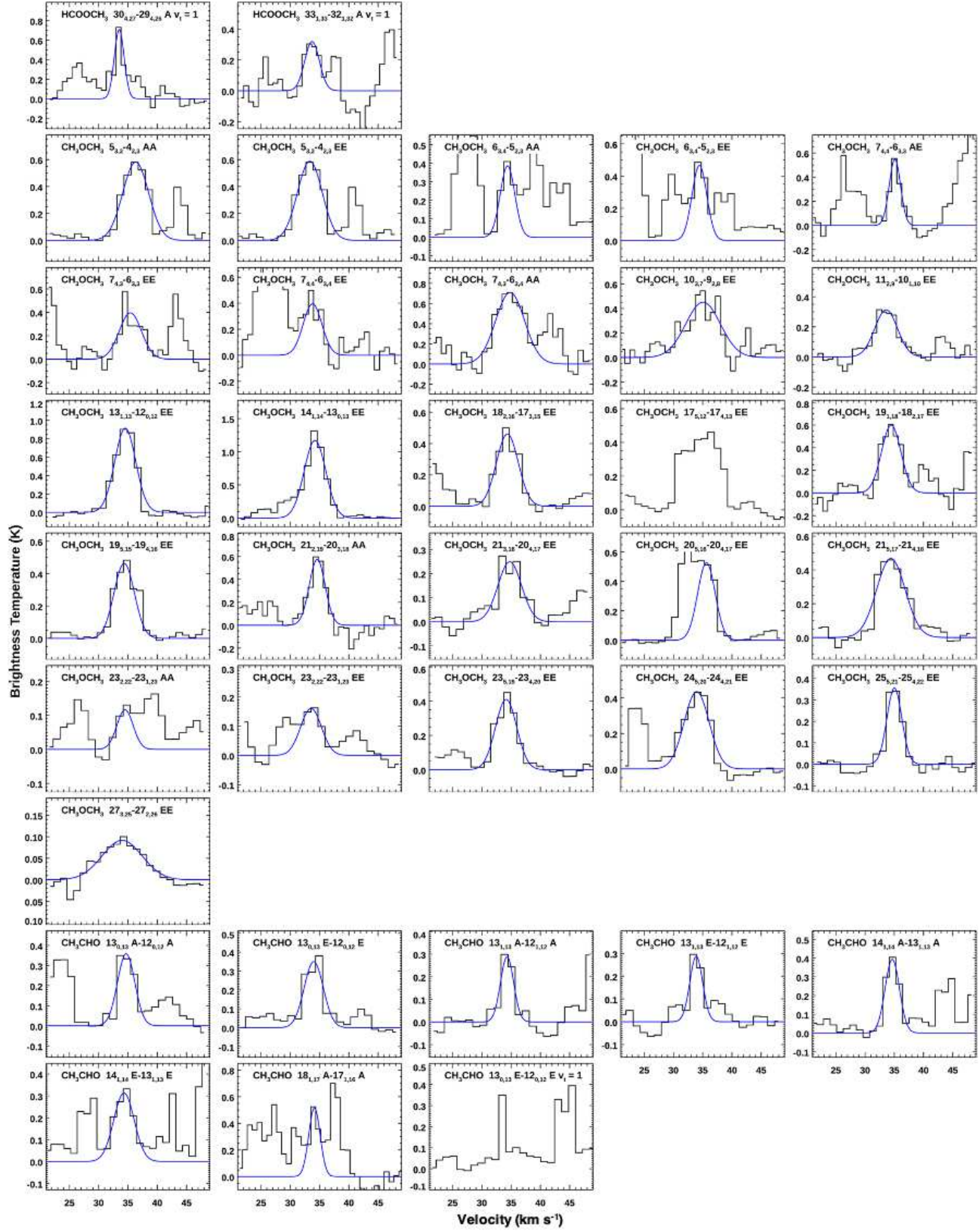


Figure B10. Same as in Figure B1 but for HCOOCH₃ (continued), CH₃OCH₃, and CH₃CHO.

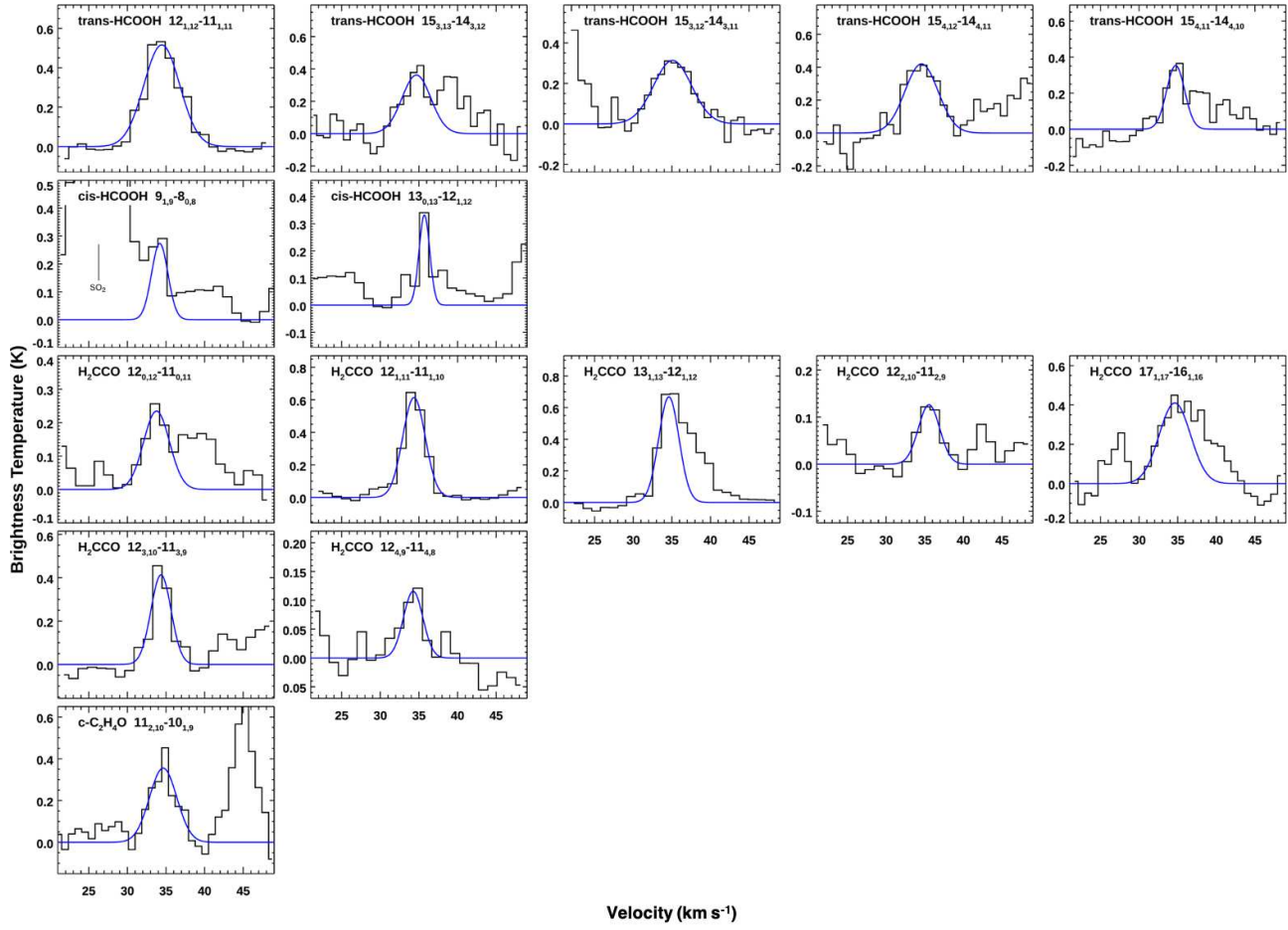


Figure B11. Same as in Figure B1 but for HCOOH, H₂CCO, and c-C₂H₄O.